

INFORMATION TO USERS

This manuscript has been reproduced from the microfilm master. UMI films the text directly from the original or copy submitted. Thus, some thesis and dissertation copies are in typewriter face, while others may be from any type of computer printer.

The quality of this reproduction is dependent upon the quality of the copy submitted. Broken or indistinct print, colored or poor quality illustrations and photographs, print bleedthrough, substandard margins, and improper alignment can adversely affect reproduction.

In the unlikely event that the author did not send UMI a complete manuscript and there are missing pages, these will be noted. Also, if unauthorized copyright material had to be removed, a note will indicate the deletion.

Oversize materials (e.g., maps, drawings, charts) are reproduced by sectioning the original, beginning at the upper left-hand corner and continuing from left to right in equal sections with small overlaps.

ProQuest Information and Learning
300 North Zeeb Road, Ann Arbor, MI 48106-1346 USA
800-521-0600

UMI[®]

University of Alberta

Melting Phenomena in Polymer Blending

by

Hongbing Chen



A thesis submitted to the Faculty of Graduate Studies and Research in partial fulfillment of the requirements for the degree of
Doctor of Philosophy

in

Chemical Engineering

Department of Chemical & Materials Engineering

Edmonton, Alberta

Fall 2005



Library and
Archives Canada

Bibliothèque et
Archives Canada

Published Heritage
Branch

Direction du
Patrimoine de l'édition

0-494-08621-1

395 Wellington Street
Ottawa ON K1A 0N4
Canada

395, rue Wellington
Ottawa ON K1A 0N4
Canada

Your file *Votre référence*

ISBN:

Our file *Notre référence*

ISBN:

NOTICE:

The author has granted a non-exclusive license allowing Library and Archives Canada to reproduce, publish, archive, preserve, conserve, communicate to the public by telecommunication or on the Internet, loan, distribute and sell theses worldwide, for commercial or non-commercial purposes, in microform, paper, electronic and/or any other formats.

The author retains copyright ownership and moral rights in this thesis. Neither the thesis nor substantial extracts from it may be printed or otherwise reproduced without the author's permission.

AVIS:

L'auteur a accordé une licence non exclusive permettant à la Bibliothèque et Archives Canada de reproduire, publier, archiver, sauvegarder, conserver, transmettre au public par télécommunication ou par l'Internet, prêter, distribuer et vendre des thèses partout dans le monde, à des fins commerciales ou autres, sur support microforme, papier, électronique et/ou autres formats.

L'auteur conserve la propriété du droit d'auteur et des droits moraux qui protègent cette thèse. Ni la thèse ni des extraits substantiels de celle-ci ne doivent être imprimés ou autrement reproduits sans son autorisation.

In compliance with the Canadian Privacy Act some supporting forms may have been removed from this thesis.

Conformément à la loi canadienne sur la protection de la vie privée, quelques formulaires secondaires ont été enlevés de cette thèse.

While these forms may be included in the document page count, their removal does not represent any loss of content from the thesis.

Bien que ces formulaires aient inclus dans la pagination, il n'y aura aucun contenu manquant.


Canada

Abstract

This study is focused on understanding of the melting process of polymer blends during blending. Four topics are addressed in this thesis: melting behavior of polymer blends in an extruder; heat transfer between a solid polymer pellet and polymer melt; rheological properties of polymer melt suspensions; and morphology development of polymer blends during melting.

A barrel sliding mechanism and a perturbation method was used to investigate the melting behavior of polypropylene (PP) and polystyrene (PS) blends in the extruder. It was found that the melting process in the extruder could be divided into three distinct regions. Most of melting occurred in the transition region mainly due to mechanical energy input. Friction between solid polymer pellets played a critical role in converting mechanical energy into heat. The location of the transition region for each process could be determined from the on-line visualization results, temperature and pressure profiles, and the perturbation signals.

A representative heat transfer coefficient between a solid polymer pellet and another polymer melt under shear flow was obtained as $250 W / m^2 \cdot K$ through numerical simulations. The dynamics of thermocouple used in the experiment was captured using a first order process approximation. A good match was achieved between the simulation and experiment after taking the thermocouple dynamics into account.

Suspensions of ethylene acrylate copolymer (EAC) melt with PS beads were used to study rheological properties of polymer flow during extrusion. It was found that deformation of PS beads under high local shear stress could result in the decrease of the relative viscosity with increasing volume fraction.

On-line visualization in a TSE showed an “erosion” mechanism for polycarbonate (PC) drop deformation and breakup in polyethylene (PE) melt. This “erosion” mechanism was also found from corresponding numerical simulations. Stress peaks at the interface from simulation result could explain the “erosion” mechanism.

Acknowledgement

This thesis is the result of four and half years work whereby I have been accompanied and supported by many people. It is a pleasant moment for me that I have now the opportunity to express my gratitude for all of them.

The first persons I would like to thank are my two supervisors Prof. Uttandaraman Sundararaj and Prof. Krishnaswamy Nandakumar, whose guidance, stimulating suggestions and inspiration helped me during all the time of research and writing of this thesis. Their dedication to their jobs and enthusiasm of exploring new fields present me a model to follow in my career. Our once a week regular meeting fed me continuously with new ideas or suggestions on my research in the last four years. They could not even realize how much I have learned from them. I am really glad that I have come to know both of them in my life.

I would like to express my deep gratitude to Dr. Mark Wetzels in DuPont Experimental Station for providing me the opportunity to carry out most experiments in Chapter 2 and Chapter 4. The experience to work with him in an industrial environment goes far beyond what I can obtain in school. I also want to thank Dr. Michael Pottiger in DuPont for his support on rheological testing in chapter 4. It was an enjoyable cooperation with both of them. I also received lots of help from many other people when I was in DuPont, Mr. Donald Denelsbeck, Mr. John Howe, Ms. Susan Latimer, Ms. Anna Berl, and Mr. Jonathan Doran, many thanks for your great help.

My appreciations go to Prof. Suzanne Kresta and Prof. Alan Mather in University of Alberta for their valuable comments and suggestions on my research. I also want to thank my colleagues in the polymer processing group who gave me the feeling of being at home at work. Particularly, I would like to thank Dr. Bin Lin for

providing me some erosion pictures in chapter 5. My thanks also go to Mr. Bob Barton, Mr. Walter Boddez, Mr. Richard Cooper, and Mr. Les Dean in the Department of Chemical and Materials Engineering, University of Alberta for their excellent technical support during my research.

I am very thankful for the financial support from DuPont for my research, and the Lew Erwin Memorial Scholarship from the extrusion division, Society of Plastics Engineers is also highly acknowledged.

My special thanks go to my girl friend Weijie, for her support, and many valuable suggestions on my research. One of the best experiences is that I was “forced” to work on my projects many times in weekends because she needed to run her experiments. As a result of it, many important results in this thesis were found in a mood that I was forced to work.

I feel a deep sense of gratitude for my parents, and my only brother who taught me the good things that really matter in life. Thanks for their unfailing love and support that I did not get lost in my life. This thesis would be impossible without their encouragement and help in the first instance.

Table of Contents

Chapter 1	Introduction	1
1.1	A brief history of polymer blends	1
1.2	Property - morphology - processing of polymer blends	2
1.3	Polymer melting in extrusion	5
1.4	Objectives of the thesis	8
1.5	Structure of the thesis	8
1.6	References	11
Chapter 2	Melting of PS/PP blends in a twin screw extruder	20
2.1	Introduction	20
2.1.1	PREVIOUS WORK	21
2.1.2	SLIDING BARREL MECHANISM	24
2.1.3	PERTURBATION METHOD	25
2.2	PS/PP (80:20) and PP/PS (80:20) blends at constant Q/N	27
2.2.1	EXTRUSION SETUP	27
2.2.2	MATERIALS	31
2.2.3	RESULTS AND DISCUSSION	33
2.2.3.1	PP/PS (80:20) Blend	33
2.2.3.2	PS/PP (80:20) Blend	40
2.2.3.3	Comparison of PP/PS (80:20) and PS/PP (80:20) extrusions	43
2.3	PS/PP (80:20) blend at various Q/N	47
2.3.1	EXPERIMENTAL	47
2.3.2	RESULTS AND DISCUSSION	50
2.3.2.1	On-line Pressure, Temperature and Visualization Measurements	50
2.3.2.1.1	Partially Filled Region	54
2.3.2.1.2	Transition Region	57
2.3.2.1.3	Fully Filled Region	60
2.3.2.2	RTD and Pulse Measurements	60
2.3.2.3	Determination of Transition Region Location	65
2.4	Summary	67
2.5	References	69
Chapter 3	Heat transfer in polymer melts	73
3.1	Introduction	73
3.2	Experimental procedures	76
3.2.1	POLYMER PROPERTIES	76
3.2.2	BATCH MIXER EXPERIMENT	79
3.3	Model equations	83
3.4	Results and discussion	89

3.4.1	EXPERIMENTAL RESULTS	89
3.4.2	SIMULATION RESULTS	97
3.5	Summary	103
3.6	References	104
Chapter 4	Rheology of polymer melt suspensions	107
4.1	Introduction	107
4.2	Previous work	109
4.3	Experimental	114
4.3.1	MATERIALS AND SAMPLE PREPARATION	114
4.3.2	RHEOLOGICAL MEASUREMENT	116
4.4	Results and discussion	117
4.4.1	VISCOSITY OF SUSPENSIONS	117
4.4.2	COMPLEX SHEAR MODULUS OF SUSPENSIONS	128
4.4.3	STRUCTURE EFFECT ON VISCOSITY	130
4.4	Summary	134
4.5	References	135
Chapter 5	Polymer drop deformation and breakup in polymer blends	140
5.1	Introduction	140
5.2	On-line visualization of PE/PC blending	143
5.3	Numerical Modeling	146
5.3.1	MODEL GEOMETRIES	146
5.3.2	MODEL EQUATIONS	147
5.3.3	VOF METHOD	148
5.3.4	MATERIAL PROPERTIES	149
5.4	Results and discussion	152
5.4.1	ON-LINE VISUALIZATION OF PE/PC BLENDING	152
5.4.2	MODELING OF PE/PE Blend	153
5.4.3	MODELING OF PE/PC Blend	157
5.5	Summary	163
5.6	References	164
Chapter 6	General discussion and future work	167
6.1	General discussion and conclusions	167
6.2	Future work	176
6.2.1	Melting or reacting of polymer blends during extrusion	176
6.2.2	Heat transfer of a free moving solid polymer pellet in polymer pellet	177
6.2.3	Rheology of polymer blends in transition from suspension to emulsion	178
6.2.4	Heat balance of polymer flow during melting	179

6.2.5	Modeling of drop deformation and breakup with viscoelastic properties	180
6.3	References	182

List of Tables

Table 2.1	Operating conditions for PP/PS (80:20) and PS/PP (80:20) blends at constant Q/N.	30
Table 2.2	Properties of PP and PS.	31
Table 2.3	Operation parameters for extrusion of PS/PP (80:20) blend with various Q/N.	48
Table 2.4	Determination of locations of the transition region for various Q/N*.	65
Table 3.1	Parameters of PEI pellet used in calculating the mean h -value from experimental data.	80
Table 3.2	Property values of PE and PEI used in the simulations.	84
Table 3.3	Summary of heat transfer coefficients from experiment and simulations.	95
Table 4.1	Data fitting using power law model, $\eta = \eta_0 \cdot \dot{\gamma}^{(n-1)}$, for sandwich EAC/PS suspensions.	119
Table 5.1	Properties of PE and PC used in modeling.	151

List of Figures

Figure 2.1	Sliding barrel mechanism for visualization.	24
Figure 2.2	Glass window for visualization and light sources above the window.	27
Figure 2.3	Probe locations in the spacer plate for PS/PP blends at constant Q/N.	28
Figure 2.4	Screw configuration for the melting zone.	28
Figure 2.5	Extruder configuration and experimental setup. Note W and X axes.	29
Figure 2.6	Original shape of PS and PP pellets.	32
Figure 2.7	Viscosity of PS and PP at 220°C.	33
Figure 2.8	Visualization of PP/PS (80:20) blending process in the TSE. Each image begins at the value of X given and is 30mm in width. That is, for each image, there is a 10mm overlap on either side with the adjacent images.	34
Figure 2.9	Axial temperature and pressure profiles for the extrusion of PP/PS (80:20) blend.	34
Figure 2.10	Visualization of PS/PP (80:20) blending process in the TSE. Each image begins at the value of X given and is 30mm in width. That is, for each image, there is a 10mm overlap on either side with the adjacent images.	41
Figure 2.11	Axial temperature and pressure profiles for the extrusion of PS/PP (80:20) blend.	41
Figure 2.12	Melting sequences of PP/PS (80:20) blend and PS/PP (80:20) blend in the TSE.	44
Figure 2.13	Melt area fraction along the extrusion channel for constant Q/N.	44
Figure 2.14	Melt mechanism of polymer pellets in a TSE. The majority of melting occurs in section b) and c). In each section, different heat sources dominate the melting: a) heat conduction and FED;	

	b) FED & PED; c) PED & VED; d) VED & heat convection; e) melting finished.	45
Figure 2.15	Probe locations in the spacer plate for extrusions with various Q/N.	47
Figure 2.16	Heat capacities of PS and PP.	49
Figure 2.17	Visualization of PS/PP blend at different Q/N: a) Q/N=5.0g/rev; b) Q/N=7.6g/rev; c) Q/N=11.3g/rev.	50
Figure 2.18	Axial pressure profiles for the three runs with various Q/N.	51
Figure 2.19	Axial temperature profiles for the three runs with various Q/N.	52
Figure 2.20	High speed video images for Q/N=7.6g/rev at locations: a) X=150mm; b) X=170mm; c) X=190mm; d) X=210mm.	52
Figure 2.21	Melt area fraction along the extrusion channel for the three runs with various Q/N.	53
Figure 2.22	Relative positions of the melting peak and the RTD peak: a) Q/N=5.0g/rev; b) Q/N=7.6g/rev; c) Q/N=11.3g/rev. It can be seen that motor power peak and RTD peak coincide at a) X=240mm, b) X=190mm, c) X=180mm. These locations correspond approximately to the midpoint of the transition region in Figure 2.16. The transition region is where most of the melting was observed.	61
Figure 3.1	Variation of thermal conductivity with temperature for PEI (data supplied by GE Plastics).	76
Figure 3.2	Specific heat of PEI with temperature.	77
Figure 3.3	Specific heat of PE with temperature.	77
Figure 3.4	Viscosity of PE at three different temperatures.	78
Figure 3.5	Schematic of the batch mixer experimental setup.	79
Figure 3.6	Flow diagram for calculating the mean heat transfer coefficient, \bar{h} , from the experimental temperature history.	81
Figure 3.7	Geometric model and boundary conditions: a) two-dimensional approximation with axis perpendicular to flow; b) two-	

	dimensional approximation with axis parallel to flow: c) three-dimensional geometry of the batch mixer. (Figures not to scale).	85
Figure 3.8	Finite element grid distribution for the three geometries considered in this work: a) 2D simulation with axis perpendicular to the flow; b) 2D simulation with axis parallel to the flow; c) 3D simulation.	87
Figure 3.9	Comparison of the experimentally measured center point temperature with those predicted from the simulations. Thermocouple dynamics were not accounted for.	89
Figure 3.10	First order process approximation of the thermocouple dynamics (time constant=0.9s): a) model used to shift the 3D simulation curve to include thermocouple delay, b) model used to shift the experimental curve to remove thermocouple delay.	90
Figure 3.11	Results of shifting 3D simulation and experiment data using a first order process approximation with time constant 0.9s: a) simulation curve shifted to include thermocouple delay, and b) experimental curve shifted to remove thermocouple delay.	91
Figure 3.12	Comparison of the center point temperature curves from the experiment and that predicted with $h=370 \text{ W/m}^2/\text{K}$ using algorithm outlined in Figure 3.6.	93
Figure 3.13	Variation of spatially averaged h -values with time: a) 2D simulation with axis perpendicular to the flow ($h=1160 \text{ W/m}^2/\text{K}$); b) 2D simulation with axis parallel to the flow ($h=420 \text{ W/m}^2/\text{K}$); c) 3D simulation ($h=250 \text{ W/m}^2/\text{K}$).	94
Figure 3.14	Temperature profile and vector plots of the velocity field for the three cases are shown at the end of 1 s: a) 2D simulation with axis perpendicular to the flow; b) 2D simulation with axis parallel to the flow; c) 3D simulation.	98
Figure 3.15	a) Y component velocity variation and b) Temperature variation from the three-dimensional simulation along x , ($y=0, z=-3$). The sampling line cuts across the pellet as shown in the inset. Axes are defined in Figure 3.8c.	99
Figure 3.16	Shear rate plots along a line through the pellet from the three dimensional simulation at different times. The location is along x , ($y=0, z=-3$). Axes are defined in Figure 3.8c.	101
Figure 3.17	Viscosity plots along a line through the pellet from the three	

	dimensional simulation at different times. The location is along x , ($y=0, z=-3$). Axes are defined in Figure 3.8c.	102
Figure 4.1	Relationship between specific volume and temperature for EAC and PS.	114
Figure 4.2	Size distribution of PS beads.	115
Figure 4.3	Complex viscosity versus frequency for the sandwich EAC/PS suspensions: a) 70°C; b) 80°C; c) 90°C.	118
Figure 4.4	Complex viscosity versus volume fraction for the sandwich EAC/PS suspensions: a) 70°C; b) 80°C; c) 90°C.	120
Figure 4.5	Complex viscosity versus volume fraction for the sandwich EAC/GB suspensions at 80 °C.	121
Figure 4.6	The relative viscosity versus volume fraction for the sandwich EAC/PS suspensions: a) 70°C; b) 80°C; c) 90°C.	122
Figure 4.7	The relative viscosity versus volume fraction for the sandwich EAC/GB suspension at 80°C.	123
Figure 4.8	The relative viscosity versus volume fraction at constant frequency for the sandwich EAC/PS suspensions: a) 10s ⁻¹ ; b) 100s ⁻¹ .	126
Figure 4.9	Deformation of PS beads under local shear stress.	126
Figure 4.10	Experimental data fitting using well known equations.	127
Figure 4.11	The relative elastic modulus and viscous modulus versus volume fraction at 80°C and frequency 50s ⁻¹ for the sandwich EAC/PS suspensions.	130
Figure 4.12	The relative viscosity versus volume fraction for EAC/PS suspensions at 80°C: a) sandwich, b) homogeneous.	131
Figure 4.13	The relative viscosity versus volume fraction for the sandwich and homogeneous EAC/PS suspensions at 80°C and frequency 50s ⁻¹ .	132
Figure 4.14	PS beads distribution in EAC/PS suspensions at $\phi = 47\%$: a) sandwich; b)homogeneous.	132

Figure 5.1	Original shapes of PE and PC pellets: a) PC; b) PE.	143
Figure 5.2	Dynamic viscosity versus frequency at different temperatures: a) PE and b) PC.	144
Figure 5.3	Simulation models, boundary and initial conditions: a) PE/PE blend; b) PE/PC blend.	146
Figure 5.4	Velocity U_x and nominal shear rate versus time for PC/PE blend.	147
Figure 5.5	Dynamic viscosity of PE versus temperature. This relation was used in simulation of the PE/PE blend.	150
Figure 5.6	On-line visualization of PE/PC blending in TSE (“erosion” of some PC pellets in pictures at $X=250$ and $X=270$ is highlighted, refer to Figure 2.5 for the definition of X , in the unit of mm).	153
Figure 5.7	Deformation and breakup mechanism of PE drop in PE melt under shear flow at different times and corresponding temperature contours.	154
Figure 5.8	PC drop deformation and erosion in PE matrix at nominal shear rate $\dot{\gamma} = 17s^{-1}$ and viscosity ratio of 9: a) $t=0s$ (no deformation); b) $t=1632s$; c) $t=1747s$; d) $t=2356s$ (Lin et al., 2003).	156
Figure 5.9	Deformation and breakup mechanism of PC drop in PE melt under shear flow for $t < 8s$ and corresponding temperature contours.	158
Figure 5.10	Deformation and breakup mechanism of PC drop in PE melt under shear flow for $t=21.7\sim 22.9s$.	159
Figure 5.11	a) Cross section AB chosen for plots at time 21.7s; b) Volume concentration vs. position at time 21.7s; c) Temperature vs. position at time 21.7s; d) Shear rate vs. position at time 21.7s; e) Viscosity vs. position at time 21.7s; f) Shear stress vs. position at time 21.7s.	161

Nomenclature

a	Constant
A_i	Local area
b	Constant
Bi_c, Bi_p	Biot number for infinite cylinder and plane wall
C_n	Coefficient
C_p	Specific heat
D	Diameter of the pellet
\overline{D}	Strain rate tensor
F	Volume concentration
h	Heat transfer coefficient
h_i	Local heat transfer coefficient
\overline{h}	Time-averaged mean heat transfer coefficient
$\overline{h}(t)$	Mean heat transfer coefficient at time t
J_0, J_1	Bessel functions of the first kind
k	Thermal conductivity
L	Length of the pellet
m	Constant
\overline{Nu}_D	Mean Nusselt number
P	Pressure
Pr_D	Prandtl number
q_i''	Local heat flux
Re_D	Reynolds number
s	Laplace transform variable
t	Time
Δt	Time interval
T	Temperature

T_{3-D}	Temperature from 3D simulation
$T_{3-D,s}$	Shifted temperature from 3D simulation
T_g	Glass transition temperature
T_i	Local temperature
T_m	Measured temperature or melting temperature
$T_{m,s}$	Shifted temperature from measurement
T_{ref}	Reference temperature
U_x	x component velocity
ΔU_x	Velocity difference
U_y	y component velocity
V	Velocity vector

Greek Letters

α	Thermal diffusivity
$\dot{\gamma}$	Shear rate
θ	Dimensionless temperature from finite cylinder
θ_c^*, θ_p^*	Dimensionless temperature from infinite cylinder and plane wall
θ_m	Dimensionless temperature from the measurement
η	Viscosity
η_0	Zero shear rate viscosity
ξ_n	Roots of transcendental equation
ρ	Density
τ	Time constant for thermocouple
$\bar{\tau}, \tau$	Stress tensor
ω	Frequency

Chapter 1

Introduction

1.1 A brief history of polymer blends

Polymer refers to any high molecular weight compound that consists of smaller repeated linked units (1). Natural polymers, such as natural rubber, protein, wood, leather, cotton and so on, have existed in the world long before any recorded history. Our ancestors strongly relied on natural polymer materials for clothing and shelter. Polymer as a material is also essential for our daily lives. However, the dependence of human beings on natural polymers has been gradually weakened since the success of the first synthetic polymer, Bakelite made by Baekeland in 1909 (2). In the following several decades, synthetic polymer was quickly developed as one of the most important materials for all industrialized countries. During the same time, polymer science and technology has developed as one of the major disciplines (3).

Parallel to the development of synthetic polymers, polymer blending provides another way to make new materials with enhanced performance. The first successful application of blending in polymer industry can be traced back to Thomas Hancock, who greatly improved the performance of natural rubber by mixing it with sulphur under heat (4). Compared to the synthetic method, polymer blending provides a more economical and effective way to make new materials to meet the requirement of various applications. Today, we can find all kinds of different polymer products in the market.

The house where we stay, the car we drive, the clothes we wear, and the computer in our office, all contain many polymer components. As a matter of fact, most polymer products are made of a blend of polymers instead of one polymer. Through blending, performance of polymer products is usually improved, or cost of those products is greatly reduced by using cheaper components. In the modern sense of the word, polymer blend refers to a mixture of at least two polymers (5). Although the concept of blending was applied long ago, the first commercial polymer blend was not available until 1942. This was a blend of polyvinylchloride (PVC) and acrylonitrile rubber (NBR) (6). As the cost of developing and industrializing a new polymer increased sharply, the potential value of polymer blends has attracted ever-increasing attention. In the last several decades, there were over 4,000 patents published world-wide on polymer blends every year (5). Polymer blends with special functions, such as barrier, anti-static, conductive, and antibacterial, etc. represent a new trend in the development of advanced materials. There is a wider scope for components of polymer blends, covering not only high molecular weight polymers (synthetic and natural), but also small molecular organic or inorganic substances. There is no doubt that there is a strong driving force to develop new polymer blends.

1.2 Property - morphology - processing of polymer blends

Material performance is always one of the most important factors to guide the design of new polymer blends. Performance of a polymer blend depends on its components, including polymers and other additives or agents, and the blending process. Morphology of a polymer blend is the result of interaction of its components under

certain processing conditions. Different processing conditions could result in completely different performances even for the same polymer blend system. Therefore, properties of a polymer blend, the process to make it, and the morphology of the polymer blend are strongly correlated with each other (5, 7~15). Intelligent choice of its component polymers, and use of the right method to process them is necessary to make a polymer blend with desired properties.

Three major methods are used in industry to prepare polymer blends: melt mixing, solution mixing, and dry mixing. Melt mixing in extruders is the dominant method to make polymer blends in industry mainly due to its low cost, continuous operation, and high mixing efficiency (5, 7). Two types of extruders are widely used in polymer industry, viz., single screw extruder (SSE) and twin screw extruder (TSE). This thesis focuses only on the melt mixing in extruders, especially in TSE. Numerous studies have been reported to connect properties of polymer blends with their morphologies (16~25). Improvement of mechanical properties, such as toughness, temperature resistance, tensile strength, stiffness, elongation at break, and so on, continues to be one trend in the current development of polymer blends (16, 17, 19, 22, 24, 26). Taking the toughness as an example, it is widely accepted that to make a toughened polymer blend, the average distance between dispersed particles has to reach a minimum critical value (16, 17, 19). The dispersed particle size and its distribution in the matrix phase were often monitored to improve the toughness of polymer blends (13, 16, 26, 27, 28, 29). Besides mechanical property improvement, polymer blends with certain functions, such as permeability barrier, conductive, antistatic, flame retardant, antibacterial, and so on, represent another trend in the design of new polymer products

(18, 21, 23, 24, 30~34). Lamellar morphology is usually expected to make a polymer blend with permeability barrier function (18, 23), while a co-continuous morphology is often pursued to make conductive or antistatic polymer blends (21, 24, 30, 31).

Generally speaking, morphology of a polymer blend is determined by two factors: properties of its components (5, 11, 16, 23, 35, 36) and processing conditions (9~12, 14, 37, 38). Morphology is the result of interaction between components during processing. Interfacial interaction between polymers was extensively investigated to study morphology generation of polymer blends (16, 39, 40, 41, 42). Several methods, such as addition of small molecule weight interfacial agents (20, 43, 44), grafting functional groups on polymer chains (10, 11, 16, 17, 45), and using co-polymers or block copolymers as compatibilizer (12, 14, 46, 47), have proved to be very useful to modify or control morphology of polymer blends. For most commercial polymer blends, the thermodynamic steady state morphology cannot be reached mainly due to the large molecular dimensions of polymer chains and short processing time (5, 7). Therefore, morphology of a polymer blend is also highly dependent on the operating conditions and processing procedures. As a benefit of this, a variety of morphologies, thus various performances, can be obtained by changing the processing conditions or procedures even for the same polymer blend system.

Study of morphology development of polymer blends during processing has attracted much attention in the last few decades. Experimental investigations have shown that the major morphology change occurs during the melting or softening process (48~55). The initial morphology development consists of sheet formation of dispersed phase and breakup of the sheets into particles. As more particles of the

dispersed phase are present in the later stage of the morphology development, drop coalescence compete with drop breakup to determine the final morphology of a polymer blend (56~ 60).

Prediction of morphology development of polymer blends has been restricted to the molten state for both matrix and dispersed polymers mainly due to the poor understanding of their melting behavior during blending and the complex geometry within which the polymer blend was processed (59~62). One method is to divide the flow into different zones based on the local flow information (such as shear rates). Passage of melt through these zones is used to model the flow in batch or continuous mixers (62~ 64). Another method is to simplify the flow in extruders using unwound geometries (59~ 61). These models predict the morphology development of polymer blends based on drop breakup and coalescence theories for generalized Newtonian liquids. Ignoring the effects of melting and non-Newtonian behavior of polymer melts on morphology certainly is not an acceptable assumption for models to accurately predict polymer blend morphology through melt blending. Therefore, a clear understanding of polymer melting is essential before a model can be built to predict morphology development of polymer blends during processing.

1.3 Polymer melting in extrusion

Most commercial polymers are semi-crystalline or amorphous polymers. Theoretically speaking, there is no melting point for amorphous polymers. Instead they have a wide range of softening temperatures. In this thesis, “melting” is used for both

semi-crystalline and amorphous polymers to indicate the transition from a solid-like state to a liquid-like state during processing. In this way, we will not need to emphasize “melting” for semi-crystalline polymers and “softening” for amorphous polymers each time.

After solid polymer pellets are added inside the channel of an extruder, they are heated up through contact with the hot barrel and friction with the screw of the extruder. With enough heat, some pellets start melting at the surface and slide against the barrel or the screw. Then, a mixture of solid pellets and polymer melt is formed and conveyed through the channel (65~70). The time to complete the melting process depends on the polymers and the operating conditions. Sometimes, the melting process occurs over the entire length of the extruder.

Study of the melting phenomena in single screw extruders has a relatively long history (65, 71~76). A full description of the melting behavior of polymers in single extruders can be found from Tadmor and co-workers (65, 71), Lindt's group (74, 75), and Han and co-workers (72, 76). However, comprehensive studies of melting in TSE started only around two decades ago with Todd (77). Since then, the study of the melting phenomena in the TSE has attracted much attention mainly due to the wide application of TSE in industry (55, 67, 78~91). It is generally accepted that the mechanical energy plays a critical role for the fast melting of polymers in the TSE (7). Three major mechanisms are reported to convert mechanical energy from the motor to heat, leading to melting of polymers in TSE. They are: solid friction between polymers and the screw or between solid polymer pellets; plastic deformation; and viscous dissipation (65, 67, 71, 77, 82, 89, 90). However, the quantification of heat generation

from each mechanism and the heat transfer rate to solid polymers during extrusion remains a huge challenge to the polymer processing community.

The study of melting in TSE covers not only how heat is generated and transferred to polymers, but also how melting is initiated and propagated in the extrusion channel (77, 79, 90, 92~96). The melting process can be initiated by the hot barrel or via friction between polymer pellets or by the movement of polymer pellets against the screw (7, 65, 90). After melting is initiated, a polymer melt suspension with solid polymer pellets is usually formed (67, 77, 85, 87). Todd (77) observed that material was peeled off from solid polymer pellets like an onion through contact with their neighbors, and through this mechanism, the size of pellets was reduced. A similar mechanism was also reported by other authors (97). However, this is not the only mechanism through which the melting process is propagated, especially after the polymer pellets are softened in the fully filled channel (98). More work is needed to determine how the melting process propagates, and how melting and the morphology development are related to each other. Furthermore, a clear understanding of the melting process is also critical for optimization of industrial blending operations, or design of new blending equipment.

1.4 Objectives of the thesis

This thesis focuses on the melting process of polymer blends in extruders, especially in TSE. The major objective of this research is to investigate how heat is generated and transferred to solid polymers during extrusion, and what the

consequences are to the solid polymers under the heat and complex flow in the channel of extruders.

The typical flow for the study of polymer melting in TSE is a mixture of solid polymer pellets with polymer melt. Several fundamental questions about quantification of heat balance for the polymer flow during melting are still open; such as heat transfer coefficient between solid polymer pellets and polymer melt under complex flow, solid friction or deformation energy consumption, and viscous dissipation of polymer melt suspension with solid polymer pellets.

Four major topics will be addressed in this thesis. The first one is the melting behavior of polymer blends in TSE. The second one is heat transfer between solid polymer pellet and polymer melt under complex flow. The third one is rheological properties of polymer melt suspensions with solid polymer pellets. The last one is related to the morphology development of polymer blends during melting.

1.5 Structure of the thesis

The thesis consists of six chapters. Chapter 1 is an introduction to the subject area. Chapter 2 will integrate all chapters under the title of melting phenomena in polymer blending. A detailed description will be provided to show the melting behaviors of polypropylene (PP) and polystyrene (PS) blends in TSE based on on-line measurements and a perturbation method. Different heat sources during extrusion will be covered. This chapter will also introduce the following research topics related to the melting process: heat transfer coefficient from the molten polymer to the solid polymer,

rheological properties of the suspension flow, and morphology development during melting.

In chapter 3, numerical simulations will be presented to obtain the heat transfer coefficient between a solid polymer pellet and another polymer melt under a complex flow similar to that found in TSE. The simulation results will be checked with corresponding experimental data. A match between the simulation and experiment will be demonstrated after taking the thermocouple's time constant into account.

A suspension of polymer melt with solid polymer pellets is usually formed during melting in TSE. Viscous dissipation can be one of the major heat sources to melt polymers. In chapter 4, a model polymer melt suspension, ethylene acrylate copolymer (EAC) melt with PS beads, is introduced for the rheological study of such suspensions. Sandwich structure suspension samples are used to simulate the polymer flow structure during melting in TSE. Rheological properties of homogeneous suspension samples are also tested for comparison.

In chapter 5, on-line observation of the morphology development of polyethylene/polycarbonate (PE/PC) blends during melting in TSE will be presented. Two-dimensional and three-dimensional physical models will be built for numerical simulations to study PC drop deformation and breakup in PE melt under shear flow. It will be shown that numerical simulations provide another powerful tool to study the morphology development of polymer blends during processing.

The melting of polymers in TSE is a very complex process. Each chapter from 2 to 5 in this thesis can be considered as an independent research project. However, all of them are related to polymer melting during blends processing. The major findings of

this study will be summarized in Chapter 6. In the last chapter, I will discuss future work related to the melting process or other research projects derived from this study.

1.6 References

1. Rudin, A., *The elements of polymer science and engineering*, 2ed Edition, Academic Press, New York (1999).
2. Baekeland, L. H., "Method of making insoluble products of phenol and formaldehyde," *US Pat.*, No. 942,699 (1909).
3. Mark, H., *History of polymer science and technology*, Raymond B. Seymour, ED., Marcel Dekker, Inc., New York (1982).
4. Hancock, T., *Engl. Pat.*, No. 11,147 (1846).
5. Utracki, L. A., *Polymer alloys and blends: thermodynamics and rheology*, Hanser publishers, New York (1990).
6. Badum, E., "Ozone resistant cable insulation," *US Pat.*, No. 2,297,194 (1942).
7. Tadmor, Z., C. G. Gogos, *Principles of polymer processing*, John Wiley & Sons, New York (1979).
8. Imagawa, A., T. C. Qui, "Structure-property relationship of polymer blends with co-continuous structures prepared by photo-cross-linking," *Macromolecules*, **28**, 8388 (1995).
9. Petrovic, Z. S., R. Farris, "Structure-property relationship in fibers spun from poly(ethylene-terephthalate) and liquid-crystalline polymer blends. 1. The effect of composition and processing on fiber morphology and properties," *J. Appl. Polym. Sci.*, **58**, 1077 (1995).
10. Pesneau, I., A. A. Kadi, M. Bousmina, et al. "From polymer blends to in situ polymer/polymer composites: Morphology control and mechanical properties." *Polym. Eng. Sci.*, **42**, 1990 (2002).
11. Huang, W. Y., J. W. Shen, X. M. Chen, "Effect of composition on phase morphology and mechanical properties of PP/PA66 in situ composites via extrusion-drawing-injection method." *J. Mater. Sci.*, **38**, 541 (2003).
12. Fortelny, I., D. Hlavata, J. Mikesova, et al. "Effect of mixing conditions on the morphology and properties of Polystyrene/Polyethylene blends compatibilized with styrene-butadiene block copolymers," *J. Polym. Sci., Pol. Phys.*, **41**, 609 (2003).

13. Premphet, K., W. Paecharoenchai, "Polypropylene/metallocene ethylene-octene copolymer blends with a bimodal particle size distribution: Mechanical properties and their controlling factors," *J. Appl. Polym. Sci.*, **85**, 2412 (2002).
14. Garcia, M., J. I. Eguiavabal, J. Nazabal, "Processability, morphology and mechanical properties of glass fiber reinforced poly(ether sulfone) modified by a liquid crystalline copolyester," *Polym. Composite*, **24**, 686 (2003).
15. Zheng, X. J., J. Zhang, J. S. He, "Mutual influence of the morphology and capillary rheological properties in nylon/glass-fiber/liquid-crystalline-polymer blends," *J. Polym. Sci., Pol. Phys.*, **42**, 1619 (2004).
16. Wu, S., "Phase-Structure and Adhesion in Polymer Blends - A Criterion for Rubber Toughening," *Polymer*, **26**, 1855 (1985).
17. Montiel, A. G., H., Keskkula, D. R. Paul, "Impact-Modified Nylon-6 Polypropylene Blends. 1. Morphology - Property Relationships," *Polymer*, **36**, 4587 (1995).
18. Subramanian, P. M., "Permeability Barriers by Controlled Morphology of Polymer Blends," *Polym. Eng. Sci.*, **25**, 483 (1985).
19. Bucknall, C. B., F. P. Cote, I. K. Partridge, "Rubber Toughening of Plastics. 9. Effects of Rubber Particle-Volume Fraction on Deformation and Fracture in HIPE," *J. Mater. Sci.*, **21**, 301 (1986).
20. Chandramouli, K., S. A. Jabarin, "Morphology and property relationships in ternary blends of polyethylene polyamide-6 compatibilizing agents," *Adv. Polym. Tech.*, **14**, 35 (1995).
21. Lee, J. C., T. Ikehara, T. Nishi, "Morphology and electrical properties of carbon black-filled poly(epsilon-caprolactone)/poly(vinyl butyral) blends," *J. Appl. Polym. Sci.*, **69**, 193 (1998).
22. Xie, Z. M., J. Sheng, Z. M. Wan, "Mechanical properties and morphology of polypropylene/polystyrene blends," *J. Macromol. Sci. Phys.*, **40**, 251 (2001).
23. Yeo, J. H., C. H. Lee, C. S. Park, et al. "Rheological, morphological, mechanical, and barrier properties of PP/EVOH blends," *Adv. Polym. Tech.*, **20**, 191 (2001).
24. Thongruang, W., R. J. Spontak, C. M. Balik, "Bridged double percolation in conductive polymer composites: an electrical conductivity, morphology and mechanical property study," *Polymer*, **43**, 3717 (2002).

25. Bai, S. L., G. T. Wang, J. M. Hiver, et al. "Microstructures and mechanical properties of polypropylene/polyamide 6/polyethelene-octene elastomer blends," *Polymer*, **45**, 3063 (2004).
26. Luo, J. J., I. M. Daniel, "Characterization and modeling of mechanical behavior of polymer/clay nanocomposites," *Compos. Sci. Technol.*, **63**, 1607 (2003).
27. Bucknall, C. B., P. Davies, and I. K. Partridge, "Rubber Toughening of Plastics. 11. Effects of Rubber Particle-Size and Structure on Yield Behavior of HIPS," *J. Mater. Sci.*, **22**, 1341 (1987).
28. Cho, Y. G., M. R. Kamal, "Effect of the dispersed phase fraction on particle size in blends with high viscosity ratio," *Polym. Eng. Sci.*, **42**, 2005 (2002).
29. Zeng, J. J., M. Aoyama, H. Takahashi, "Effect of the composition on the phase size in immiscible blends with the viscosity ratio close to unity," *J. Appl. Polym. Sci.*, **89**, 1791 (2003).
30. Lee, B. L., "Electrically conductive polymer composites and blends," *Polym. Eng. Sci.*, **32**, 36 (1992).
31. Zhang, Q. H., D. J. Chen, "Percolation threshold and morphology of composites of conducting carbon black/polypropylene/EVA," *J. Mater. Sci.*, **39**, 1751 (2004).
32. Lu, J., M. A. Hill, M. Hood, et al. "Formation of antibiotic, biodegradable polymers by processing with Irgasan DP300R (Triclosan) and its inclusion compound with beta-cyclodextrin," *J. Appl. Polym. Sci.*, **82**, 300 (2001).
33. Sohn, J. I., S. T. Lim, S. H. Park, et al. "Effect of a reactive-type flame retardant on rheological and mechanical properties of PC/ABS blends," *J. Mater. Sci.*, **38**, 1485 (2003).
34. Kashiwagi, T., R. H. Harris, X. Zhang, et al. "Flame retardant mechanism of polyamide 6-clay nanocomposites," *Polymer*, **45**, 881 (2004).
35. Oshinski, A. J., H. Keskkula, and D. R. Paul, "The Role of Matrix Molecular Weight in Rubber Toughened Nylon 6 Blends .1. Morphology," *Polymer*, **37**, 4891 (1996).
36. Moly, K. A., Z. Oommen, S. S. Bhagawan, et al. "Melt rheology and morphology of LLDPE/EVA blends: Effect of blend ratio, compatibilization, and dynamic crosslinking," *J. Appl. Polym. Sci.*, **86**, 3210 (2002).

37. Sundararaj, U., "Effect of Processing Parameters on Phase Inversion during Polymer Blending," *Rev. Makrom. Chem. Makrom. Symp.*, **112**, 85 (1996).
38. Kallel, T., V. Massardier-Nageotte, M. Jaziri, et al. "Compatibilization of PE/PS and PE/PP blends. I. Effect of processing conditions and formulation," *J. Appl. Polym. Sci.*, **90**, 2475 (2003).
39. Wu, S., "Formation of dispersed phase in incompatible polymer blends: Interfacial and rheological effects," *Polym. Eng. Sci.*, **27**, 335 (1987).
40. Lacasse, C., B. D. Favis, "Interface/morphology/property relationships in polyamide-6/ABS blends," *Adv. Polym. Tech.*, **18**, 255 (1999).
41. Chaffin, K. A., F. S. Bates, P. Brant, et al. "Semicrystalline blends of polyethylene and isotactic polypropylene: Improving mechanical performance by enhancing the interfacial structure," *J. Polym. Sci., Pol. Phys.*, **38**, 108 (2000).
42. Fisher, I., A. Siegmann, M. Narkis, "The effect of interface characteristics on the morphology, rheology and thermal behavior of three-component polymer alloys," *Polym. Composite*, **23**, 34 (2002).
43. Jang, S. P., D. Kim, "Thermal, mechanical, and diffusional properties of nylon 6/ABS polymer blends: Compatibilizer effect," *Polym. Eng. Sci.*, **40**, 1635 (2000).
44. Willis, J. M., V. Caldas, and B. D. Favis, "Processing Morphology Relationships of Compatibilized Polyolefin Polyamide Blends 2: The Emulsifying Effect of an Ionomer Compatibilizer as a Function of Blend Composition and Viscosity Ratio," *J. Mater. Sci.*, **26**, 4742 (1991).
45. Shi, D., Z. Ke, J. H. Yang, et al. "Rheology and morphology of reactively compatibilized PP/PA6 blends," *Macromolecules*, **35**, 8005 (2002).
46. Cigana, P., B. D. Favis, C. Albert, et al. "Morphology-interface-property relationships in polystyrene/ethylene-propylene rubber blends. 1. Influence of triblock copolymer interfacial modifiers," *Macromolecules*, **30**, 4163 (1997).
47. Chuai, C. Z., S. Li, K. Almdal, et al. "Influence of diblock copolymer on the morphology and properties of polystyrene/poly(dimethylsiloxane) blends," *J. Appl. Polym. Sci.*, **92**, 2747 (2004).

48. Scott, C. E., C. W. Macosko, "Model Experiments Concerning Morphology Development during the Initial-Stages of Polymer Blending," *Polym. Bull.*, **26**, 341 (1991).
49. Lindt, J. T., A. K. Ghosh, "Fluid mechanics of the formation of polymer blends. Part 1: Formation of lamellar structures," *Polym. Eng. Sci.*, **32**, 1802 (1992).
50. Sundararaj, U., C. W. Macosko, R. J. Rolando, H. T. Chan, "Morphology Development in Polymer Blends," *Polym. Eng. Sci.*, **32**, 1814 (1992).
51. Scott, C. E., C. W. Macosko, "Morphology development during the initial stages of polymer-polymer blending," *Polymer*, **36**, 461 (1995).
52. Sundararaj, U., Y. Dori, C. W. Macosko, "Sheet formation in immiscible polymer blends: model experiments on initial blend morphology," *Polymer*, **36**, 1957 (1995).
53. Li, H. X., G. H. Hu, and J. A. Sousa, "The Early Stage of the Morphology Development of Immiscible Polymer Blends During Melt Blending: Compatibilized vs. Uncompatibilized Blends," *J. Polym. Sci. Pol. Phys.*, **37**, 3368 (1999).
54. Potente, H., S. Krawinkel, M. Bastian, M. Stephan, P. Potschke, "Investigation of the Melting Behavior and Morphology Development of Polymer Blends in the Melting Zone of Twin-Screw Extruders," *J. Appl. Polym. Sci.*, **82**, 1986 (2001).
55. Potente, H., M. Bastian, K. Bergemann, M. Senge, G. Scheel, T. Winkelmann, "Morphology of Polymer Blends in the Melting Section of Co-Rotating Twin Screw Extruders," *Polym. Eng. Sci.*, **41**, 222 (2001).
56. Utracki, L. A., Z. H. Shi, "Development of Polymer Blend Morphology During Compounding in a Twin-Screw Extruder 1: Droplet Dispersion and Coalescence - A Review," *Polym. Eng. Sci.*, **32**, 1824 (1992).
57. Grace, H. P., "Dispersion Phenomena in High Viscosity Immiscible Fluid Systems and Application of Static Mixers as Dispersion Devices in Such Systems," *Chem. Eng. Commun.*, **14**, 225 (1982).
58. Sundararaj, U., C. W. Macosko, "Drop Breakup and Coalescence in Polymer Blends," *Macromolecules*, **28**, 2647 (1995).
59. Shi, Z. H., L. A. Utracki, "Development of Polymer Blend Morphology during Compounding in a Twin-Screw Extruder. 2. Theoretical Derivations," *Polym. Eng. Sci.*, **32**, 1834 (1992).

60. Huneault, M. A., Z. H. Shi, L. A. Utracki, "Development of Polymer Blend Morphology during Compounding in a Twin-Screw Extruder. 4. A New Computational Model with Coalescence," *Polym. Eng. Sci.*, **35**, 115 (1995).
61. Delamare, L., B. Vergnes, "Computation of the Morphological Changes of a Polymer Blend Along a Twin-Screw Extruder," *Polym. Eng. Sci.*, **36**, 1685 (1996).
62. Li, H., G. Hu, "A Two-Zone Melting Model for Polymer Blends in a Batch Mixer," *Polym. Eng. Sci.*, **41**, 763 (2001).
63. Tadmor, Z., "Number of Passage Distribution Functions with Application to Dispersive Mixing," *AIChE. J.*, **34**, 1943 (1988).
64. DeRoussel, P., D. V. Khakhar, J. M. Ottino, "Mixing of Viscous Immiscible Liquids. Part 1: Computational Models for Strong-Weak and Continuous Flow Systems," *Chem. Eng. Sci.*, **56**, 5511 (2001).
65. Tadmor, Z., "Fundamentals of plasticating Extrusion," *Polym. Eng. Sci.*, **7**, 185 (1966).
66. Broyer, E., Z. Tadmor, "Solids Conveying in Screw Extruders Part 1: A Modified Isothermal Model," *Polym. Eng. Sci.*, **12**, 12 (1972).
67. Potente, H., U. Melishc, "Theoretical and Experimental Investigations of the Melting of Pellets in Co-Rotating Twin-Screw Extruders," *Intern. Polym. Process.*, **2**, 101 (1996).
68. Chiruvella, R. V., Y. Jaluria, M. V. Karwe, V. Sernas, "Transport in a Twin-Screw Extruder for the Processing of Polymers," *Polym. Eng. Sci.*, **36**, 1531 (1996).
69. Yung, K. L., Y. Xu, K. H. Lau, "A Transient Melting Model of Polymer Balls Sliding Against the Barrel," *Intern. Polym. Process.*, **2**, 108 (2001).
70. Zhu, L., K. A. Narh, X. Geng, "Modeling of Particle-Dispersed Melting Mechanism and Its Application in Corotating Twin-Screw Extrusion," *J. Polym. Sci., Pol. Phys.*, **39**, 2461 (2001).
71. Tadmor, Z., I. J. Duvdevani, I. Klein, "Melting in Plasticating Extruders Theory and Experiments," *Polym. Eng. Sci.*, **7**, 198 (1967).
72. Lee, K. Y., C. D. Han, "Analysis of the Performance of Plasticating Single-Screw Extruders With a New Concept of Solid-Bed Deformation," *Polym. Eng. Sci.*, **30**, 665 (1990).

73. Lai, E., D. Yu, "Modeling of the Plasticating Process in a Single-Screw Extruder: A Fast-Track Approach," *Polym. Eng. Sci.*, **40**, 1074 (2000).
74. Elbirli, B., J. T. Lindt, S. R. Gottgetreu, S. M. Baba, "Mathematical Modeling of Melting of Polymers in a Single-Screw Extruders," *Polym. Eng. Sci.*, **24**, 988 (1984).
75. Lindt, J. T., B. Elbirli, "Effect of the Cross-Channel Flow on the Melting Performance of a Single-Screw Extruder," *Polym. Eng. Sci.*, **25**, 412 (1985).
76. Han, C. D., K. Y. Lee, N. C. Wheeler, "Plasticationg Single-Screw Extrusion of Amorphous Polymer: Development of a Mathematical Model and Comparison With Experiment," *Polym. Eng. Sci.*, **36**, 1360 (1996).
77. Todd, D. B., "Melting of Plastics in Kneading Blocks," *Intern. Polym. Process.*, **8**, 113 (1993).
78. Sakai, T., "The Development of On-Line Techniques and Novel Processing Systems for the Monitoring and Handling of the Evolution of Microstructure in Nonreactive and Reactive Polymer Systems," *Adv. Polym. Tech.*, **14**, 277 (1995).
79. Bawiskar, S., J. L. White, "Solids Conveying and Melting in a Starved Fed Self-Wiping Co-Rotating Twin Screw Extruder," *Intern. Polym. Process.*, **10**, 105 (1995).
80. Cho, J. W., J. L. White, "Melting and Blending in a Modular Co-Rotating/Counter-Rotating Twin Screw Extruder," *Intern. Polym. Process.*, **11**, 21 (1996).
81. Bawiskar, S., J. L. White, "A Composite Model for Solid Conveying, Melting, Pressure and Fill Factor Profiles in Modular Co-Rotating Twin Screw Extruders," *Intern. Polym. Process.*, **12**, 331 (1997).
82. Gogos, C. C., Z. Tadmor, M. H. Kim, "Melting Phenomena and Mechanisms in Polymer Processing Equipment," *Adv. Polym. Tech.*, **17**, 285 (1998).
83. Bawiskar, S., J. L. White, "Melting Model for Modular Self Wiping Co-Rotating Twin Screw Extruders," *Polym. Eng. Sci.*, **38**, 727 (1998).
84. Potente, H., M. Bastian, "Polymer Blends in Co-Rotating Twin-Screw Extruders," *Intern. Polym. Process.*, **16**, 14 (2001).
85. Vergnes, B., G. Souveton, M. L. Delacour, A. Ainsier, "Experimental and Theoretical Study of Polymer Melting in a Co-Rotating Twin Screw Extruder," *Inter. Polym. Process.*, **16**, 351 (2001).

86. Carneiro, O. S., A. Poulesquen, J. A. Covas, B. Vergnes, "Visualization and Analysis of the Flow along the Kneading Block of a Twin-Screw Extruder," *Intern. Polym. Process.*, **17**, 301 (2002).
87. Zhu, L., X. Geng, "Experimental Investigation of Polymer Pellets Melting Mechanisms in Co-rotating Twin-Screw Extrusion," *Adv. Polym. Tech.*, **21**, 188 (2002).
88. Wetzel, M. D., "Experimental Study of LDPE Melting in a Twin-Screw Extruder Using On-Line Visualization and Axial Pressure and Temperature Measurement," *SPE ANTEC Tech. Papers* (2002).
89. Qian, B., D. B. Todd, C. G. Gogos, "Plastic Energy Dissipation and Its Role on Heating/Melting of Single-Component Polymers and Multi-Component Polymer Blends," *Adv. Polym. Tech.*, **22**, 85 (2003).
90. Jung, H., J. L. White, "Investigation of Melting Phenomena in Modular Co-Rotating Twin Screw Extrusion," *Intern. Polym. Process.*, **18**, 127 (2003).
91. Wilczynski, K., J. L. White, "Melting Model for Intermeshing Counter-Rotating Twin-Screw Extruders," *Polym. Eng. Sci.*, **43**, 1715 (2003).
92. White, J. L., Z. Chen, "Simulation of Non-Isothermal Flow in Modular Co-Rotating Twin Screw Extrusion," *Polym. Eng. Sci.*, **34**, 229 (1994).
93. White, J. L., E. K Kim, J. M. Keum, H. C. Jung, "Modeling Heat Transfer in Screw Extrusion With Special Application to Modular Self-Wiping Co-Rotating Twin-Screw Extrusion," *Polym. Eng. Sci.*, **41**, 1448 (2001).
94. Sastrohartono, T., Y. Jaluria, and M. V. Karwe, "Numerical Simulation of Fluid Flow and Heat Transfer in Twin-Screw Extruders for Non-Newtonian Materials." *Polym. Eng. Sci.*, **35**, 1213 (1995).
95. Tenge, S., D. Mewes, "Experimental Investigation of the Energy Balance for the Metering Zone of a Twin-Screw Extruder," *Polym. Eng. Sci.*, **40**, 277 (2000).
96. Kim, E. K., J. L. White, "Isothermal Transient Startup of a Starved Flow Modular Co-Rotating Twin Screw Extruder," *Polym. Eng. Sci.*, **40**, 543 (2000).
97. Lin, B., U. Sundararaj, F. Mighri, M. A. Huneault, "Erosion and Breakup of Polymer Drops under Simple Shear in High Viscosity Ratio Systems," *Polym. Eng. Sci.*, **43**, 891 (2003).

98. Lin, B., F. Mighri, M. A. Huneault, U. Sundararaj, "Parallel Breakup of Polymer Drops under Simple Shear," *Macro. Rapid Commun.*, **24**, 783 (2003).

Chapter 2

Melting of PS/PP blends in a twin screw extruder*

2.1 Introduction

Twin screw extruders (TSE) have been widely used in polymer industry to make polymer blends because of their low cost, high mixing efficiency and flexibility. Performance of a polymer blend depends on properties of its component polymers and the final blend morphology (1~4). The morphology development along the extrusion channel has been intensively studied by many research groups. It was found that the major morphology change occurs during the melting process (5~12). However, no satisfactory models can accurately predict the morphology development during melting mainly due to poor understanding of the melting process in TSE.

In this chapter, the melting behavior of polystyrene/polypropylene (PS/PP) blends in a co-rotating TSE was investigated. Two major factors on the melting behavior were studied in detail: a) effect of component concentration; b) effect of ratio of flow rate (Q) with screw speed (N). For the study of both factors, a sliding barrel mechanism was used to visualize the melting process in TSE through a glass window and obtain the temperature and pressure profiles along the extrusion channel. For the study of b), an additional perturbation method was used to detect the location of mechanical energy consumption in the extruder. Brief introductions of the sliding barrel

* Part of this chapter is published in two papers:

Chen, H., U. Sundararaj, K. Nandakumar, M. D. Wetzel, *Ind. Eng. Chem. Res.*, **43**, 6822 (2004)

Chen, H., U. Sundararaj, K. Nandakumar, M. D. Wetzel, *Intern. Polym. Process.*, **19**, 342 (2004)

mechanism and the perturbation method are provided before going into the details of experiments in this chapter.

2.1.1 PREVIOUS WORK

The melting phenomena of polymers in single extruders has been extensively studied by many authors (13~19). However, a comprehensive study in the TSE started only around two decades ago with Todd (20). Since then, the study of the melting phenomena in the TSE has attracted much attention (21~30). It was widely accepted that the mechanical energy plays a critical role for the fast melting of polymers in the TSE (31). However, how the mechanical energy was converted to heat to melt polymers in TSE remains an open question in the field of polymer processing. Todd (20) reported that friction between polymer pellets or particles in the kneading blocks was the major heat source to melt polymers in the TSE. An effective viscosity was estimated for the extrusion flow at the initial stage of melting. The existence of solid polymer pellets in the flow significantly increased the viscosity of the mixture (20~33). Viscous energy dissipation (VED) could be another key mechanism to generate a significant amount of heat from mechanical energy in the TSE. More recently, Gogos and his co-workers (11, 34) reported that plastic energy dissipation (PED) was the dominant heat source to melt polymers in the TSE. According to their definition, PED refers to the energy dissipation due to irreversible solid deformation of polymer pellets under pressure. Mathematical models were widely developed to predict the temperature and pressure profiles along the extrusion channel (24, 25, 32, 33). However, the mathematical representation of melting mechanisms, especially for friction between polymer pellets and for PED, remains a challenge for the polymer processing community.

The study of melting in TSE covers not only how heat is generated and transferred to polymers, but also how melting is initiated and propagated in the extrusion channel. Generally speaking, heat from the barrel combined with mechanical energy from the motor achieves unique melting phenomena in the TSE (11, 20, 31). The melting process can be initiated by the hot barrel or via friction between polymer particles (20, 29~32). White and co-workers (35, 36) reported a new melting initiation regime: melting at the screw surface. Friction between the pellets and screw surface was believed to be the source of initiation. After melting was initiated, a polymer melt suspension with solid polymer pellets was usually formed. Todd (20) observed that material was peeled off from solid polymer pellets like an onion through contact with their neighbors, and this mechanism slowly reduced the size of the pellets. A similar mechanism was also reported by other authors (31, 33). However, this is not the only mechanism through which the melting process was propagated, especially after the polymer pellets were softened in the fully filled channel (37). More work is needed to determine how the melting process propagates, and how melting and the morphology development are related.

Two methods are widely used to study the melting process in extruders. One is the so-called carcass analysis method, where samples are obtained from the screws after suddenly shutting down the machine during steady state operation. This method has been used extensively by many authors, particularly the groups of Potente (12, 26, 27, 32), Gogos (11, 34) Han (15, 19, 38), and White (22~25, 35). Melting mechanisms are formulated using the morphology of the samples obtained at different positions along the screw channel. However, it is important to note that the morphology may change

during the time between shutting down the machine and when the sample is obtained. It takes approximately 3 minutes to obtain the sample using this method (11, 12, 21).

The other method is on-line measurement of the melting process in extruders. This method provides the most direct information on melting mechanisms in the extruder. Schlatter et al. (39) designed a light scattering device to perform an online study of polymer blend morphology development in a twin-screw extruder. This device, however, was limited to use with molten polymer blends for dispersed particle sizes in the micrometer range. Therefore it is not suitable for the study of melting processes in extruders since typically a mixture of solid polymer pellets that are millimeters in size are used. Bawishar and White (22) visualized an extrusion process in a co-rotating twin screw extruder using transparent barrels made of poly(methyl methacrylate) (PMMA). Because of the limitation of mechanical properties of PMMA, only low pressure and low temperature conditions could be applied in their visualizations. In production, high pressure and high temperature are typically used in extrusion. Therefore, glass with high temperature and high pressure resistance needs to be used to make transparent windows. Industrial extrusion processes have been visualized through glass windows fitted in the barrel of the extruder. Sakai used a side window to view polypropylene (PP) melting in a TSE (21). His study also proved that morphology development is closely related to the melting process. Zhu and Geng (29) used three glass windows at different sections of an extruder to visualize twin-screw extrusion of high density polyethylene (HDPE). An island-sea melting model was found to be an important mechanism to realize a high efficiency melting process. Wetzel (30) visualized the melting of low density polyethylene (LDPE) along the length of a TSE through one glass window using a

sliding barrel mechanism, and obtained the axial temperature and pressure profiles using several transducers attached to the barrel. The effects of flow rate and screw speed on pressure profiles were also investigated.

2.1.2 SLIDING BARREL MECHANISM

In this chapter, the same sliding barrel mechanism as that used by Wetzel (30) was used to realize the on-line measurement of PP/PS blends melting behavior in a co-rotating TSE. This sliding barrel technique was first introduced by McCullough and Hilton (40), and Christiano and Lindenflezer (41) to generate dynamic pressure profiles in the TSE.

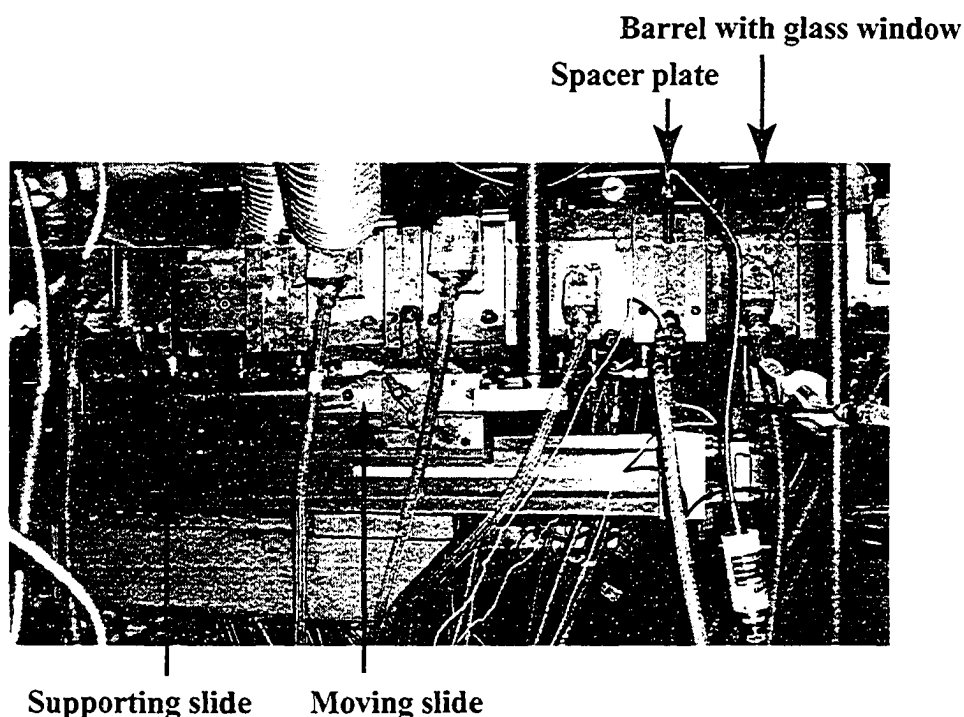


Figure 2.1 Sliding barrel mechanism for visualization.

Figure 2.1 shows how the sliding barrel technique works for the on-line measurement. The working part of a TSE is composed of three major components: motor, screws, and barrel. The screws are driven by the motor to process polymers. The

barrel provides a hot channel for polymers to be processed. In industry, the barrel is fixed to a solid base. For the sliding barrel technique, the whole barrel is mounted on two parallel slides. Therefore, the barrel can be moved along the axial direction of the extruder. Various probes, such as temperature, pressure, residence time distribution (RTD) probes, and so on, can be mounted in the barrel to monitor the process. Glass window can also be fitted in the barrel for on-line visualization. By moving the barrel along the screw, we can visualize the whole melting process through the glass window, and obtain the temperature and pressure profiles along the screw channel.

2.1.3 PERTURBATION METHOD

The perturbation method introduced by Wetzel et al. (42) was used for this study. In this method, a material mass pulse is added into the extruder feed to generate a disturbance to the steady state operation. The machine response is monitored with various probes, such as pressure transducers, thermocouples, residence time distribution (RTD) probes (43), and so on. Most important, the drive motor power is also monitored. By removing the steady state base-line values, we can obtain the response of the machine to the pulse material. Theoretically speaking, any physical or chemical changes to the pulse material should be reflected in the motor power input signals if those changes are big enough to be detected. For example, in the case of reactive blending, the motor power input will increase if the viscosity of the flow is increased due to a cross-linking reaction at certain location in the channel. The history of the pulse material in the channel can be tracked with the RTD data. Therefore, the location of the reaction in the extrusion channel can be detected by combining information from the motor power input signals and the RTD data. The motor power input signal contains

historic information about temperature, stress, and flow properties. By selecting suitable pulse material or varying the composition or amount of the pulse material, we can probe process dynamics of an extruder. An “extrusion pulse analysis system” (EPAS) was developed by Wetzel et al. (42) to enable on-line data analysis of the imposed disturbances. The pulse disturbance signals provide us information about the steady state and the dynamics of an extrusion process. Details about the structure and function of the system are provided in their paper (42).

The melting of the pulse material requires additional energy either through heat transferring from its surrounding or through mechanical energy conversion from the motor. However, only the heat from the mechanical energy is reflected in the motor power input signal. The RTD tracer pulse is added to the feed together with the material mass pulse, so that the location of the pulse material in the extrusion channel at a certain time can be tracked using the RTD data (42, 43). Therefore, the perturbation method provides a new way to study the melting mechanisms of polymer blends in the extrusion channel, and specifically, provides a method to find the location of melting in the extruder.

2.2 PS/PP (80:20) and PP/PS (80:20) blends at constant Q/N

2.2.1 EXTRUSION SETUP

The device designed by Wetzel (30) was used for this study. The 40mm extruder (Werner-Pleiderer, now Coperion ZSK) comprised nine barrel sections, and the barrel was mounted on two parallel slides. The screws inside the barrel were driven by a motor. Figure 2.1 shows the sliding mechanism used for visualization. By moving the whole barrel along the screw using the slide mechanism, we can visualize the process at different sections through a glass window fitted in one of the barrels. The glass window was contoured to the barrel shape in the apex region but there was a slight increase in clearance to prevent the screws from scratching the glass surface. The size of the window was 30mm in the axial direction and 40mm in width (see Figure 2.2). External light above the glass window was used to better visualize the extrusion process.

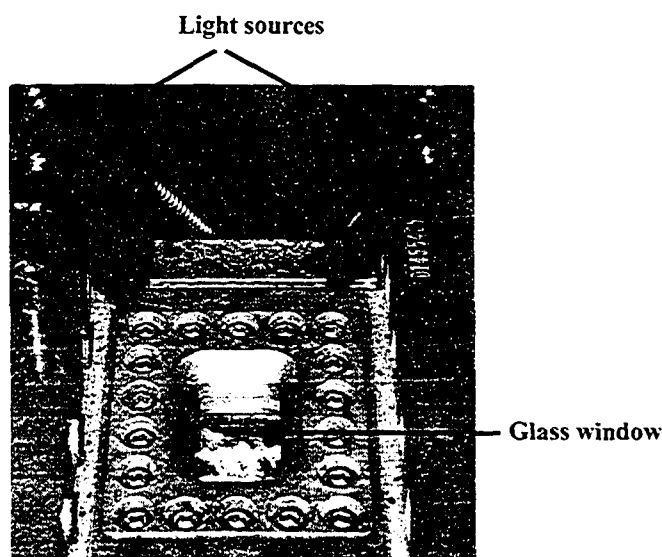


Figure 2.2 Glass window for visualization and light sources above the window.

A spacer plate with temperature and pressure probes was located 90mm upstream of the barrel fitted with the glass window. Three pressure transducers and a flush-wall type J thermocouple were mounted in the spacer plate at several angular locations as shown in Figure 2.3. The tips of probes were perpendicular and flush to the barrel surface.

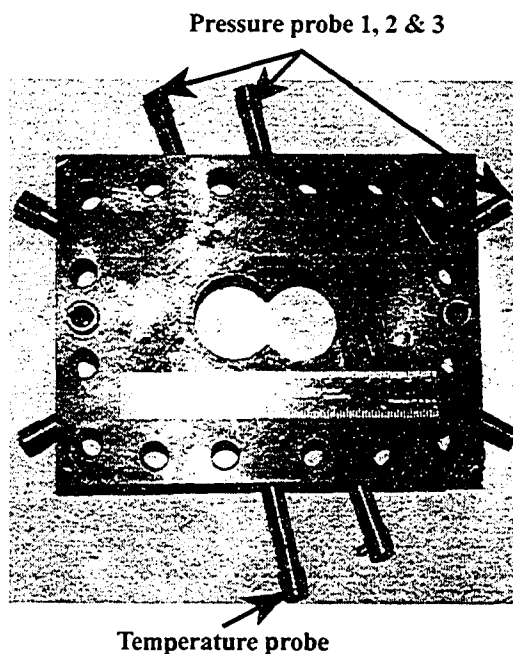


Figure 2.3 Probe locations in the spacer plate for PS/PP blends at constant Q/N .

The extruder was configured with a standard melting zone screw and was operated in an open-discharge mode for all steady state operations.

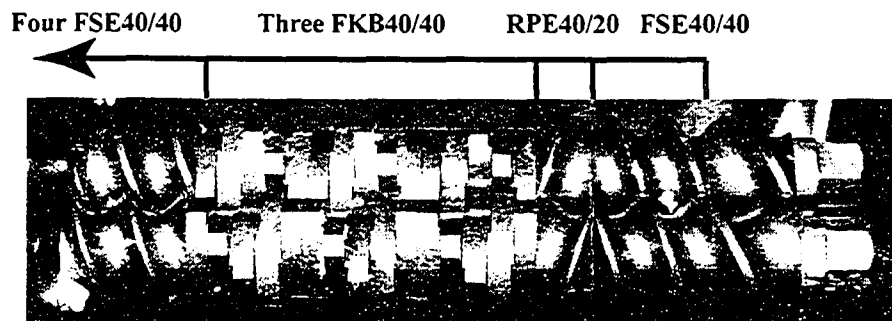


Figure 2.4 Screw configuration for the melting zone.

A photograph of the screw configuration including the melting zone region is shown in Figure 2.4 and a schematic of the screw design showing the axial location of the probe and glass window is shown in Figure 2.5. The naming convention used in the thesis for screw elements is three letters followed by two numbers. The first letter indicates if the element is forward or reverse, the last two letters indicate the type of element, the first number indicates the pitch and the second number is the length of the element in mm. The kneading section comprised of three forward 40mm 45°-staggered kneading blocks (FKB, 40/40) and a 20mm lead reverse pumping element (RPE, 40/20). There were four 40mm forward screw elements (FSE, 40/40) upstream of the kneading section and one 40mm forward screw element downstream. The axial distance between the spacer plate and the glass window was 90mm.

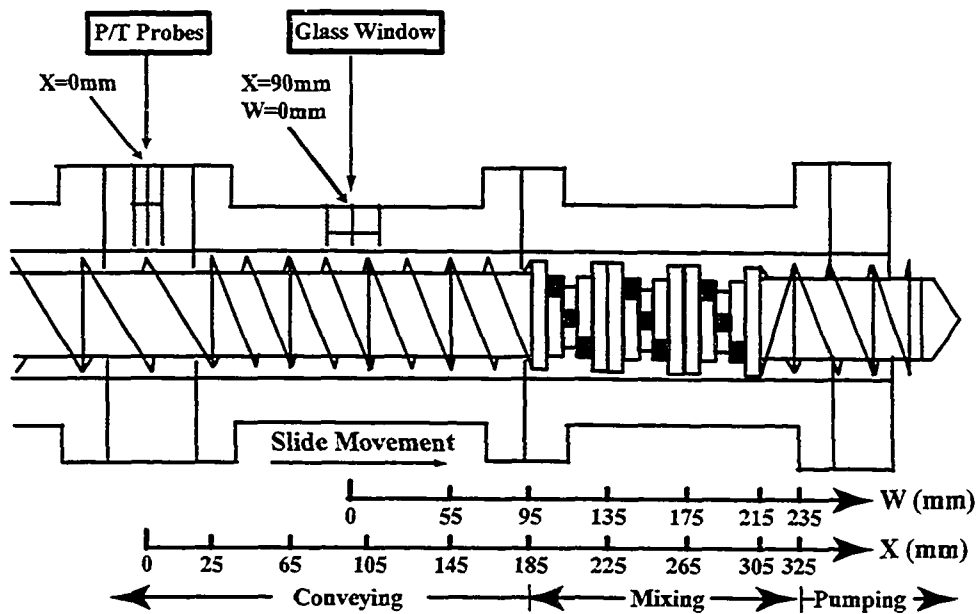


Figure 2.5 Extruder configuration and experimental setup. Note W and X axes.

Video recording above the glass window was performed at 30 frames per second. Dynamic measurements of temperature and pressure were recorded along with video images during the steady state operation at each position. Signals of pressure from different angular locations were averaged to produce a single value for each axial position. For each run, the slide was started at the retracted position ($X=0\text{mm}$). The barrel slide was moved either 10 or 20mm each time toward the end of the screw. By sliding the barrel, the glass window was able to cover the region from the solid conveying zone to the open discharge region. The operation was allowed to stabilize for at least 2 minutes at each position before recording the video, pressure and temperature data.

Table 2.1 Operating conditions for PP/PS (80:20) and PS/PP (80:20) blends at constant Q/N.

	PP/PS (80:20) blend	PS/PP (80:20) blend
Flow rate (kg/hr)	22.7	22.7
Screw speed (rpm)	50	50
Feed pellet temperature ($^{\circ}\text{C}$)	32	30
Discharge melt temperature ($^{\circ}\text{C}$)	149	159
Specific energy input (kw.hr/kg)	0.12	0.10

The specific energy input at each position was calculated using the following

equation (30):

$$\text{Specific Energy Input} = \frac{V \cdot A}{Q}$$

where V and A are the voltage and current, respectively, of the extruder motor, and Q is the flow rate. Only the averaged values for each blend are reported here since there was little variation of those values at each position. The temperatures for barrels 1 to 9

were set as ($^{\circ}\text{C}$): 50-50-50-50-170-180-200-200-200. The steady state operating conditions for each blend are listed in Table 2.1.

2.2.2 MATERIALS

Two polymers were used in this study: PP (BASELL PDC1277), with melting temperature (T_m) 168°C , and PS (BASF 168M), with glass transition temperature (T_g) 100°C . For an amorphous polymer, such as PS, there is no melting point. However, it has a flow temperature corresponding to a transition above T_g . Boyer and his co-workers extensively studied the transitions above T_g , or liquid-liquid transitions (T_{ll}) in atactic PS (44~46). They found that the flow temperature (T_f) of PS is around 50°C higher than its T_g . "Melting" for PS in this chapter refers to the transition from solid pellets to flowing liquid in TSE channel. Properties of PP and PS are summarized in Table 2.2.

Table 2.2 Properties of PP and PS.

	PP	PS
Thermal conductivity ($\text{W}/\text{m}/^{\circ}\text{C}$, 25°C)	0.21	0.16
Specific heat ($\text{J}/\text{kg}/^{\circ}\text{C}$, 25°C)	1635	913
Density (kg/m^3 , 25°C)	910	1060
Characteristic temperature ($^{\circ}\text{C}$)	168 (T_m)	100 (T_g)
Flowing temperature ($^{\circ}\text{C}$)	>168	>150
Viscosity ($\text{Pa}\cdot\text{s}$, 220°C , 60 s^{-1})	794	1319

Figure 2.6 shows the original shape of the two types of pellets. PP pellets are spherical in shape and opaque, while PS pellets are transparent short cylinders. The viscosity versus shear rate plot for PS and PP is given in Figure 2.7. Both materials are

shear-thinning and the power law coefficients are 0.39 and 0.33 for PP and PS respectively at 220⁰C. PP/PS (80:20, ratio by weight) was chosen as the model system to study the melting mechanism of an amorphous polymer dispersed in a semi-crystalline

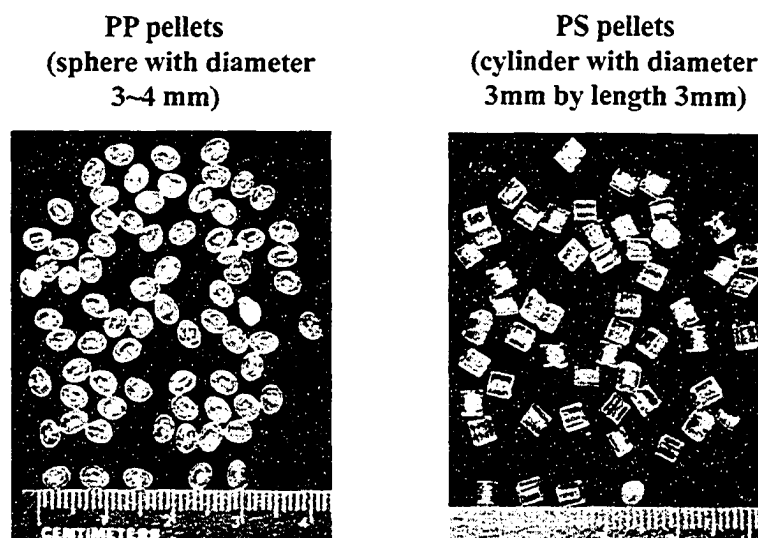


Figure 2.6 Original shape of PS and PP pellets.

polymer in an extruder; while PS/PP (80:20, ratio by weight) was chosen to study the melting mechanism of a semi-crystalline polymer dispersed in an amorphous polymer. In an industrial extrusion process, different operating conditions would be used for each of these two blends. However, in this study, the same operating conditions were used for the two blending systems to compare the melting behavior of each component. It should be noted that though the melting temperatures of the two polymers used in this study were only 15-20⁰C apart, the melting sequences changed when we changed concentration. This will be described in more details in the Results and Discussion section.

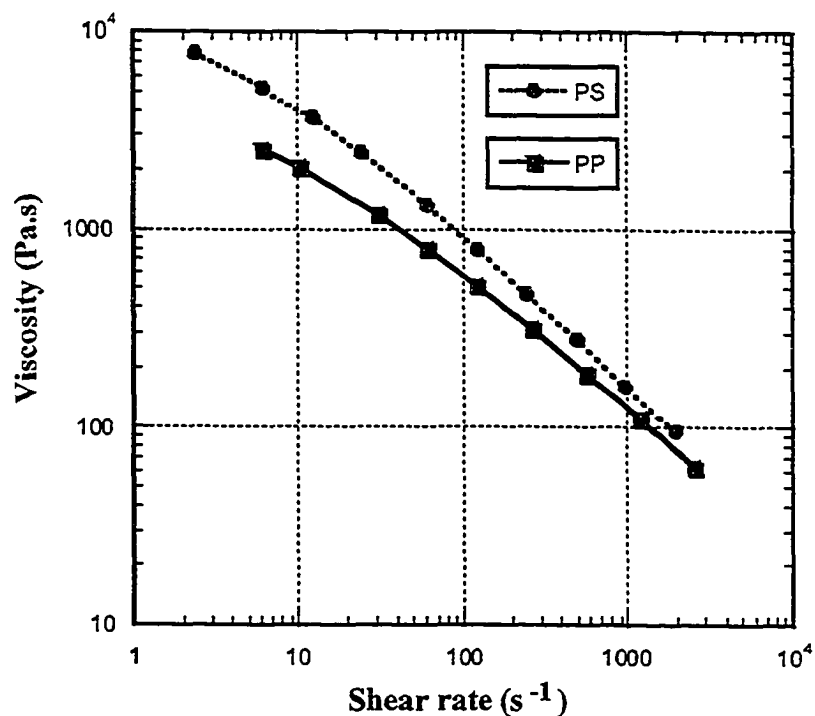


Figure 2.7 Viscosity of PS and PP at 220°C.

2.2.3 RESULTS AND DISCUSSION

2.2.3.1 PP/PS (80:20) Blend

Figure 2.8 shows images of the PP/PS (80:20) blend in the TSE. The first visualization result is taken at the second FSE 40/40 ($W=0$, $X=90$ mm, see Figure 2.5 for definition of W and X) before the kneading section. In the region $X=90$ mm to $X=130$ mm, the polymer pellets are compacted.

The extruder is fully filled in the middle of the FSE 40/40 located immediately upstream of the kneading blocks (at approximately $X=150$ mm). In the partially filled region, we cannot see any significant deformation or melting of polymer pellets.

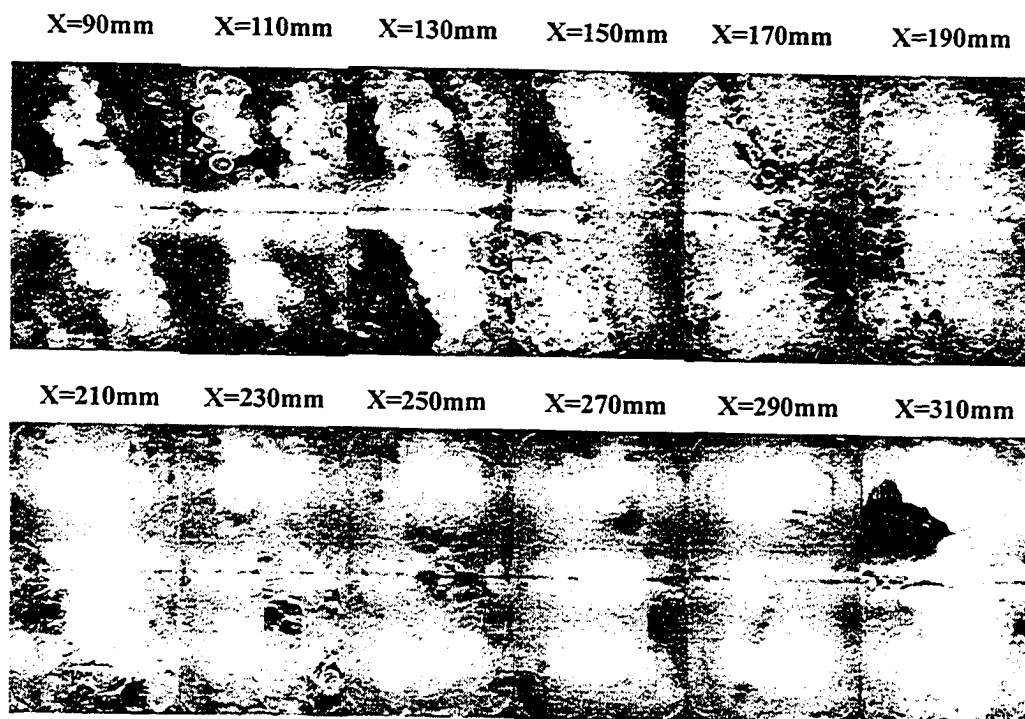


Figure 2.8 Visualization of PP/PS (80:20) blending process in the TSE. Each image begins at the value of X given and is 30mm in width. That is, for each image, there is a 10mm overlap on either side with the adjacent images.

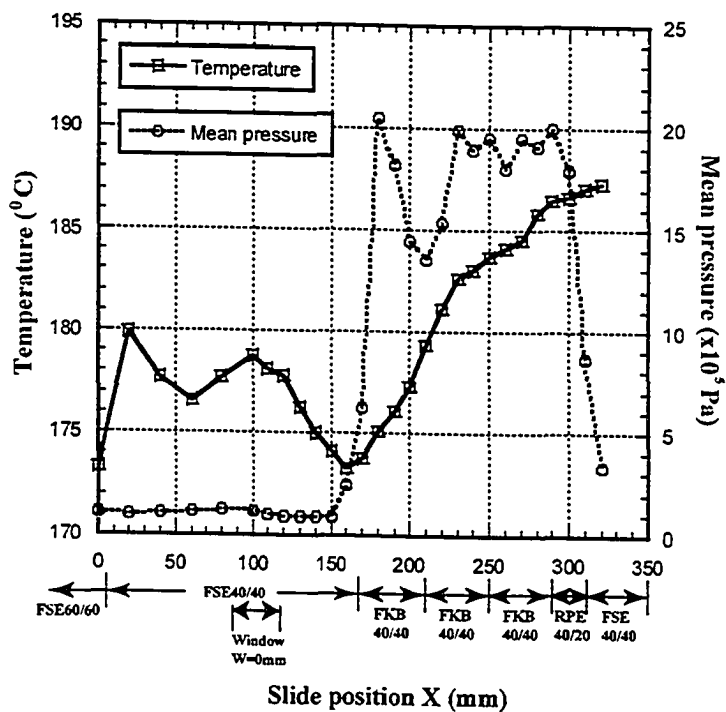


Figure 2.9 Axial temperature and pressure profiles for the extrusion of PP/PS (80:20) blend.

Even PS pellets, whose T_g is 100°C lower than the set temperature for the barrels in the region, kept their original shape. The majority of melting occurred in the region from $X=150\text{mm}$ to 270mm , and a homogeneous flow is shown at $X=290\text{mm}$ (see Figure 2.8).

Figure 2.9 shows the axial wall pressure and temperature profiles in the channel of the extruder during steady state operation. It can be seen that the pressure was constant at around one atmosphere pressure before the fully filled region ($X=150\text{mm}$). In the fully filled region, the pressure increased suddenly and then slightly decreased before finally reaching a pressure plateau at $20 \times 10^5\text{Pa}$. After the reverse pumping element (RPE), the pressure decreased abruptly back to lower levels.

The temperature curve in Figure 2.9 shows some oscillation in the region from $X=0\text{mm}$ to $X=100\text{mm}$. In the partially filled region, the flow of polymer pellets was not constant even during steady state operation and cold pellets may occasionally contact the surface. Therefore, since only one thermocouple in the spacer plate was used to measure the axial temperature, the temperature measurement was not stable. As the flow approached the fully filled region, a more stable flow was generated. Temperature decreased steadily in the region right before the fully filled region, because more heat was transferred from the hot barrel to the cold polymer pellets as more of the inner surface of the barrel was covered with cold polymer pellets. There was no electric heating for the spacer plate. The temperature of the spacer plate was maintained mainly through heat conduction from the barrels immediately upstream and downstream. Thus, the temperature of the spacer plate most probably will not be the same as the set temperature of the barrels attached to it. In Figure 2.9, we see that the inner wall

temperatures of the barrels even in the fully filled region were lower than their corresponding set temperatures.

There are two basic heat sources for polymer melting in the extrusion channel: one is heat transferred from the hot barrel either through conduction or convection, and the other is heat converted from mechanical power. Mechanical energy from the motor is usually the most important factor in a TSE. The mechanical energy is converted to heat through plastic energy dissipation (PED) of solid pellets (34), viscous energy dissipation (VED) of polymer melt (32, 47) and friction energy dissipation (FED) among solid polymer pellets (32, 34).

In the partially filled region for the PP/PS (80:20) blend, no PS melting is seen, and a few PP pellets are observed to melt on their surface (see Figure 2.8 at $X=90 \sim 130$ mm). The main heat transfer mechanism to melt polymer pellets in this region was heat conduction from the hot barrel. Friction between polymer pellets and air convection did not play a significant role in melting polymer pellets in the partially filled region under the conditions studied here. This will be discussed in more detail by comparing the melting behavior of PP/PS (80:20) blend and PS/PP (80:20) blend under the same operating conditions. For a polymer pellet to melt via conduction in the partially filled region, it must contact the hot barrel for a sufficiently long time so that enough heat can be transferred to the polymer pellet. For the PP/PS (80:20) blend, most polymer pellets contacting the hot barrel were PP, because 80% PP was added into the extruder. Pellets of PS and PP are similar in density and size, and therefore, both should be able to contact the barrel. Thus, due to the concentration difference, the probability for a PS pellet contacting the hot barrel in the partially filled region up to the beginning

of the fully filled region is much less than that for a PP pellet contacting the barrel. Some PP pellets were able to contact the hot barrel for sufficient time to melt first even though the T_f of PS is lower than that of PP. However, the total amount of melting in the partially filled region was not significant.

The channel was fully filled at $X=150\text{mm}$. It can be seen in Figure 2.8 that most PP pellets and PS pellets were still in the solid state and retained their original shape at $X=150\text{mm}$. Since so many PS pellets were seen and considering the small percentage of PS in the blend, it is reasonable to believe that most PS pellets were still in the solid state at the beginning of the fully filled region. PS pellets melted quickly in the first kneading block region (see Figure 2.8, $X=170\text{mm}$ to 210mm). Many partially melted PS pellets can be found at $X=170\text{mm}$, but much fewer solid or even partly deformed PS pellets can be observed at $X=190\text{mm}$; and at $X=210\text{mm}$, no PS pellets can be discerned. The major heat source for melting should come from mechanical energy through FED, PED or VED when the channel is fully filled (34, 47). The relative significance of the heat generated through FED, PED or VED depends on the concentration of the solid polymer pellets in the flow. In the very beginning of the fully filled region for the PP/PS (80:20) blend, FED and PED contributed most of the heat for the melting of polymer pellets since little polymer melt was present. We believe that PED could not be the dominant heat source compared to FED at the beginning of the fully filled region for the PP/PS (80:20) blend because no highly deformed solid PP or PS pellets can be found in our visualization (see Figure 2.8). Solid fraction in the flow was the key factor to determine the relative importance of FED, PED and VED for heat generation. In the transition region, FED and PED played key roles in achieving fast melting when the

solid fraction was greater than 80%. When there was more polymer melt in the flow, solid friction and solid plastic deformation were greatly reduced due to lubrication between solid particles. VED dominated the melting when the solid fraction was below 60%. As more polymer melted, much less energy was required to re-orient and deform the bulk plastic. Since molten polymer was being sheared between pellets, and between pellet and the barrel wall, the dominant heat source changed from combined FED/PED to VED.

The pressure results also describe the melting behavior. A significant amount of mechanical energy was applied to push the material forward at the beginning of the fully filled region. High pressure in this region (see Figure 2.9 at $X=150\text{mm}$ to 180mm) suggests that a large amount of mechanical energy was consumed. This generated a lot of heat and led to the quick melting of polymer pellets in this region. PS pellets softened and flowed first because the enthalpy change required to melt PS is lower than that of PP. Once the PS pellets melted at $X=180\text{mm}$, the pressure dropped sharply (see Figure 2.9). It was found that a large percentage of the PP pellets were still in the solid state after the PS pellets had fully melted and a molten PS phase had formed (see Figure 2.8, $X=210\text{mm}$). With over 20% polymer melt, FED and PED were no longer a major heat source for melting. VED dominated the melting of the majority of polymer pellets.

Figure 2.8 shows that a mixture of solid PP and PP/PS melt was present in the region from $X=210\text{mm}$ to $X=250$. The pressure increased again due to the backward flow generated by the RPE at the end of the kneading blocks (see Figure 2.9). The relatively constant pressure from position $X=230\text{mm}$ to 300mm occurs due to the combined effect of pressure decrease as the solid PP fraction in the flow decreased and

pressure increase due to the backward flow generated by the RPE. Because of the decrease in the solid polymer fraction, it is easier to push the material forward; thus less positive pressure difference is required. However, as the flow approaches the RPE, pressure is generated due to backflow. The melting process was not complete until the material passed the RPE. Figure 2.9 shows that the temperature increased continuously from the beginning of the fully filled region to the end of the RPE due to VED heating. This is consistent with the result provided by Curry (47).

Han et al. (19) introduced a concept called the ‘critical flow temperature’ (T_{cf}) for amorphous polymers. T_{cf} is around 50 °C higher than T_g . This concept was used to model the flow of amorphous polymers in a single-screw extruder (19) and in a twin-screw extruder (38). According to their definition, an amorphous polymer may be regarded as a ‘rubber-like’ solid when the temperature is below T_{cf} , and as a liquid when the temperature is above T_{cf} . Similarly, we postulate that there is a critical melt fraction (F_{cm}), below which the flow can be treated as that of a bulk plastic, and above which the flow can be treated as that of a concentrated suspension. The bulk plastic re-orientation and deformation essential to achieve good mixing in a twin-screw extruder requires energy. However, the energy required to deform an elastic bulk plastic is much higher than that required to deform a concentrated suspension. For melt fraction below F_{cm} , mechanical energy is converted to heat mainly through FED and PED, while for melt fraction above F_{cm} , mechanical energy is converted to heat mainly through VED. From our study, we find that F_{cm} is approximately 20%.

2.2.3.2 PS/PP (80:20) Blend

Figure 2.10 shows the flow visualization results for extrusion of the PS/PP (80:20) blend. Here, some PS pellets started softening and melting even in the conveying section (at $X=90\text{mm}$). The fully filled region started at the beginning of the first kneading block ($X=170\text{mm}$). There was a relatively high fraction of polymer melt at the beginning of the fully filled region. Figure 2.11 shows the axial temperature and pressure profiles for this process. The pressure did not vary significantly in the partially filled region. A pressure peak was also found in the PS/PP (80:20) blend at the beginning of the fully filled region (see Figure 2.11, $X=180\text{mm}$); however, the peak value ($P_{\max} = 3 \times 10^5\text{Pa}$) was much lower than the peak value ($P_{\max} = 20 \times 10^5\text{Pa}$) for the PP/PS (80:20) blend. The temperature showed a trend similar to that seen in the PP/PS (80:20) blend. There was oscillation in the temperature profile in the partially filled region and then a decrease in temperature was found just before the fully filled region. In the fully filled region, the temperature increased linearly with distance down the extruder.

In the partially filled region, under the same operating conditions, the probability that a PS pellet contacts the hot barrel in the PS/PP (80:20) blend is four times that expected for a PS pellet in the PP/PS (80:20) blend. Some of the PS pellets in the PS/PP (80:20) blend had a chance to contact the hot barrel for sufficient time to melt. For pellets in the partially filled channel, the amount of heat generated through friction between polymer pellets and air convection should be similar for the two blends (PS/PP=80:20 and PP/PS=80:20).

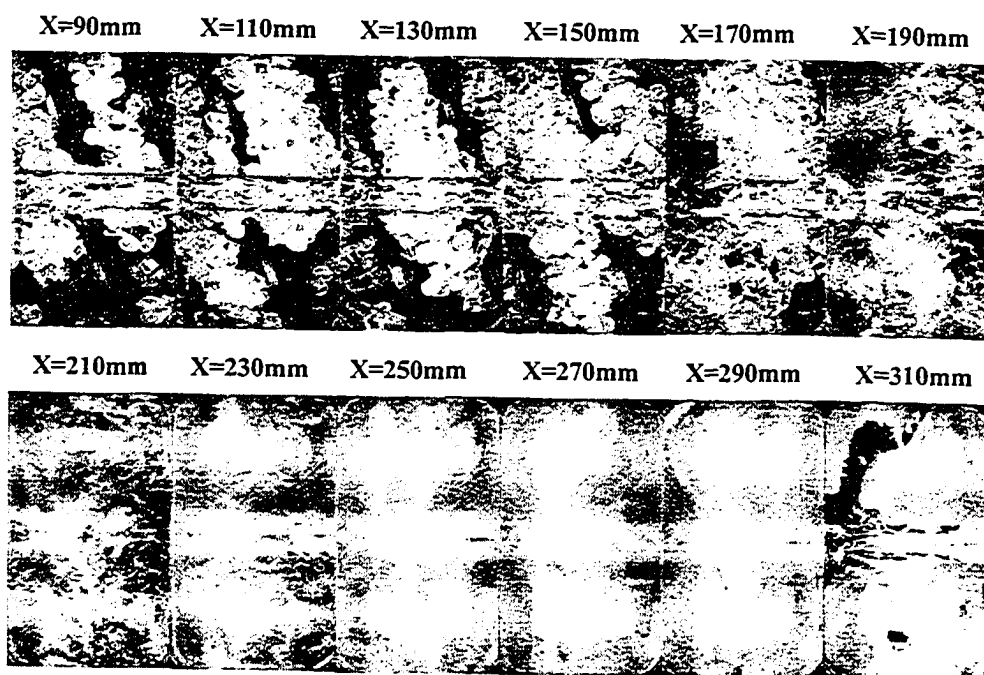


Figure 2.10 Visualization of PS/PP (80:20) blending process in the TSE. Each image begins at the value of X given and is 30mm in width. That is, for each image, there is a 10mm overlap on either side with the adjacent images.

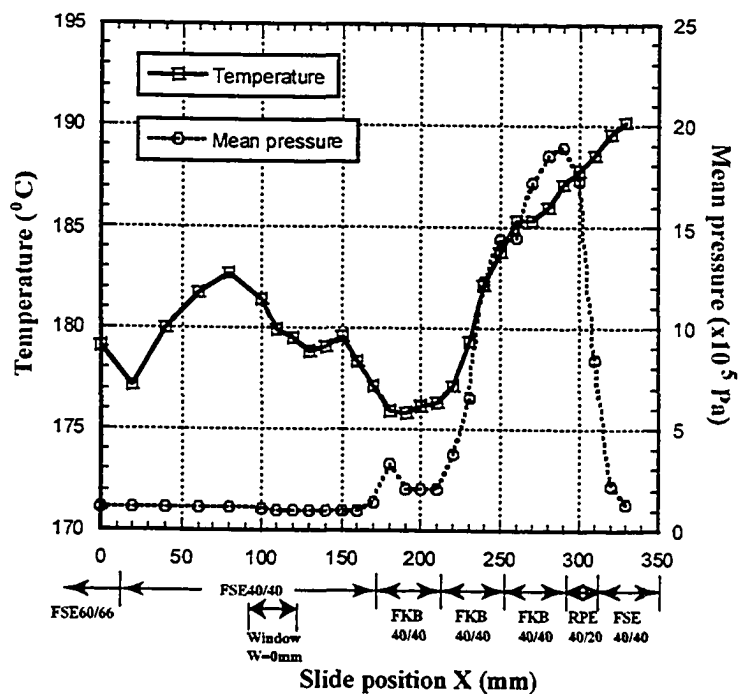


Figure 2.11 Axial temperature and pressure profiles for the extrusion of PS/PP (80:20) blend.

The concentration inversion of these two blends changed the contact time of PS pellets with the hot barrel, which resulted in melting of PS pellets in the partially filled region for PS/PP (80:20) blend. Therefore, the heat generated through friction between polymer pellets or heat transferred through air convection in the partially filled region is negligible compared with heat transferred via conduction from the hot barrel to the polymer for the operating conditions used here.

At the beginning of the fully filled region, we see that many PP pellets kept their original shape (Figure 2.10, $X=170\text{mm}$). Most PS pellets were either completely softened or partially softened. Significant FED and PED can only occur in the fully filled region if there is high solid fraction. In this case, since there was a relatively high concentration of polymer melt at the beginning of the fully filled region ($X=170\text{mm}$), little heat was generated through PED. In addition very few highly deformed solid pellets are seen in Figure 2.10, which is required for PED. The high melt fraction also suppressed any significant FED since there was melt between solid surfaces reducing frictional heat generation. Heat was generated mainly through VED at this stage and VED accelerated the melting rate of both the PS and PP pellets. It is believed the lower value of the initial pressure peak is due to the earlier initiation of lubrication flow for PS/PP (80:20) which forms a suspension of polymer pellets in melt. It is well known that in suspension flows, the stress decreases dramatically as the melt fraction (or fluid fraction) increases. Therefore, the lower value of the pressure peak is most likely due to the higher fraction of polymer melt present in the PS/PP (80:20) blend.

At $X=190\text{mm}$, very few solid pellets of either PS or PP were found in the flow, and almost all pellets had melted at $X=210\text{mm}$. The melting process for this blend was

complete in the middle of the third kneading block ($X=230\text{mm}$). Figure 2.11 shows that the sharp increase in pressure stops at an axial position of $X=250\text{mm}$ and there is a small plateau in the pressure curve. Since all the material has melted at this point, less pressure is generated until the effects of the RPE are felt. Therefore, for this case, the plateau is an indication of the end of the melting process. Since the RPE pushes the polymer melt backward, the highest pressure occurs right before the RPE. The pressure results indicate a low concentration of solid polymer pellets in the PS/PP (80:20) blend after $X=210\text{mm}$. This is consistent with the visualization results; i.e. very few solid polymer pellets are seen after the region of $X=210\text{mm}$ (Figure 2.10). The temperature profile for this blend is very similar to what was observed for the previous blend. Oscillation in temperature was observed in the partially filled region because cold pellets may occasionally contact the thermocouple at the barrel surface for certain slide positions. When the pellets started to melt just before the fully filled region, the temperature decreased as heat was transferred to the melt from the barrel. In the fully filled region, the temperature steadily increased due to viscous dissipation.

2.2.3.3 Comparison of PP/PS (80:20) and PS/PP (80:20) extrusions

Two polymer blends composed of the same materials at inverse concentrations show completely different melting mechanisms even under the same operating conditions. This is remarkable especially since the melting temperatures of the two components are similar, and yet we were able to see two very different melting sequences due to the blend concentration. For the PP/PS (80:20) blend, PP melted first due to the contact with the hot barrel, followed by complete melting of PS, and then continued melting of PP. For the PS/PP (80:20) blend, PS melted first, and followed by

combined melting of PS and PP. The sequences of melting along the extrusion channel for the two blends are summarized in Figure 2.12.

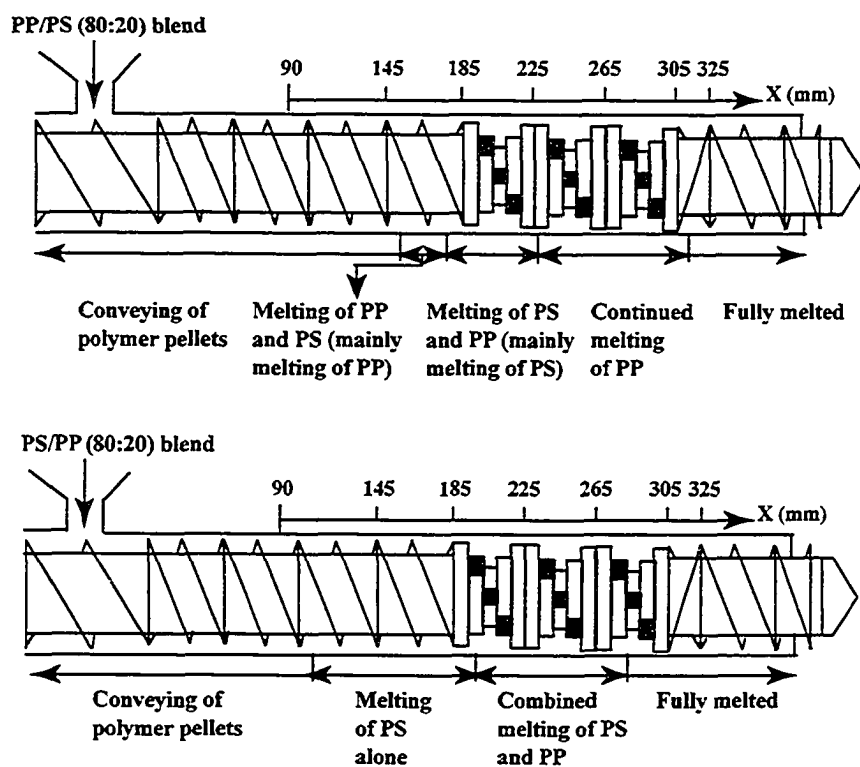


Figure 2.12 Melting sequences of PP/PS (80:20) blend and PS/PP (80:20) blend in the TSE.

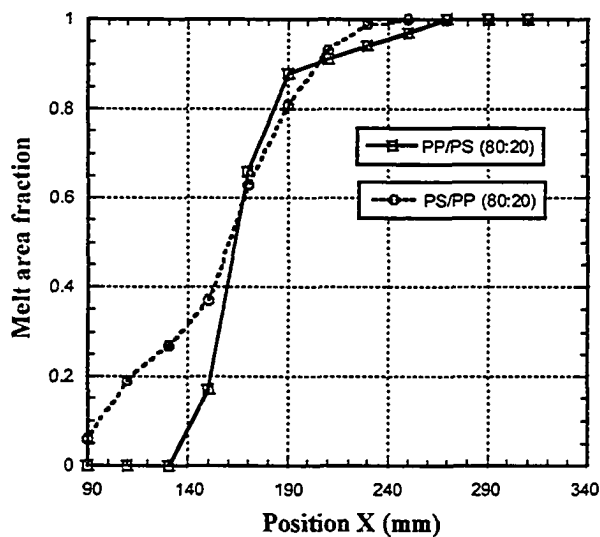


Figure 2.13 Melt area fraction along the extrusion channel for constant Q/N .

Based on the images obtained from the experiment, we calculated the melt area fraction at different positions along the extrusion channel. The melt fraction is plotted versus position for both blends in Figure 2.13. At the beginning of the fully filled region (between $X=130$ and $X=150$ mm), the PP/PS (80:20) blend comprised less than 20% melt while the PS/PP (80:20) blend had more than 40% melt. The melt area fraction increased very sharply in the fully filled region for both blends. Melt fraction at the beginning of the fully filled region had a large effect on the pressure profile, and on the relative contributions of FED, PED and VED to melting. The melting mechanisms for polymer pellets in a co-rotating TSE are summarized in Figure 2.14.

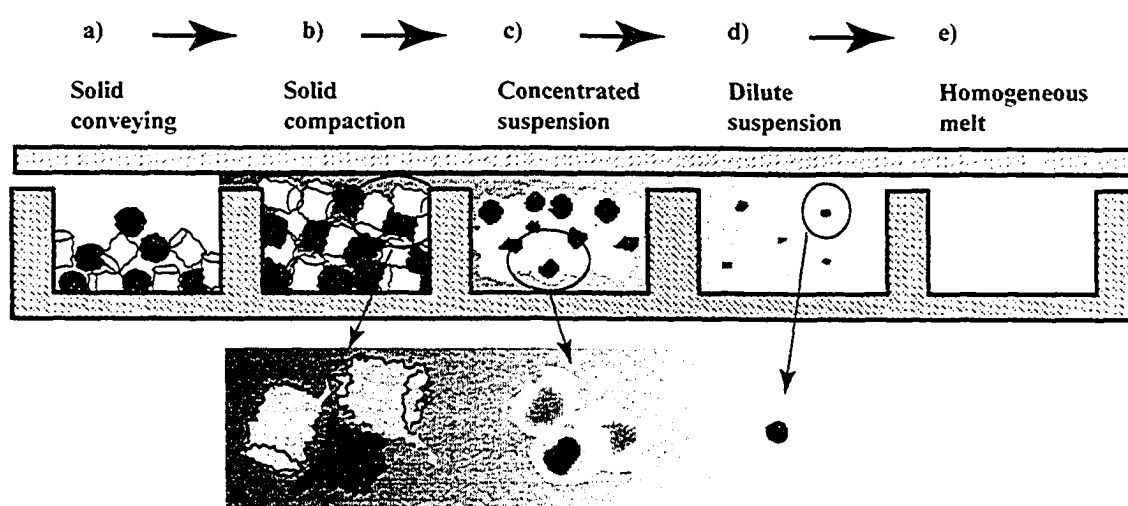


Figure 2.14 Melt mechanism of polymer pellets in a TSE. The majority of melting occurs in section b) and c). In each section, different heat sources dominate the melting: a) heat conduction and FED; b) FED & PED; c) PED & VED; d) VED & heat convection; e) melting finished.

In the conveying section a), the channel is usually partially filled. Heat conduction from the hot barrel and friction between polymer pellets and the screws are

the major heat sources to heat up polymer pellets. Most of the melting occurs in section b) and c). The complex flow generated by the two screws causes the solid polymer pellets to undergo high frequency reorientation and forward and backward movement under high pressure. Friction between solid polymer pellets and plastic deformation of polymer pellets (or FED and PED) generate a large amount of heat in section b) for the melting. The molten polymer on the surface is peeled off layer by layer mainly through friction between polymer pellets. The shape of polymer pellets becomes more like a sphere even for those pellets that originally have a cylindrical shape. With more molten polymer in the flow, a concentrated polymer melt suspension is usually formed in section c). Once the melting is initiated, the contribution of FED to the melting is greatly reduced due to lubrication by molten polymer. However, PED could still play an important role in the melting. Large deformation of softened polymer pellets is often found in section c). In a concentrated polymer melt suspension, VED plays a key role for the melting of polymers. The molten polymer on the surface of polymer pellets is peeled off either through contact with neighbor polymer pellets or by high shear stress generated in the gap between polymer pellets.

Since there is a majority of polymer melts in section b) and c), a dilute polymer melt suspension is formed in section d). The fluid temperature increases continuously mainly due to VED. Through heat convection, the melting of remaining solid polymer pellets is finished, and results in a uniform homogeneous polymer melt in section e). By changing TSE operating conditions, we can change the melt fraction at the beginning of the fully filled region, and thus modify the polymer melting behavior downstream.

2.3 PS/PP (80:20) blend at various Q/N

2.3.1 EXPERIMENTAL

The same extrusion setup as that in previous section was used for this study. The detailed description about the device used for the on-line visualization, and temperature and pressure measurement can be found in section 2.2.1 of this chapter. However, for this section, we used three pressure transducers and three flush-wall type-J thermocouples to obtain the pressure and temperature profiles. A RTD probe was also mounted in the spacer plate. The location of each probe in the spacer plate for this study is shown in Figure 2.15.

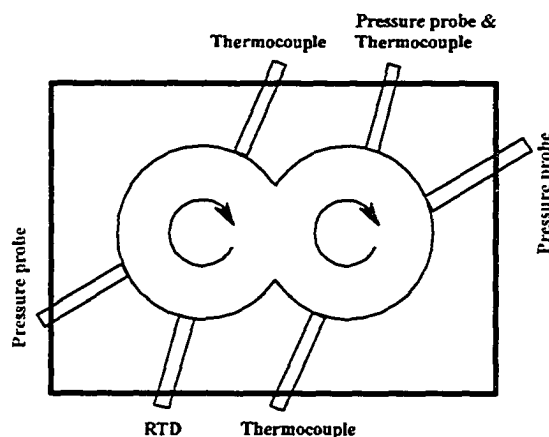


Figure 2.15 Probe locations in the spacer plate for extrusions with various Q/N.

Besides the on-line visualization, pressure and temperature measurement, the perturbation method was also used to characterize the melting behavior of PS/PP (80:20) blend in this section. The total pulse material was composed of five polyethylene (PE) pellets filled with carbon black (CB) (20% by weight) as the RTD tracer and 30g PS/PP blend (80:20, by weight) as the material mass pulse. For each run, the slide started at the

retracted position ($X=0\text{mm}$). The operation was allowed to stabilize for at least 2 minutes at each slide position before starting the video recording, performing the pressure and temperature measurement, and introducing the pulse material. After finishing measurements at one position, the barrel was moved to the next slide position, and the same procedures were used to acquire all dynamic data at the new position. The slide barrel was moved 5, 10 or 20mm each time toward the end of the screw depending on the channel location. After measurement, at each slide position, a set of data were obtained, including video, temperature, pressure, RTD data, and mass pulse signals. The melting process was visualized through the glass window at each slide location using digital video camera or high speed video recording device (2000 frames/second).

Table 2.3 Operation parameters for extrusion of PS/PP (80:20) blend with various Q/N.

	Q/N=5.0g/rev	Q/N=7.6g/rev	Q/N=11.3g/rev
Barrel temperature from 1 to 9 ($^{\circ}\text{C}$)	50-50-50-50-170-180-200-200-200		
Flow rate Q (kg/hr)	45.36	45.36	47.63
Screw speed N (rpm)	150	100	70
Q/N (g/rev)	5.0	7.6	11.3
Additional motor power input (kJ/kg)	212	231	254
$\Delta\hat{H}$ for PS/PP (80:20) blend from 50 to 200 $^{\circ}\text{C}$ (kJ/kg)			300

Polystyrene/polypropylene (PS/PP) blend (80:20) was used for all the extrusions studied here. Three runs were defined by their flow rate/screw rpm (Q/N) ratios, and all of them were operated in a starve-fed condition. For a total blend flow rate of approximately 45 kg/hr, the pulse material was composed of five PE pellets filled with

CB and 30g PS/PP blend. All three runs maintained the starve-fed condition when the 30g pulse material was added during steady state operations. The dynamic data scanned at 80Hz were decimated to 20Hz, which means three of every four data were deleted, and filtered with a 3-tap median filter to smooth the signals. At each slide location, two minutes of data were recorded. The first minute data were used to obtain the steady state baseline values. At the end of the first minute, the pulse material was added, and data was acquired for another minute to measure the machine response. The temperatures for barrels 1 to 9 were set as ($^{\circ}\text{C}$): 50-50-50-50-170-180-200-200-200 for all the three runs. The operating conditions for each run are summarized in Table 2.3.

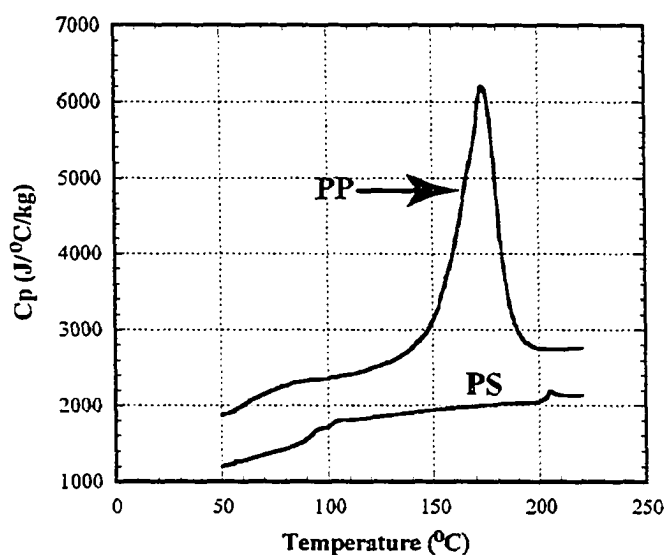


Figure 2.16 Heat capacity of PS and PP.

The two polymers used in this work were: PS (DOW Styron 666D), with glass transition temperature (T_g) 100°C , and PP (Atofina 3480Z), with melting temperature (T_m) 170°C . Figure 2.16 shows the specific heat (C_p) variation with temperature for the

two polymers. PP pellets are opaque and have a shape close to a sphere, while PS pellets are transparent and have a cylindrical shape (see Figure 2.6).

2.3.2 RESULTS AND DISCUSSION

2.3.2.1 On-line Pressure, Temperature and Visualization Measurements

There are three distinct regions in the TSE: the partially filled region, the transition region, and the fully filled region. Initially, the pellets are loosely packed and the extrusion channel is partially filled.

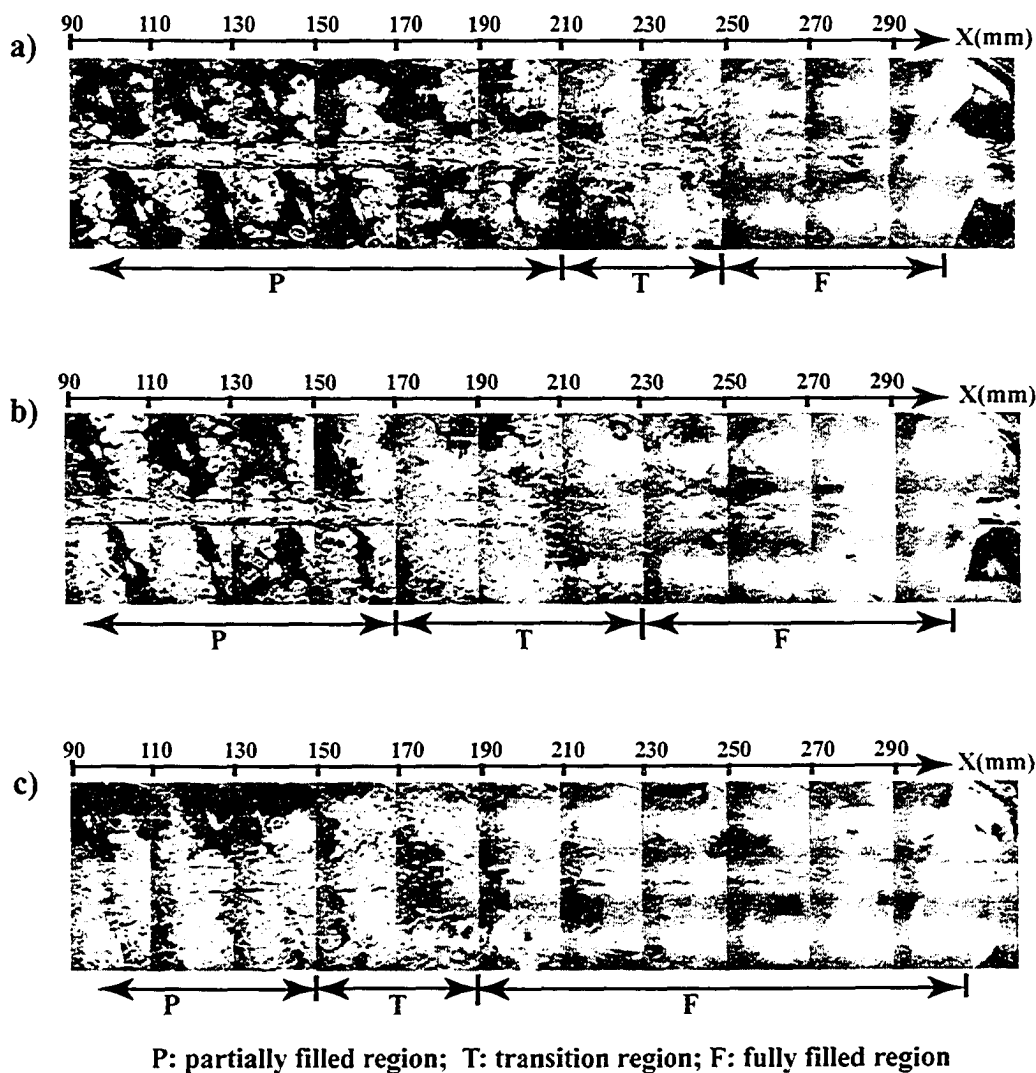


Figure 2.17 Visualization of PS/PP blend at different Q/N: a) Q/N=5.0g/rev; b) Q/N=7.6g/rev; c) Q/N=11.3g/rev.

The transition region begins when solid polymer pellets start compacting with each other in the channel. Some melt may also be present in the transition region. However, the major phase in the flow is the compacted solid pellets. Due to the air space between solid pellets, the channel in the transition region is still only partially filled. As more molten polymer is generated and distributed in the flow, a polymer melt suspension with un-melted polymer pellets is formed. When the polymer melt forms the major phase, the channel is fully filled. This indicates the end of the transition region and the beginning of the fully filled region. Figure 2.17 shows the flow visualization results, including separation into the three different regions, for all the three runs, and Figure 2.18 and Figure 2.19 show their pressure and temperature profiles.

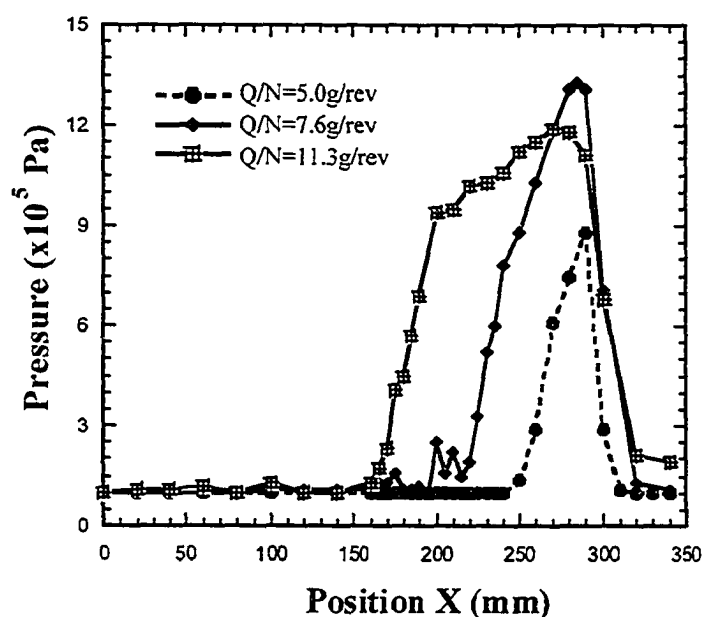


Figure 2.18 Axial pressure profiles for the three runs with various Q/N .

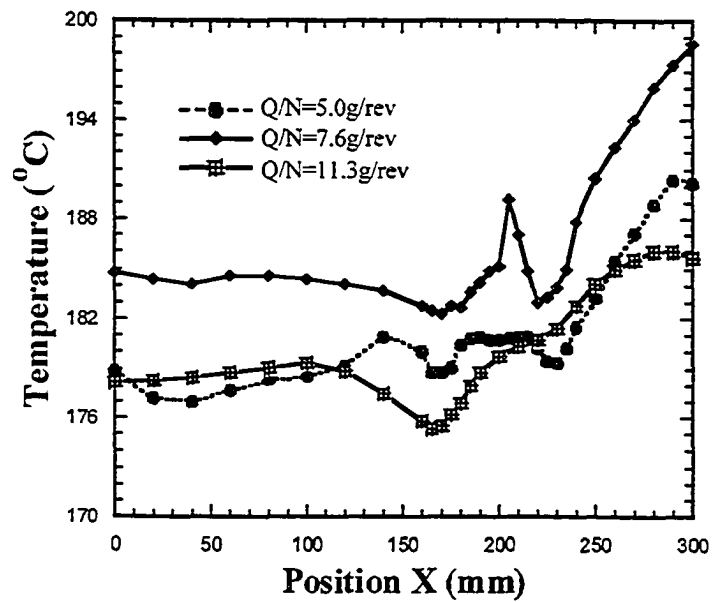


Figure 2.19 Axial temperature profiles for the three runs with various Q/N .

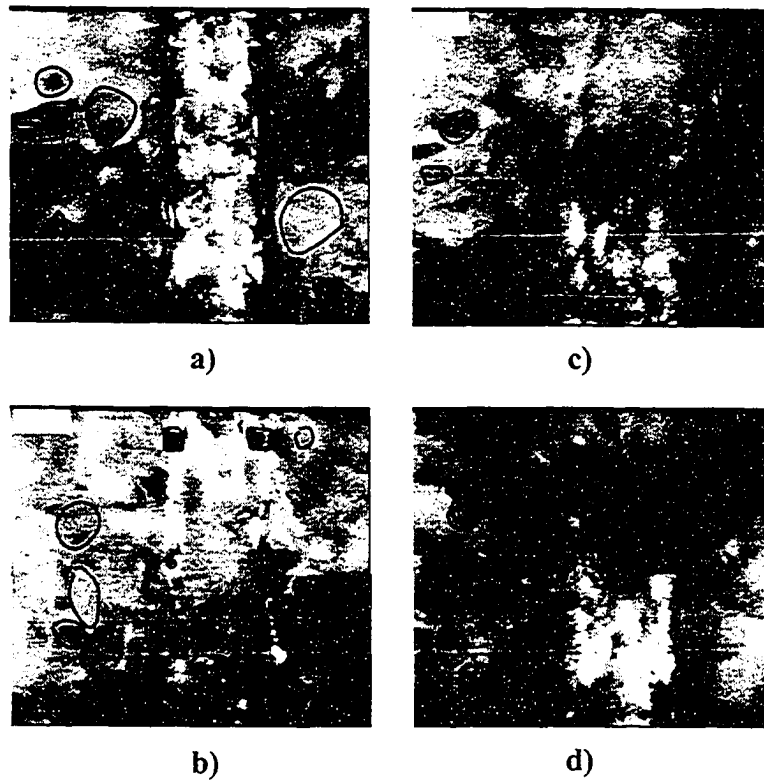


Figure 2.20 High speed video images for $Q/N=7.6g/rev$ at locations: a) $X=150mm$; b) $X=170mm$; c) $X=190mm$; d) $X=210mm$.

The final location of each region for each run (in Figure 2.17) was determined based on the visualization results, temperature and pressure profiles, and the pulse signals. Different methods may indicate a slightly different location for the same region in each run. A high speed video recorder was used to visualize the melting process due to the high rotation speed of the screws. Figure 2.20 shows some high speed video images for run 2 with $Q/N=7.6\text{g/rev}$ in the transition region. Outlines of some un-melted pellets are highlighted.

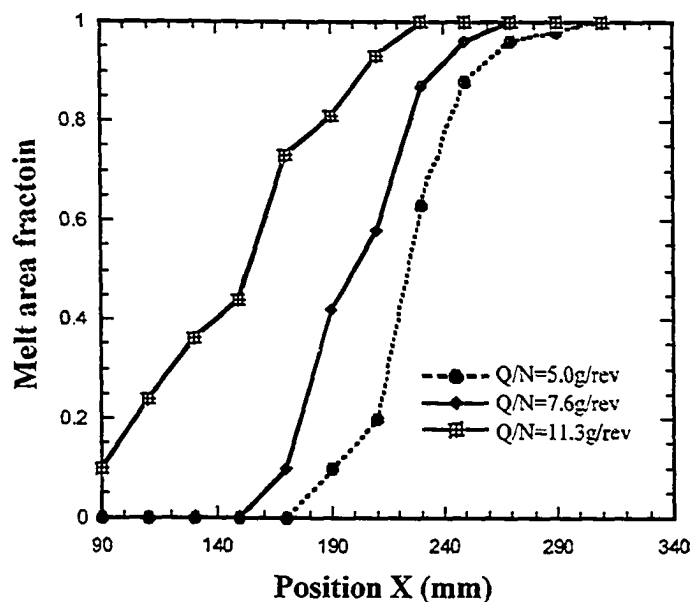


Figure 2.21 Melt area fraction along the extrusion channel for the three runs with various Q/N .

Based on the images obtained from the experiment, we calculated the melt area fraction at different positions along the extrusion channel. The melt fraction is plotted versus position for all runs in Figure 2.21. Combining the on-line visualization of the processes, temperature and pressure measurement along the extrusion channel, RTD

data, and the mass pulse data, we obtained a comprehensive picture of the melting process. The melting in each region was distinct; therefore, we have divided our observations and discussion on melting into the three different regions: partially filled region, transition region, and fully filled region.

2.3.2.1.1 Partially Filled Region

The end of the partially filled region can be determined using the on-line visualization results (Figure 2.17). For run 1 ($Q/N=5.0\text{g/rev}$), the partially filled region ended at position $X=200\text{mm}$. As the ratio of Q/N increased, the end of the partially filled region moved upstream: for run 2 with $Q/N=7.6\text{g/rev}$, it ended at $X=160\text{mm}$, and for run 3 with $Q/N=11.3\text{g/rev}$, it ended at $X=150\text{mm}$. In the partially filled region, the pressure was constant and equal to one atmosphere pressure (see Figure 2.18), and the temperature was also relatively constant (see Figure 2.19).

The temperature and pressure profiles along the extrusion channel also help us to understand melting phenomena inside the extrusion channel. The trends of the temperature and pressure profiles in the partially filled region are similar at different Q/N ratios. Since flush-wall type thermocouples were used to obtain the temperature profiles, the measured temperature was the temperature of the inner surface of the barrel, or of material directly contacting the inner barrel surface. At the end of the partially filled region, a decrease followed by an increase in temperature was usually seen (30, 48). This trend can be found in the temperature profiles for all three runs (see Figure 2.19). The temperature profile of run 2 with $Q/N=7.6\text{g/rev}$ is around 5°C higher than those of the other two runs. This could be caused by differences in temperature of the feed into the extruder.

In the previous section, we reported that for the PS/PP (80:20) blend, PS melted first in the conveying zone followed by a combined melting of PS and PP in the kneading zone. The same melting sequence was observed for all the runs studied here. In the partially filled region, the pressure was low and a small amount of PS melted. Most polymer pellets were pushed forward in a manner similar to plug flow. Figure 2.21 gives an indication of what percent of polymer melted in the partially filled region. There was around 10% polymer melted in the partially filled region for run 1 (at $X=200\text{mm}$), only 5% for run 2 (at $X=160\text{mm}$), and 40% for run 3 (at $X=150\text{mm}$). However, these values should not be used as the real melt fractions in the flow considering the fact that most polymer melt was located close to the barrel and most solid pellets were probably close to the screws during melting in TSE (13, 20, 22). The melt fractions obtained based on the on-line visualization images (Figure 2.21) should be higher than the real values in the flow, especially in the partially filled region. Mechanical energy through plastic energy dissipation (PED) or viscous energy dissipation (VED) (11, 34) did not contribute significantly to the melting of polymer pellets. The melting was initiated by conduction from the hot barrel in the partially filled region under the conditions studied here. The pulse data confirmed that dissipation of mechanical energy was insignificant in the partially filled region, and therefore, heat from the barrel was the most important contributor to melting observed in the partially filled region. The pulse data will be discussed in detail later.

In the partially filled region, the melting mechanisms at different Q/N ratios were similar. The surface of some PS pellets softened first mainly due to heat conduction from the hot barrel and friction between the pellets and the rotating screws.

Then the softened layer underwent deformation due to the relative movement of the screw and the barrel, and some deformation was big enough to cause layers to peel off from the PS pellets. It is a mechanism similar to “erosion” reported in experiment (49) and simulations (50) of initial deformation in polymer blends. However, the erosion that occurred here in the partially filled region was caused mainly through the relative movement of the pellets against the barrel, while erosion found in previous work (49, 50) was caused by the shearing in melt flow. For run 3 only ($Q/N=11.3$), after some PS pellets melted, all the pellets agglomerated, and some PP pellets melted in the partially filled region in a manner similar to that found for PS pellets. We did not observe any large deformation of pellets for either PS or PP before they softened. Thus, PED did not play an important role for the melting of PS/PP blend in the partially filled region. Some large deformation reported for polymer pellets during melting in other studies (11, 20) could have been caused by the sampling method. For example, if the sample was obtained by shutting down the machine during steady state operation, and subsequently the melt was solidified, the large deformation found could be the deformed molten layer that was peeled off from its mother pellet. There is no way to state if the pellet was stretched in the solid state using quenched samples. The thermal history at different layers in a polymer pellet cannot be identified through morphology observation after the entire pellet was cooled down. There is a need to perform on-line visualization of deformation, as we have done in this study, or to find the temperature profile within a pellet during melting.

2.3.2.1.2 Transition Region

Although some pellets melted in the partially filled region, the amount of melting in this region was not significant. Most of the melting took place in the transition from the partially filled region to the fully filled region (see Figures 2.17 and 2.21). Therefore, the transition region is the most important region for studying melting in a TSE.

Visualization of the extrusion process provided us a direct method to study the details of polymer melting behavior in extruders (21, 29, 30). It can be seen from Figure 2.17 that the run with $Q/N=7.6\text{g/rev}$ had the longest transition region and it also showed the most peculiar behavior in terms of temperature and pressure profile. From the high speed video results shown in Figure 2.20, it was found that the solid polymer pellets melted in the transition region through an “erosion” mechanism similar to what was found in the partially filled region. However, the peeling off of the softened layer in the transition region was caused mainly through contact with other pellets (20). The same “erosion” mechanism was also found using high speed video for $Q/N=5.0\text{g/rev}$ and $Q/N=11.3\text{g/rev}$ in the transition region.

There is some difference between the three runs in their pressure profiles: specifically, there are two distinct regimes (i.e. slopes) of pressure increase in the pressure profiles for $Q/N=7.6\text{g/rev}$ and $Q/N=11.3\text{g/rev}$, while there seems to be one sustained regime of pressure increase with a constant slope for $Q/N=5.0\text{g/rev}$ (see Figure 2.18). Since the transition region for all the three runs ended in the kneading blocks, the screw geometry is not the reason for the difference. Rather, the difference was mainly caused by the solid concentration in the flow. For $Q/N=5.0\text{g/rev}$, at the end

of the transition region, very few solid polymer pellets can be found (see Figure 2.17a, $X=250\text{mm}$). The melting process was almost finished at the beginning of the fully filled region. For $Q/N=7.6\text{g/rev}$ and $Q/N=11.3\text{g/rev}$, some solid polymer pellets can still be identified at the end of the transition region ($Q/N=7.6\text{g/rev}$: $X=230\text{mm}$; $Q/N=11.3\text{g/rev}$: $X=190\text{mm}$). Therefore, in these cases, a sharper pressure gradient was required initially to push polymer melt suspension forward than that required after complete melting to push pure polymer melt under the same flow conditions. Using the visualization results, we confirmed that the transition from the higher slope to the lower slope in the pressure profiles for $Q/N=7.6\text{g/rev}$ and $Q/N=11.3\text{g/rev}$ occurred at the end of the transition region in the extrusion channel. Using the pressure profile in Figure 2.18, for $Q/N=7.6\text{g/rev}$, it can be determined that the melting process ended at $X=240\text{mm}$, and for $Q/N=11.3\text{g/rev}$ at $X=200\text{mm}$, and these results from the pressure match the visualization results (see Figure 2.17a and 2.17b).

The temperature and pressure profiles along the extrusion channel in the transition region were similar. Figure 2.19 shows an abnormal temperature peak for $Q/N=7.6\text{g/rev}$ in the transition region (at $X=200\text{mm}$). All three thermocouples at different angular locations in the spacer plate detected this temperature increase. From the visualization results, it can be clearly seen that the bulk flow at the beginning of the transition region included a high concentration of solid polymer pellets (see Figure 2.17b, at $X=170$ and 190mm). This temperature increase could be caused by friction between solid pellets and the barrel (i. e. the thermocouple probe tips). The friction between solid pellets and the probes would also explain the oscillation of pressure signals in the transition region for $Q/N=7.6\text{g/rev}$ (see Figure 2.18 at $X=200\sim 220\text{mm}$).

For $Q/N=5.0\text{g/rev}$ and $Q/N=11.3\text{g/rev}$, the friction between solid pellets and the probes was much lower due to a polymer melt film that formed as the flow reached to the transition region (see Figure 2.17a and 2.17c). However, the inter-pellet friction and friction between the screw and solid polymer pellets was still significant. Most of the polymer melt was located between the barrel and the solid bed when the flow reached the transition region. Considering the high concentration of solid polymer pellets in the transition region, we believe that friction energy dissipation (FED) generated a significant amount of heat to melt the PS/PP blend, especially at the beginning of the transition region.

As more polymer pellets melted through friction in the beginning of the transition region, a concentrated polymer melt suspension with solid polymer pellets was formed. FED did not play an important role for the melting of remaining solid pellets since they were lubricated by polymer melt. The viscosity of such suspensions can be over twenty times larger than the viscosity of the pure polymer melt under the same flow conditions (20). The VED from shearing this suspension provided another way to convert mechanical energy into heat to melt solid polymer pellets in the transition region. The polymer blend melted quickly in the transition region due to the mechanical energy input from the motor and screws. When the flow passed the transition region, over 80% of polymer material was melted for all three runs (see Figure 2.21 at $X=250\text{mm}$ for $Q/N=5.0\text{g/rev}$, at $X=230\text{mm}$ for $Q/N=7.6\text{g/rev}$, and at $X=190\text{mm}$ for $Q/N=11.3\text{g/rev}$).

Using visualization and temperature results, we determined that the end of the transition region occurred at the point just after the characteristic dip in temperature

seen in all three runs. At the end of the transition region, the polymer melt fully filled the channel and the temperature steadily increased.

2.3.2.1.3 Fully Filled Region

The majority of solid polymer pellets melted in the transition region. When the flow reached the fully filled region, a dilute polymer melt suspension with the remaining solid polymer pellets was formed (see Figure 2.17). Heat convection in the flow around the un-melted polymer pellets became comparable to the VED as a potential source for the melting of the remaining solid polymers in the fully filled region. The remaining solid polymer disappeared through the same erosion mechanism as that reported by Lin et al. (49), and shearing in the flow caused the peeling off of the outer layer from the pellets.

The pressure increased at a constant slope in the fully filled region. At the end of the fully filled region, after the RPE, the pressure decreased abruptly to atmospheric levels. The temperature in all three runs showed a similar trend and increased continuously in the fully filled region ($X=300\text{mm}$) due to VED and heat transferred from the hot barrel.

2.3.2.2 RTD and Pulse Measurements

For each slide position, concentrated carbon black filled PE pellet tracers were added to the feed with the pulse material to obtain the RTD. After the tracer pellets were melted, the CB distributed in the flow, and a light signal proportional to the CB concentration was obtained from the RTD probe. The light intensity data can be converted to true concentration to obtain the RTD curve (43). By measuring the RTD at each slide position, we were able to determine the time required for the pulse material to

reach different parts of the screw. The mass pulse material (added to the feed at the same time as the tracer) caused a peak in the motor amperage at the time the majority of pulse material melted in the extruder, i.e. a significant additional amount of mechanical energy was consumed to melt the extra pulse material added.

Since the motor voltage was 110V for all three runs, the relative motor power input can be represented by the current passed to the motor. Figure 2.22 shows the relative positions of the current peak due to melting of pulse material and the RTD peak at different slide positions for all three runs.

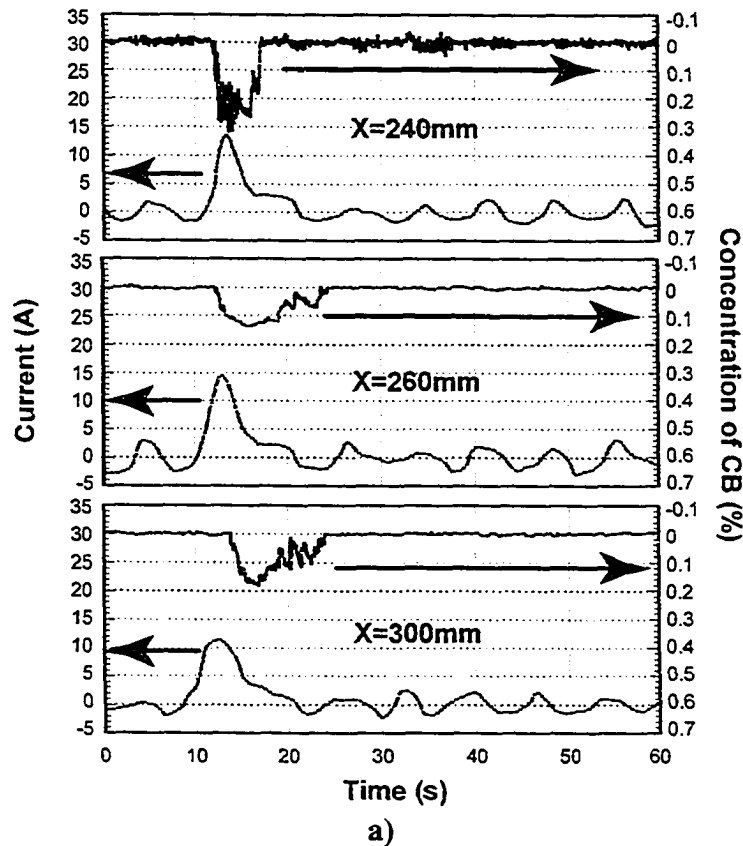


Figure 2.22 Relative positions of the melting peak and the RTD peak: a) $Q/N=5.0\text{g/rev}$; b) $Q/N=7.6\text{g/rev}$; c) $Q/N=11.3\text{g/rev}$. It can be seen that motor power peak and RTD peak coincide at a) $X=240\text{mm}$, b) $X=190\text{mm}$, c) $X=180\text{mm}$. These locations correspond approximately to the midpoint of the transition region in Figure 2.17. The transition region is where most of the melting was observed.

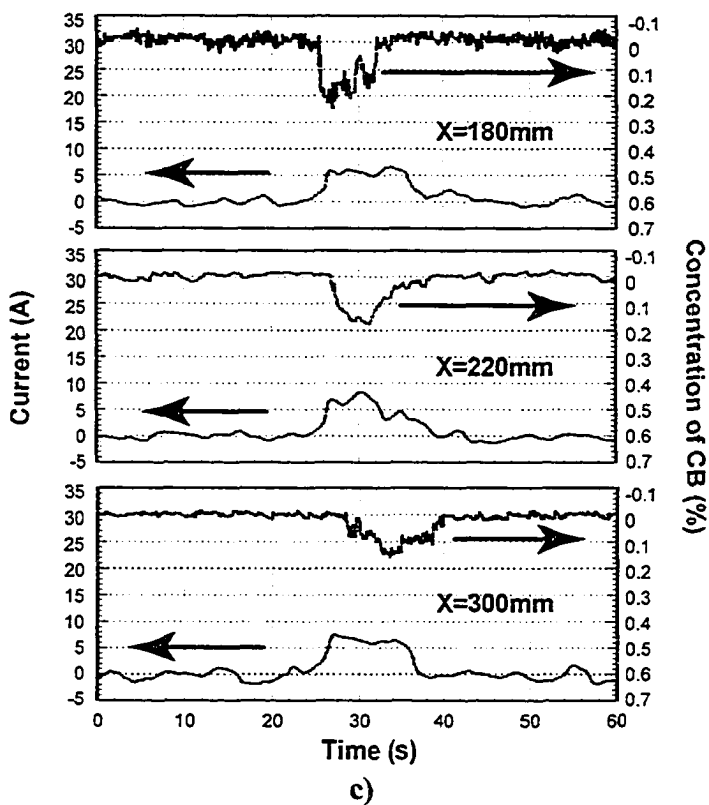
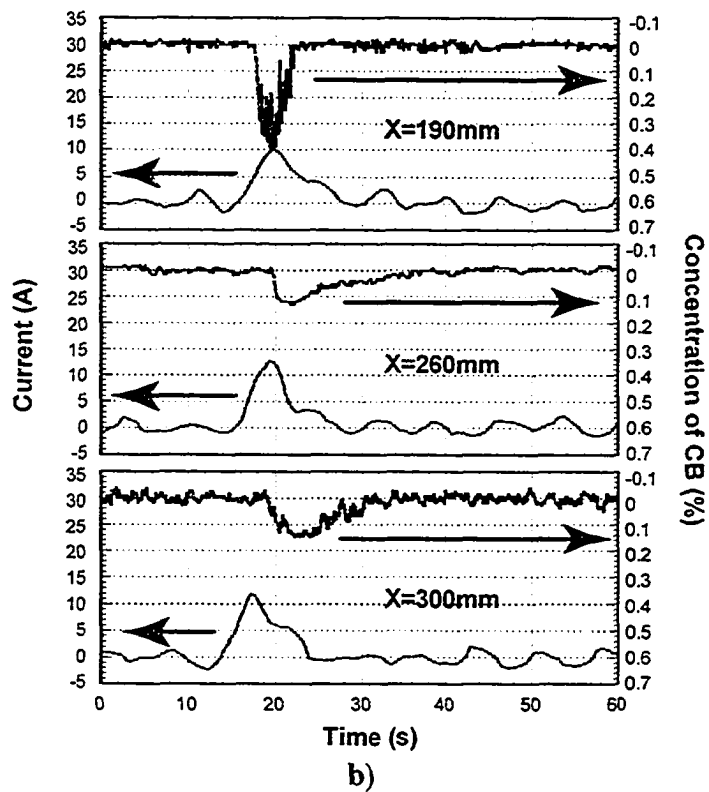


Figure 2.22 (Continued).

The current peak corresponds to the time that a significant mechanical energy was consumed to melt the pulse mass. Essentially, the time of the current peak indicates how long it took for the pulse mass to reach the location where the majority of pulse material melted in the extruder. Meanwhile, the RTD peak corresponding to a particular slide location indicates how long it took the pulse material to reach that slide location of the extruder. At each slide position, we have RTD data and mass pulse data (motor current signal). The motor current peak occurs at the same time for all slide positions. The RTD peak changes since it depends on the position of the RTD sensor (i.e. the spacer plate). For each run, the slide position where the two peaks coincide is where a significant mechanical energy was consumed for the melting.

Taking run 1 ($Q/N=5.0\text{g/rev}$) as an example, the melting peaks (bottom curves in all three plots) at different slide positions had a similar shape and appeared at almost the same time (see Figure 2.22a). As the slide moved further downstream, the RTD peak shifted to a longer time because the RTD probe moved downstream and the RTD changed due to back flow generated in the kneading blocks and reverse pumping element. At slide position $X=240\text{mm}$, the RTD peak and current peak appeared at the same time, indicating that a significant amount of mechanical energy was consumed to melt the pulse material in the region around $X=240\text{mm}$. From the visualization results, we found that $X=240\text{mm}$ corresponded to the center of the transition region for run 1 with $Q/N=5.0\text{g/rev}$, and much of the melting occurred in the transition region (see Figure 2.17a). Considering the size of the extruder and the flow rates used in this study, we assume that the 30g pulse material did not significantly change the steady state flow; thus what happened to the pulse material in the channel closely represents what

happened to the flow under steady state operation. Therefore, a significant amount of mechanical energy was consumed in the transition region to melt the PS/PP blend when $Q/N=5.0\text{g/rev}$. The same result that the motor current peak occurred at the center of the transition region was also obtained for $Q/N=7.6\text{g/rev}$ and $Q/N=11.3\text{g/rev}$.

The amount of mechanical energy consumed for melting the pulse material in the transition region can be obtained through integration of the motor power input with time. However, the energies for the three runs can only be compared qualitatively with each other because the motor efficiency may be slightly different under different conditions. The same amount of pulse material (30g PS/PP (80:20) blend) was added to the feed for each run. Each run had a different mechanical energy value; the energy value corresponded to the amount of solid polymer pellets melted in the transition region. For each run, integration was performed on at least three melting peaks to obtain an average value of the amount of mechanical energy consumed (additional motor power input) in the transition region. The final results for all three runs are given in Table 2.3. As Q/N increased, more mechanical energy was consumed to melt polymers in the TSE under the conditions studied here. Using C_p data (Figure 2.16), we calculated the enthalpy change of PS/PP (80:20) blend from 50°C to 200°C . It is shown that the total energy required to melt the PS/PP (80:20) blend from 50°C to 200°C is 300kJ/kg (Table 2.3). Table 2.3 shows that the mechanical energy consumed in the transition region for all three runs contributed significantly to the melting of PS/PP (80:20) blend in the TSE under the conditions studied here. It should be noted that the motor power efficiency may change slightly with different operating conditions. More experiments

are needed to find the motor power efficiency to obtain the absolute amount of mechanical energy for the melting of the pulse material.

2.3.2.3 Determination of Transition Region Location

The location of the transition region can be determined using the on-line visualization results, pressure and temperature profiles, and the pulse signals. There are several possible heat sources for the melting in each region. The contribution of each heat source to the melting is dependent on flow material properties, operating conditions, and screw configuration. As the Q/N ratio changed, the contribution of each heat source to melting in each region also changed. Therefore, no direct relationship can be built between the Q/N ratio and the length of each region. Table 2.4 summarizes the extrusion channel positions for the transition region obtained from the visualization results, pressure profiles, temperature profiles, and the pulse signals.

Table 2.4 Determination of locations of the transition region for various Q/N*.

	The transition region								
	Q/N=5.0g/rev			Q/N=7.6g/rev			Q/N=11.3g/rev		
	Begin	Center	End	Begin	Center	End	Begin	Center	End
Visualization	200	230	250	160	200	230	150	170	190
Press. profile	—	240	—	—	190	240	—	160	200
Temp. profile	—	—	240	—	—	230	—	—	190
Pulse signals	—	240	—	—	190	—	—	180	—
Typical range	210~250			170~230			150~190		

* The locations are correspondent to X in the unit of mm.

— No data available.

It is seen that the locations obtained using the four different techniques match quite closely. The location of each region by visualization for all three runs is presented in Figure 2.17. Visualization is the clearest method to determine melting location since we can actually see if the material is melted or not. However, in a real operation, it may be difficult and impractical to visualize the extrusion process. However, from this work, we see that the pressure and temperature can give us an indication of the location where melting occurs and we can get a definitive location by combining mass pulse data with RTD data. This can be a very powerful tool to understand extrusion processing and will help in extrusion process design.

2.4 Summary

A sliding barrel mechanism and a perturbation method were used to perform on-line visualization of polymer blend extrusion, obtain the axial temperature and pressure along the extruder, and detect the location of mechanical energy consumption in the TSE.

Three distinct regions were found for the melting of the PS/PP blend in the TSE: the partially filled region, the transition region, and the fully filled region. The transition region defined here bridged the area between compaction of solid polymer pellets in the channel to full filling of the channel with polymer melt. The location of the transition region can be determined from the visualization results, temperature and pressure profiles, and the pulse signals.

Melting in the partially filled region was caused mainly through heat conduction with the barrel for the system studied here. Most of the melting occurred in the transition region due to heat generation through FED, PED, and VED from mechanical energy. Solid fraction in the beginning of the transition region was the key factor to determine the relative importance of FED, PED and VED for heat generation. In the transition region, FED and PED played key roles in achieving fast melting of PS/PP blends when the solid fraction was larger than 80%, while VED dominated the melting when the solid fraction was below 60%. Melting in the fully filled region was mainly through VED and heat convection.

The composition of a polymer blend has a big effect on its melting behavior in TSE. Completely different melting sequences were found for PS/PP (80:20) and PP/PS (80:20) blends even under the same operating conditions. For PS/PP (80:20) blend, the

melting was initiated with PS in the partially filled region, and followed by a combined melting of PS and PP in the transition region; while for PP/PS (80:20) blend, the melting was initiated with PP in the transition region, then dominant melting of PS, and finally melting of PP alone in the transition region. As the ratio of Q/N increased, the beginning of the transition region moved upstream.

Solid polymer pellets melted in the TSE through an erosion mechanism in all three regions. In the partially filled region, the peeling off of the outer layer from polymer pellets was caused by the relative movement of pellets against the barrel, while in the transition region, it was caused by contact with neighboring pellets, and in the fully filled region, it occurred through shearing of pellets in the melt flow. The end of the melting process can be identified using the visualization results and, to some extent, the pressure profile along the extrusion length. Combining the barrel sliding technique and the perturbation method was an effective way to analyze fundamentals of melting in a TSE.

2.5 References

1. Wu, S., "Phase-Structure and Adhesion in Polymer Blends - A Criterion for Rubber Toughening," *Polymer*, **26**, 1855 (1985).
2. Subramanian, P. M., "Permeability Barriers by Controlled Morphology of Polymer Blends," *Polym. Eng. Sci.*, **25**, 483 (1985).
3. Montiel, A. G., H. Keskkula, D. R. Paul, "Impact-Modified Nylon-6 Polypropylene Blends. 1. Morphology - Property Relationships," *Polymer*, **36**, 4587 (1995).
4. Bucknall, C. B., F. P. Cote, I. K. Partridge, "Rubber Toughening of Plastics. 9. Effects of Rubber Particle-Volume Fraction on Deformation and Fracture in HIPE," *J. Mater. Sci.*, **21**, 301 (1986).
5. Scott, C. E., C. W. Macosko, "Model Experiments Concerning Morphology Development during the Initial-Stages of Polymer Blending," *Polym. Bull.*, **26**, 341 (1991).
6. Sundararaj, U., C. W. Macosko, R. J. Rolando, H. T. Chan, "Morphology Development in Polymer Blends," *Polym. Eng. Sci.*, **32**, 1814 (1992).
7. Shi, Z. H., L. A. Utracki, "Development of Polymer Blend Morphology during Compounding in a Twin-Screw Extruder. 2. Theoretical Derivations," *Polym. Eng. Sci.*, **32**, 1834 (1992).
8. Sundararaj, U., C. W. Macosko, "Drop Breakup and Coalescence in Polymer Blends," *Macromolecules*, **28**, 2647 (1995).
9. Huneault, M. A., Z. H. Shi, L. A. Utracki, "Development of Polymer Blend Morphology during Compounding in a Twin-Screw Extruder. 4. A New Computational Model with Coalescence," *Polym. Eng. Sci.*, **35**, 115 (1995).
10. Delamare, L., B. Vergnes, "Computation of the Morphological Changes of a Polymer Blend Along a Twin-Screw Extruder," *Polym. Eng. Sci.*, **36**, 1685 (1996).
11. Gogos, C. G., Z. Tadmor, M. H. Kim, "Melting Phenomena and Mechanisms in Polymer Processing Equipment," *Adv. Polym. Tech.*, **17**, 285 (1998).
12. Potente, H., M. Bastian, K. Bergemann, M. Senge, G. Scheel, T. Winkelmann, "Morphology of Polymer Blends in the Melting Section of Co-Rotating Twin Screw Extruders," *Polym. Eng. Sci.*, **41**, 222 (2001).

13. Tadmor, Z., "Fundamentals of plasticating Extrusion," *Polym. Eng. Sci.*, **7**, 185 (1966).
14. Tadmor, Z., I. J. Duvdevani, I. Klein, "Melting in Plasticating Extruders Theory and Experiments," *Polym. Eng. Sci.*, **7**, 198 (1967).
15. Lee, K. Y., C. D. Han, "Analysis of the Performance of Plasticating Single-Screw Extruders With a New Concept of Solid-Bed Deformation," *Polym. Eng. Sci.*, **30**, 665 (1990).
16. Lai, E., D. Yu, "Modeling of the Plasticating Process in a Single-Screw Extruder: A Fast-Track Approach," *Polym. Eng. Sci.*, **40**, 1074 (2000).
17. Elbirli, B., J. T. Lindt, S. R. Gottgetreu, S. M. Baba, "Mathematical Modeling of Melting of Polymers in a Single-Screw Extruders," *Polym. Eng. Sci.*, **24**, 988 (1984).
18. Lindt, J. T., B. Elbirli, "Effect of the Cross-Channel Flow on the Melting Performance of a Single-Screw Extruder," *Polym. Eng. Sci.*, **25**, 412 (1985).
19. Han, C. D., K. Y. Lee, N. C. Wheeler, "Plasticating Single-Screw Extrusion of Amorphous Polymer: Development of a Mathematical Model and Comparison With Experiment," *Polym. Eng. Sci.*, **36**, 1360 (1996).
20. Todd, D. B., "Melting of Plastics in Kneading Blocks," *Intern. Polym. Process.*, **8**, 113 (1993).
21. Sakai, T., "The Development of On-Line Techniques and Novel Processing Systems for the Monitoring and Handling of the Evolution of Microstructure in Nonreactive and Reactive Polymer Systems," *Adv. Polym. Tech.*, **14**, 277 (1995).
22. Bawiskar, S., J. L. White, "Solids Conveying and Melting in a Starved Fed Self-Wiping Co-Rotating Twin Screw Extruder," *Intern. Polym. Process.*, **10**, 105 (1995).
23. Cho, J. W., J. L. White, "Melting and Blending in a Modular Co-Rotating/Counter-Rotating Twin Screw Extruder," *Intern. Polym. Process.*, **11**, 21 (1996).
24. Bawiskar, S., J. L. White, "A Composite Model for Solid Conveying. Melting. Pressure and Fill Factor Profiles in Modular Co-Rotating Twin Screw Extruders." *Intern. Polym. Process.*, **12**, 331 (1997).
25. Bawiskar, S., J. L. White, "Melting Model for Modular Self Wiping Co-Rotating Twin Screw Extruders," *Polym. Eng. Sci.*, **38**, 727 (1998).

26. Potente, H., M. Bastian, "Polymer Blends in Co-Rotating Twin-Screw Extruders," *Intern. Polym. Process.*, **16**, 14 (2001).
27. Potente, H., S. Krawinkel, M. Bastian, M. Stephan, P. Potschke, "Investigation of the Melting Behavior and Morphology Development of Polymer Blends in the Melting Zone of Twin-Screw Extruders," *J. Appl. Polym. Sci.*, **82**, 1986 (2001).
28. Carneiro, O. S., A. Poulesquen, J. A. Covas, B. Vergnes, "Visualization and Analysis of the Flow along the Kneading Block of a Twin-Screw Extruder," *Intern. Polym. Process.*, **17**, 301 (2002).
29. Zhu, L., X. Geng, "Experimental Investigation of Polymer Pellets Melting Mechanisms in Co-rotating Twin-Screw Extrusion," *Adv. Polym. Tech.*, **21**, 188 (2002).
30. Wetzal, M. D., "Experimental Study of LDPE Melting in a Twin-Screw Extruder Using On-Line Visualization and Axial Pressure and Temperature Measurement," *SPE ANTEC Tech. Papers*, (2002).
31. Tadmor, Z., C. G. Gogos, *Principles of polymer processing*, John Wiley & Sons: New York, 1979.
32. Potente, H., U. Melisch, "Theoretical and Experimental Investigations of the Melting of Pellets in Co-Rotating Twin-Screw Extruders," *Intern. Polym. Process.*, **11**, 101 (1996).
33. Vergnes, B., G. Souveton, M. L. Delacour, A. Ainsler, "Experimental and Theoretical Study of Polymer Melting in a Co-Rotating Twin Screw Extruder," *Inter. Polym. Process.*, **16**, 351 (2001).
34. Qian, B., D. B. Todd, C. G. Gogos, "Plastic Energy Dissipation and Its Role on Heating/Melting of Single-Component Polymers and Multi-Component Polymer Blends," *Advan. Polym. Tech.*, **22**, 85 (2003).
35. Jung, H., J. L. White, "Investigation of Melting Phenomena in Modular Co-Rotating Twin Screw Extrusion," *Intern. Polym. Process.*, **18**, 127 (2003).
36. Wilczynski, K., J. L. White, "Melting Model for Intermeshing Counter-Rotating Twin-Screw Extruders," *Polym. Eng. Sci.*, **43**, 1715 (2003).
37. Lin, B., F. Mighri, M. A. Huneault, U. Sundararaj, "Parallel Breakup of Polymer Drops under Simple Shear," *Macro. Rapid Commun.*, **24**, 783 (2003).

38. Lee, J. K., C. D. Han, "Evolution of polymer blend morphology during compounding in a twin-screw extruder," *Polymer*, **41**, 1799 (2000).
39. Schlatter, G., C. Serra, M. Bouquey, R. Muller, J. Terrisse, "Online light scattering measurements: A method to assess morphology development of polymer blends in a twin-screw extruder," *Polym. Eng. Sci.*, **42**, 1965 (2002).
40. McCullough, T., B. Hilton, *SPE Antec Tech. Papers*, 3372 (1993).
41. Christiano, J. P., M. Lindenflezer, *SPE Antec Tech. Papers*, (1997).
42. Wetzel, M. D., D. A. Denelsbeck, S. L. Latimer, "A Perturbation Method to Characterize Reactive Extrusion," *SPE ANTEC Tech. Papers*, (2003).
43. Wetzel, M. D., C. K. Shih, U. Sundararaj, "Determination of Residence Time Distribution during Twin Screw Extrusion of Model Fluids," *SPE ANTEC Tech. Papers*, (1997).
44. Boyer, R. F., "The high temperature ($T > T_g$) amorphous transition in atactic polystyrene," *J. Polym. Sci.*, **C14**, 267 (1966).
45. Enns, J. B., R. F. Boyer, H. Ishida, J. L. Koenig, "Fourier transform infrared spectroscopic study of transitions above T_g in atactic polystyrene," *Polym. Eng. Sci.*, **19**, 756 (1979).
46. Smith, P. M., R. F. Boyer, P. L. Kumler, "A transition above T_g in amorphous polymers as shown by the spin-probe technique," *Macromolecules*, **12**, 61 (1979).
47. Curry, J., *SPE Antec Tech. Papers*, 92 (1995).
48. Chen, H., U. Sundararaj, K. Nandakumar, M. D. Wetzel, "On-Line Visualization of PS/PP Melting Mechanism in a Twin-Screw Extruder," *Intern. Polym. Process.*, **19**, 342 (2004).
49. Lin, B., U. Sundararaj, F. Mighri, M. A. Huneault, "Erosion and Breakup of Polymer Drops under Simple Shear in High Viscosity Ratio Systems," *Polym. Eng. Sci.*, **43**, 891 (2003).
50. Chen, H., U. Sundararaj, K. Nandakumar, "Modeling of Polymer Melting, Drop Deformation and Breakup under Shear Flow," *Polym. Eng. Sci.*, **44**, 1258 (2004).

Chapter 3

Heat transfer in polymer melts*

3.1 Introduction

The on-line visualization of polymer blending in chapter 2 shows that the typical environment of polymer melting during blending process consists of solid polymer particles dispersed in polymer melt. Understanding heat transfer related problems during polymer blending is one of the fundamental steps to model the blending process and control the final morphology of polymer blends. In particular, heat transfer between solid polymer pellets and a polymer melt is extremely relevant to modeling polymer blend processing. Numerical modeling is becoming a powerful tool to study the extrusion process especially considering the ever-increasing power of computers. Thus the models can incorporate physical property variations with processing conditions such as temperature and local shear rates as well as accommodate complex geometries of the polymer processing equipment.

Two basic flows are generated inside extruder channels: viz. shear flow and extensional flow. The right combination of these flows is used to achieve good mixing action. Numerous articles reveal the close relationship between polymer blend properties and its morphology (1~6). The morphology of polymer blends is determined by the individual components' properties as well as processing conditions (7~15). The detailed information of heat transfer between the barrel and polymer pellets, and between the melted polymer and polymer pellets under actual stress fields are essential

* Part of this chapter is published in paper:
Chen, H., U. Sundararaj, K. Nandakumar, *AIChE J.*, 49, 1372 (2003)

to understand the morphology development as well as to design new mixing devices. Heat transfer strongly depends on the flow conditions, such as velocity and pressure. Chandrasekaran and Karwe (16) measured the velocity profiles of a Newtonian fluid in a reversing section of a co-rotating twin-screw extruder, while Bravo et al. (17) obtained the pressure and velocity profiles in kneading elements through numerical simulations.

Sastrohartono et al. (18) and Chiruvella et al. (19) divided the flow domain in a twin-screw extruder into a translation region and intermeshing region. They also studied the heat transfer and the fluid flow for non-Newtonian polymers using numerical methods. In their study, only one component was included, thus no information about morphology development along the extrusion channel could be obtained from their models. The concept of equivalent radius was adopted by Lai and Yu (20) to study the heat transfer for blending two polymer phases in a single-screw extruder. In their model, the melting behavior of solid polymer was simplified to that of a metal, which is obviously not true for real polymers. Tenge and Mewes (21) focused on the metering zone of a twin-screw extruder and studied the heat balance experimentally. Only one phase was involved; however, viscous dissipation was included in their study. Potente's research group (22~24) concentrated on the melting of polymer granules in a twin-screw extruder to study the morphology change during melting. Mean temperature of a solid pellet and a pure drag flow model were used in their theoretical investigation of the melting process. The solution was done analytically using a steady-state approximation to what is inherently a transient heat transfer process.

In this chapter, the heat transfer characteristics between a single solid polymer pellet and a polymer melt under a predominantly shear flow condition in a batch mixer was studied experimentally. This corresponds to the initial process of a pellet heated in a polymer melt before it softens and deforms. Specifically, the temperature history at the center of an initially cold cylindrical pellet immersed in a melt was monitored. Such a history was used to back calculate a heat transfer coefficient between the pellet and the melt. The same process was modeled using the standard continuum mechanical equations and the generalized non-Newtonian model. Important variations of thermal properties with temperature were also accounted for using measured values of such properties. The equations were solved using the standard finite element tools that are available in the package FIDAP. A heat transfer coefficient was also calculated from the simulation results.

3.2 Experimental procedures

3.2.1 POLYMER PROPERTIES

Two polymers were used in the present work: viz. polyetherimide (PEI) from GE Plastics and polyethylene (PE) from Petromont, Canada. PE was the matrix phase, and PEI was the dispersed phase in the form of a pellet. PEI has a much higher softening temperature than PE, so that the PEI pellet was in the solid state during the entire process.

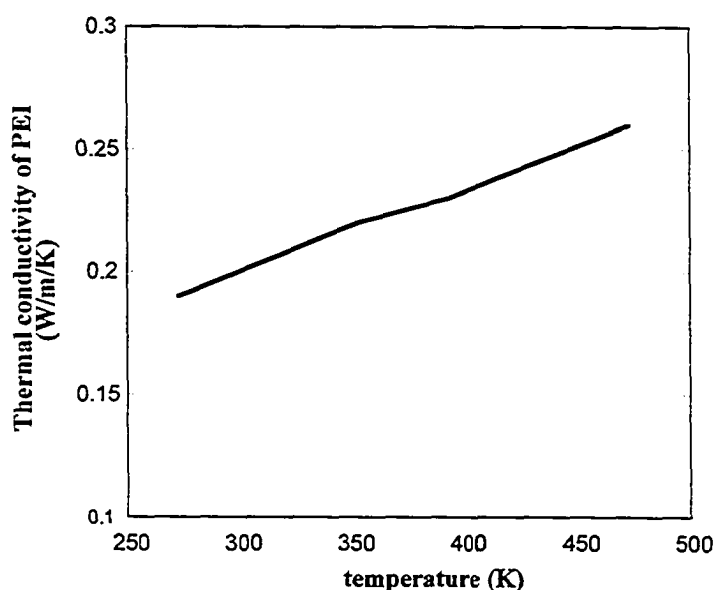


Figure 3.1 Variation of thermal conductivity with temperature for PEI (data supplied by GE Plastics).

Figure 3.1 shows the thermal conductivity of PEI as a function of temperature. The specific heat of the two polymers was measured using a TA Instruments DSC 2910, and Thermal Analyst 2200 software was used to analyze the data. The heating rate was 20 °C/min. Figure 3.2 shows the specific heat variation of PEI with temperature. For the matrix PE, a constant thermal conductivity $k_{PE} = 0.182 \text{ W/m/K}$ was used since its

temperature had small variation during the whole process (25). Its specific heat variation with temperature is shown in Figure 3.3. Since polymers melt over a range of temperatures, not at one specific temperature, we approximated the enthalpy change due to melting using specific heat data (that is, the specific heat peak in Figure 3.3 can be integrated over temperature to obtain the enthalpy change due to fusion).

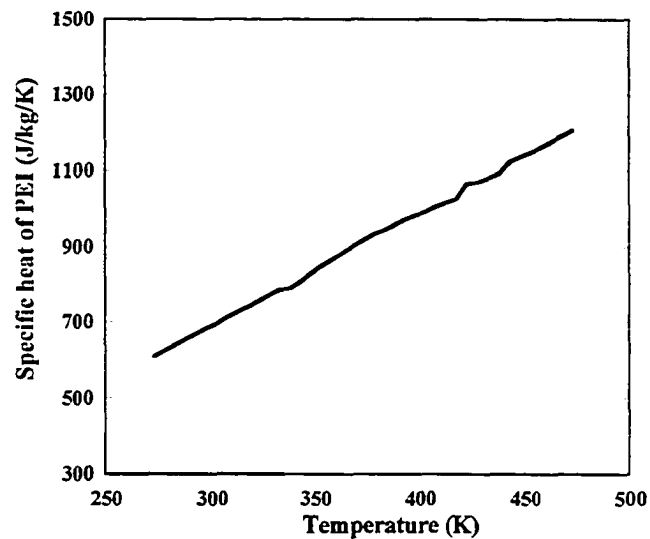


Figure 3.2 Specific heat of PEI with temperature.

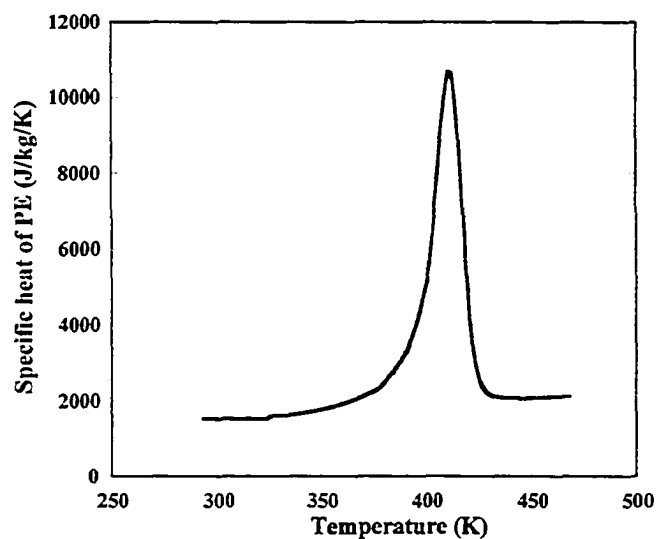


Figure 3.3 Specific heat of PE with temperature.

The dynamic rheological properties of PE were determined using a Rheometrics RMS 800 rheometer with parallel plate fixtures. Figure 3.4 shows the variation of shear viscosity of PE with frequency at different temperatures.

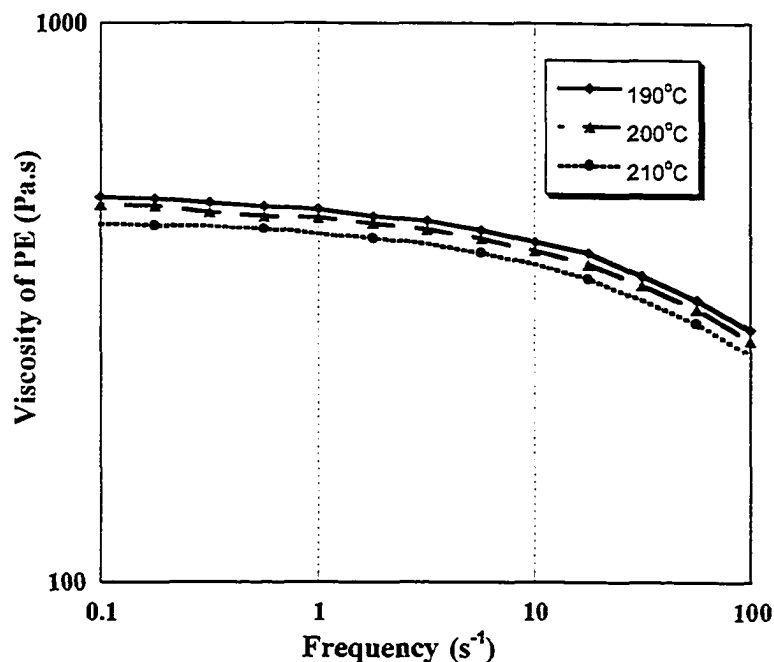


Figure 3.4 Viscosity of PE at three different temperatures.

Using the Cox-Merz rule, which states that the complex viscosity vs. frequency curve is almost exactly like the steady shear viscosity vs. shear rate curve, we were able to use the dynamic data in our model. A consistent shear thinning behavior is observed at different temperatures. A constant power law index, n can be used to capture PE shear thinning behavior. A correlation proposed by Van Krevelen et al. (26) is used to generate the functional form of the temperature dependent viscosity of PE. Based on the shear thinning and temperature effects, a generalized power law viscosity model was obtained as:

$$\eta = 350 \times 470 \times \dot{\gamma}^{(n-1)} \times \exp(-0.02 \cdot T + 1.88 \times 10^{-5} T^2) \quad (3.1)$$

where the power exponent $n = 0.9$. At lower shear rates, the viscosity was only dependent on temperature and the power law constant was set to 1.0.

3.2.2 BATCH MIXER EXPERIMENT

The Haake Rheocord 90 Torque Rheometer fitted with a series 600 internal batch mixer was used in the experiments. Two cylindrical rollers were built to generate a simple flow in the mixer. Figure 3.5 shows the experiment setup. Since we replaced the normal rollers which have indents with cylindrical rollers, the melt volume was significantly reduced by using the cylindrical rollers.

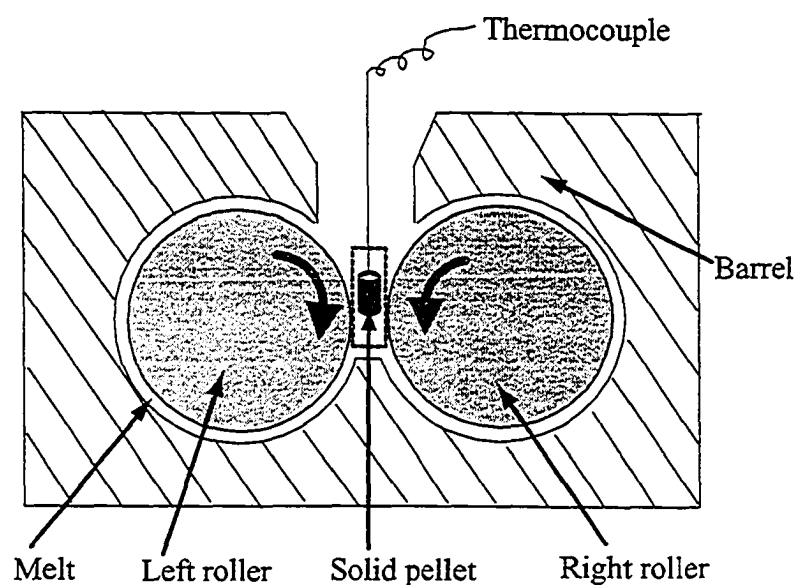


Figure 3.5 Schematic of the batch mixer experimental setup.

All materials were heated at $80\text{ }^{\circ}\text{C}$ under vacuum for 12 h before being added into the mixer. The barrel temperature of the mixer was preheated to $190\text{ }^{\circ}\text{C}$, and the motor speed was set at 50 rpm. About 16 g PE was added to the mixer to form the melt phase. To record the temperature history of the pellet, a small hole was drilled along the

cylinder axis of the PEI pellet, but not through the full length of the pellet. The size of the hole was carefully controlled so that a thermocouple could be inserted into the hole and the thermocouple was in close contact with the inner surface of the hole in the pellet. Epoxy was used to glue the thermocouple with the pellet so that there was no air between the surfaces to create any thermal contact resistance. The thermal conductivity ($k = 0.20\text{W/m/K}$) of the epoxy was comparable to the solid PEI pellet. Before the PEI pellet was inserted into the PE melt, the PE melt temperature was measured, and its value was set as the reference temperature for the corresponding simulations. For our experiment, the reference temperature was measured to be $197\text{ }^{\circ}\text{C}$. The temperature history of the central point was recorded at every 0.1 s using an OPTO 22 data acquisition system.

The classic analytical solution for transient conduction heat transfer from a cylindrical pellet to an infinite medium subject to a convective boundary condition was used to determine the mean heat transfer coefficient on the melt side by matching the experimentally measured temperature history at the center of the pellet with the analytical model. This method involves using the superposition of transient solutions that is well documented in standard heat transfer textbooks (27). Table 3.1 summarizes all the parameters that are used in the calculation.

Table 3.1 Parameters of PEI pellet used in calculating the mean h -value from experimental data.

ρ (kg/m^3)	C_p (J/kg/K)	k (W/m/K)	T_{ref} (K)	D (mm)	L (mm)
1270	938	0.23	470	2.0	12

Figure 3.6 shows the flow diagram to calculate the mean \bar{h} -value from experimental data (see ref. 28 for transient infinite cylinder and infinite plane wall equations).

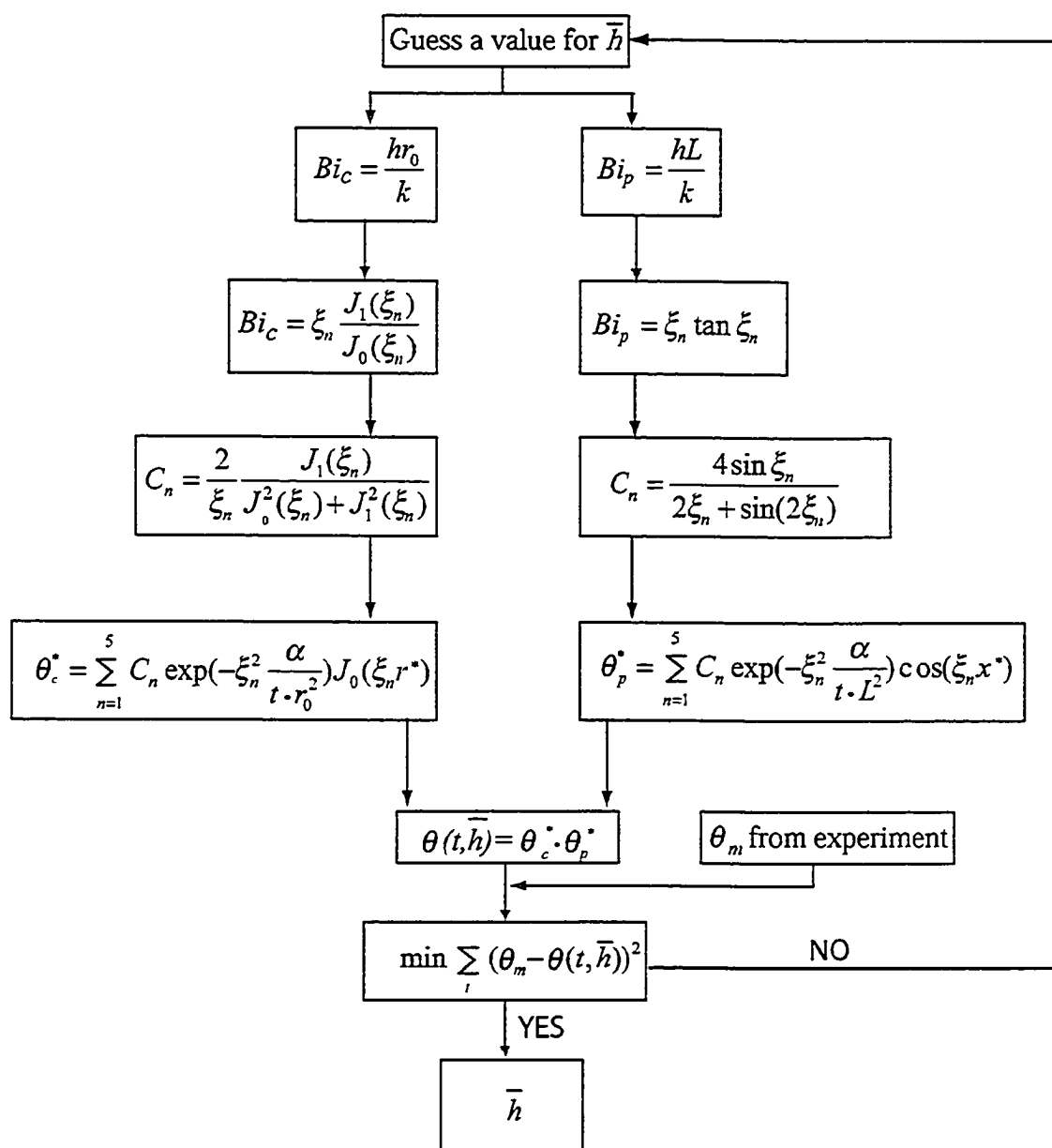


Figure 3.6 Flow diagram for calculating the mean heat transfer coefficient, \bar{h} , from the experimental temperature history.

This model, of course, assumes that all the cylindrical surfaces are exposed to the same heat transfer environment at all times, hence what we calculate as a heat transfer

coefficient from this approach can be thought of as an effective mean heat transfer coefficient from the pellet on the melt side. In particular it is to be treated as an average over the interface and over the time interval. We can only obtain this effective mean heat transfer coefficient from the single temperature measurement made in the experiment. In the actual experiments, since there is an unsymmetrical flow around the pellet, and the viscosity is a function of temperature, the heat transfer environment around the pellet-melt interface will not be uniform in space and time and the heat transfer coefficient changes with space and time. Such variation will be taken into account in the simulations.

3.3 Model equations

The governing equations are the standard conservation laws for mass, momentum, and energy. The following assumptions were made to model the flow around the pellet that is placed in the gap between two cylindrical rollers. The melt is assumed to be incompressible and inelastic, but its viscosity obeys the generalized power law. Viscous dissipation is included in the energy equation for the melt phase. The polymer melt is assumed to be in perfect contact with the pellet, and, hence, the contact resistance between the melt and the pellet is assumed to be zero. For the PE melt, the governing equations are as follows

Continuity equation:

$$\nabla \cdot V = 0 \quad (3.2)$$

Momentum equation:

$$\rho \left(\frac{\partial V}{\partial t} + V \cdot \nabla V \right) = -\nabla P + \nabla \cdot \overline{\tau} \quad (3.3)$$

where the shear stress, τ , is related to the rate of strain tensor, D through

$$\overline{\tau} = 2\eta(\dot{\gamma}, T) \overline{D} \quad (3.3a)$$

and η is the non-Newtonian viscosity which has the following form.

$$\eta = \eta_0 m e^{(-aT + bT^2)} \dot{\gamma}^{(n-1)} \quad (3.3b)$$

Energy equation:

$$\rho C_p \left(\frac{\partial T}{\partial t} + V \cdot \nabla T \right) = \nabla \cdot (k \nabla T) + \overline{\tau} : \nabla V \quad (3.4)$$

The energy equation was used for the PE melt. Because the velocity is zero inside the pellet and there is no viscous dissipation, for the PEI pellet, the energy equation is reduced to the following transient heat conduction equation:

$$\rho C_p \frac{\partial T}{\partial t} = \nabla \cdot (k \nabla T) \quad (3.5)$$

Boundary conditions:

Two 2-D models were built to simulate the flow in the gap between the two cylinders of the batch mixer. To capture the flow characteristics of the experiment, there are two possible orientations for the pellet in the simulations. If we assume the axis of the cylinder is in the z-direction perpendicular to the paper and infinitely long in that direction, the pellet then can be orientated either as a circle perpendicular to the axis of the cylinder or as a rectangle parallel to the axis of the cylinder. The geometry and boundary conditions are shown in Figure 3.7a and 3.7b.

All the material properties used in the simulations are summarized in Table 3.2. Obviously, there are important geometrical differences between the experiments and the 2-D simulations.

Table 3.2 Property values of PE and PEI used in the simulations.

Sample	ρ (kg/m ³)	C_p (J/kg/K)	k (W/m/K)	η (Pa.s)
PE	954	Figure 3.3	0.182	Equation 3.1
PEI	1270	Figure 3.2	Figure 3.1	Solid

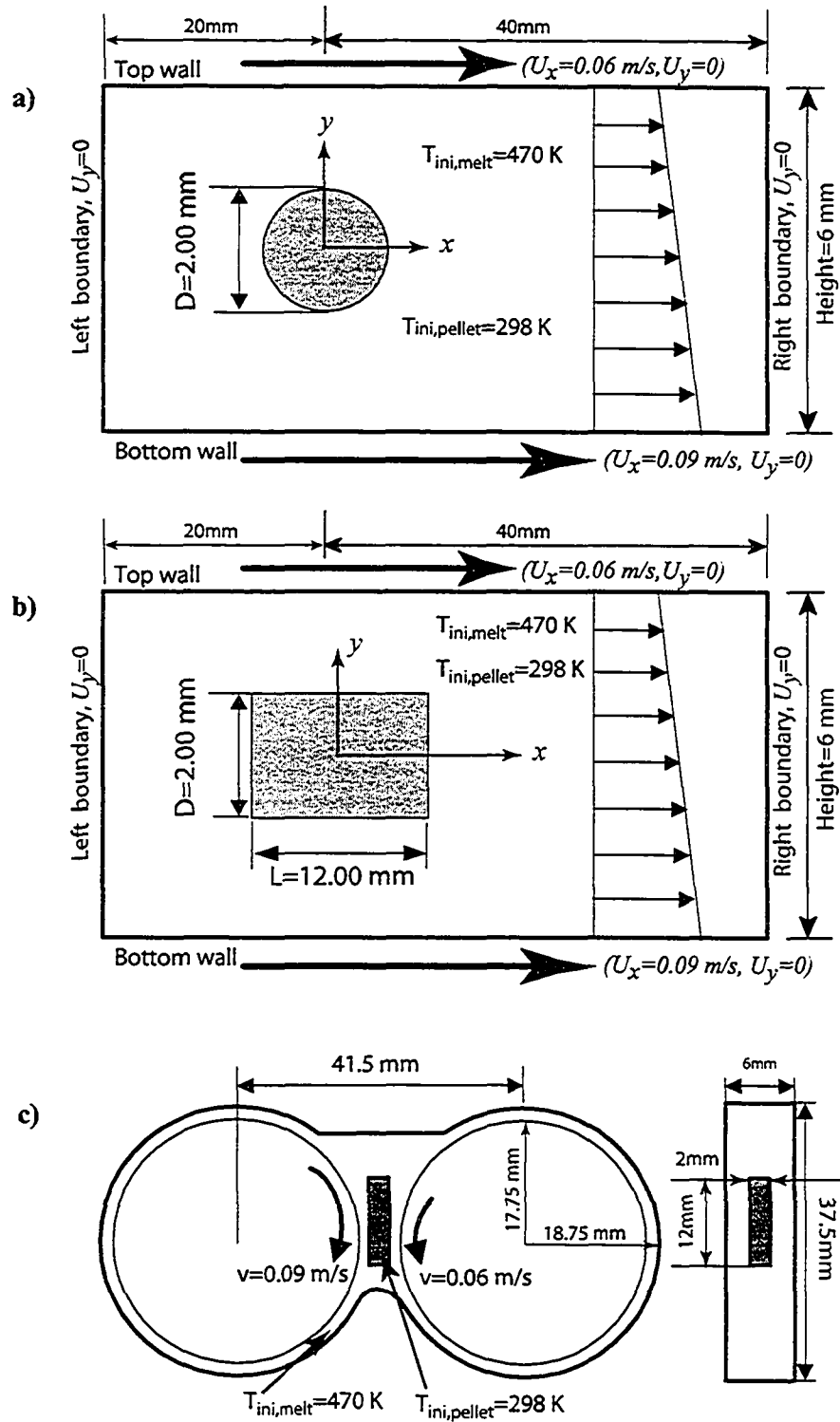


Figure 3.7 Geometric model and boundary conditions a) two-dimensional approximation with axis perpendicular to flow, b) two-dimensional approximation with axis parallel to flow c) three-dimensional geometry of the batch mixer. (figures not to scale).

To eliminate the geometry difference, a 3-D batch mixer geometry was built and is shown in Figure 3.7c. The 3-D geometry is the same as the experimental setup except for the length of the cylinders, which was reduced from 47 mm to 6 mm to save computational cost. Even so, the time required for the 3-D simulation was about 10 times longer than the time required for the 2-D cases. Therefore, if the 2-D representations are accurate, it would be advantageous to use them in future modeling efforts. The finite element grid distributions are shown in Figure 3.8a-c for the three geometrical variations.

The 2-D geometries are treated as open systems with inflow and outflow boundaries, while the 3-D geometry is a closed system with all of the polymer melt inside the batch mixer. A no-slip condition is imposed at all of the wall boundaries. For 2-D case, at the left and right boundaries, the vertical component of the velocity is set to zero, but the horizontal component is computed by the Galerkin finite element method (FEM). For the temperature, an isothermal condition is imposed on the walls with the temperature being equal to the initial melt temperature, while the interface between the melt and the pellet have the same temperature on the melt and pellet side of the interface.

The heat flux across the interface is also imposed to be continuous. For the velocities, the no-slip condition is also imposed at the pellet-melt interface. Note that the two rollers in the experiments rotate at different speeds; the right roller rotates at two-thirds the speed of the left roller. Hence the upper and lower plate velocities in the case of 2-D simulations are set at 0.06 and 0.09 m/s respectively and, of course, the 3-D simulation uses the different speeds for the two rollers.

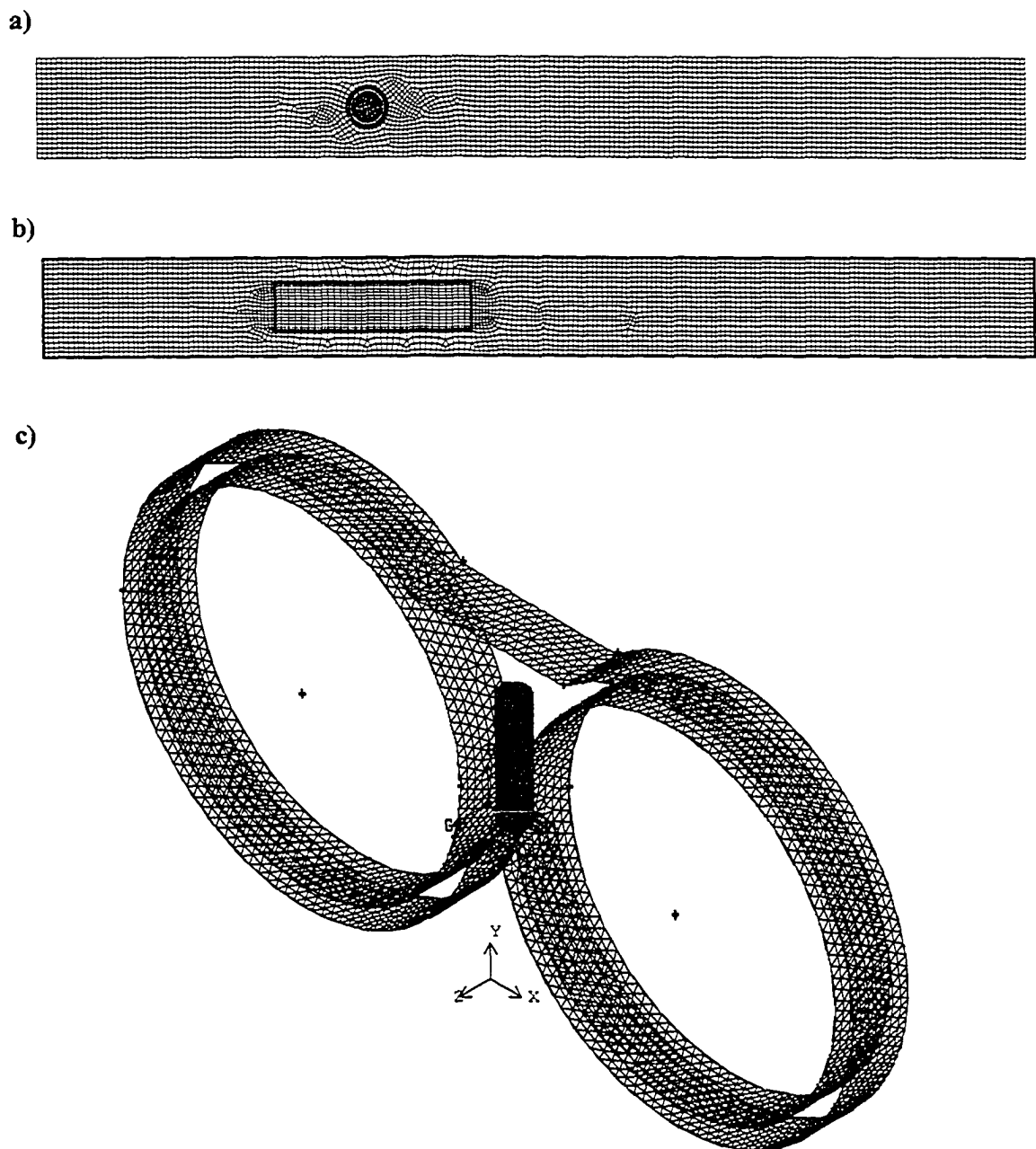


Figure 3.8 Finite element grid distribution for the three geometries considered in this work: a) 2D simulation with axis perpendicular to the flow; b) 2D simulation with axis parallel to the flow; c) 3D simulation.

The successive substitution (S.S.) method was used to solve the non-linear system of equations at each time step using the solver FIDAP version. 8.6. The time

integration was performed using the backward Euler method. Once the solution is obtained, macroscopic quantities like average temperature or heat transfer coefficients can be computed at each instant of time. The local heat transfer coefficient at every point on the interface is calculated from the equation

$$h_i = \frac{q_i''}{T_{ref} - T_i} \quad (3.6)$$

where q_i'' is the local heat flux at a point on the interface that is computed from Fourier's law applied on the pellet side using, $q'' = -k\nabla T$, T_{ref} is the reference temperature, which is 470 K for this work, and T_i is the local interface temperature. The local heat transfer coefficient can then be integrated over the interface A_i to get an average heat transfer coefficient at each instant of time from

$$\bar{h}(t) = \frac{\int h_i dA_i}{A_i} \quad (3.7)$$

The time average heat transfer coefficient \bar{h} is found using

$$\bar{h} = \frac{\sum_{n=1}^N \bar{h}(t)}{N\Delta t} \quad (3.8)$$

where Δt is the time step and N is the number of time steps.

3.4 Results and discussion

3.4.1 EXPERIMENTAL RESULTS

Figure 3.9 shows the pellet's inner temperature vs. time for the experiment and the three different simulations. The time for the pellet to reach the reference temperature from 3-D simulation matches well with the time from the experiment, although there are important differences in the temperature history that require further scrutiny, namely, the rates of temperature increase in the simulations were not the same as that in the experiment even for the 3-D simulation. This is attributed to the dynamics of the thermocouple.

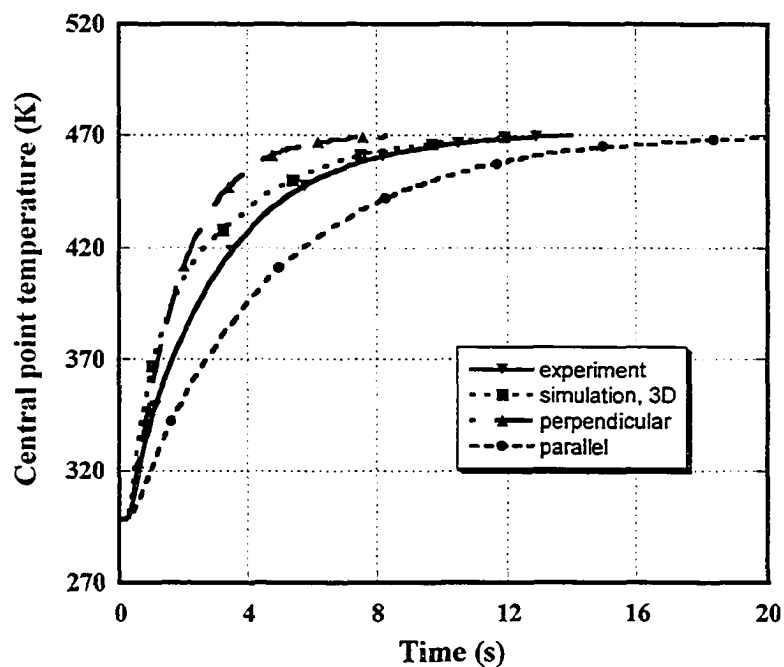


Figure 3.9 Comparison of the experimentally measured center point temperature with those predicted from the simulations. Thermocouple dynamics were not accounted for.

Every type of thermocouple has its own characteristic dynamics. A first-order time constant is widely used to capture this. To measure the time constant of the

thermocouple, we used the OPTO 22 data acquisition system to record its temperature history after inserting the thermocouple into an oil bath held at a certain temperature. The time when the recorded temperature reached 63% of the final temperature was taken to be the thermocouple's time constant for the measuring temperature. An average time constant was calculated based on time constants obtained with different bath temperatures. According to our measurement, we found that the time constant of the thermocouple used in the experiment is about 0.9 s. This value is very close to the time constant of 1.0 s supplied by the thermocouple manufacturer (Omega Engineering, Inc.). The first order process approximation of the thermocouple was employed to shift the data from the 3-D simulation to include the thermocouple dynamics, and to shift the data from experiment to remove the thermocouple dynamics to see how well the two sets of data matched. Figure 3.10 shows the block diagrams of the two process approximations.

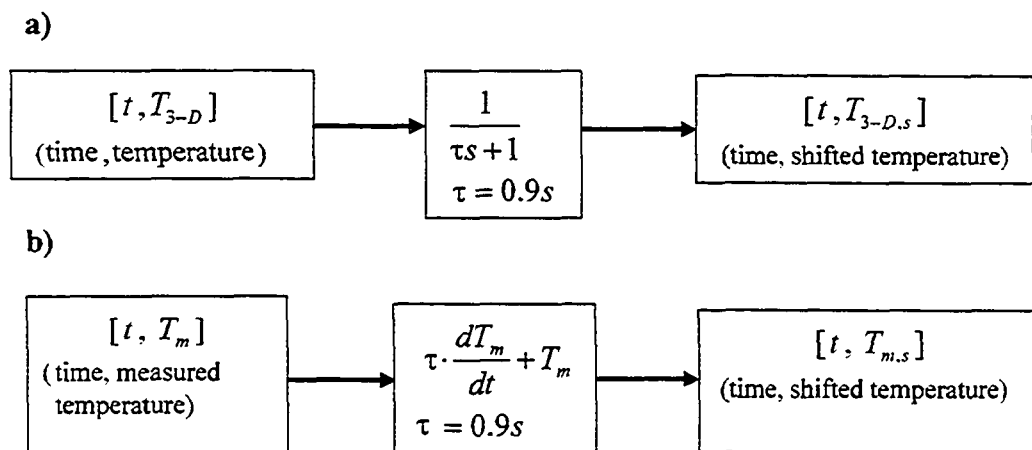


Figure 3.10 First order process approximation of the thermocouple dynamics (time constant=0.9s): a) model used to shift the 3D simulation curve to include thermocouple delay; b) model used to shift the experimental curve to remove thermocouple delay.

The thermocouple dynamics were added to the simulation result, and the shifted curve is shown in Figure 3.11a.

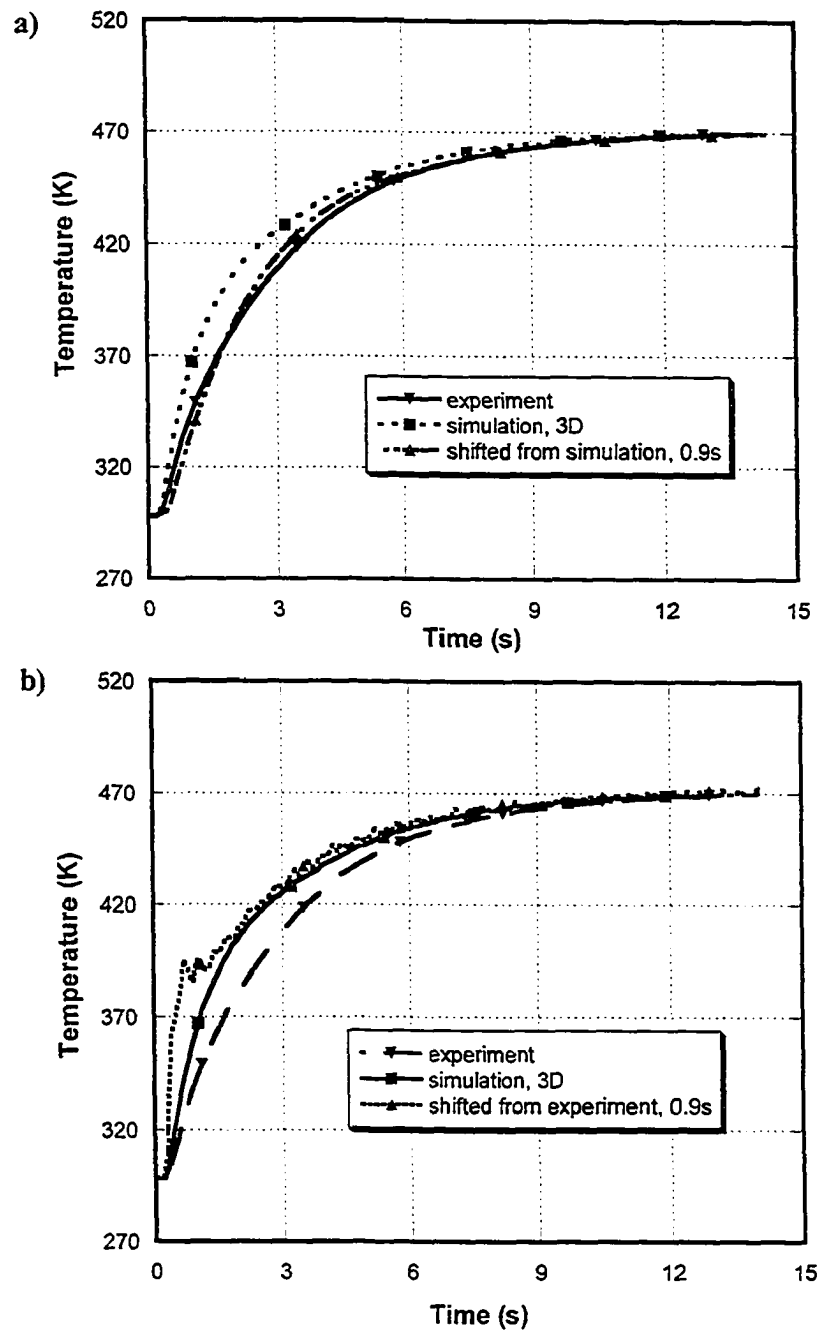


Figure 3.11 Results of shifting 3D simulation and experiment data using a first order process approximation with time constant 0.9s: (a) simulation curve shifted to include thermocouple delay, and (b) experimental curve shifted to remove thermocouple delay.

The measured experimental curve is also shown for comparison. It can be seen that the shifted simulation curve and the measured data match quite well. The thermocouple dynamics were removed from the experimental data, and the shifted curve is shown in Figure 3.11b. Again, we see that simulation and experiment match well if we account for the thermocouple dynamics. In the initial stages, since temperature was differentiated with time to shift the measured experimental data, a small variation in the recorded temperature could cause large oscillations, as seen in Figure 3.11b. The discrepancy at the initial stage may also be due to the heat transferred into the polymer pellet through the thermocouple itself during experiments, which would cause the central temperature to rise faster in the experiment than in the simulation, while at later stages, heat was taken out from the pellet because the temperature of the thermocouple was higher than the air outside the batch mixer. This may explain why the temperature rise in the experiment is slower than that seen in the shifted simulation curve (see Figure 3.11a).

Based on the uncorrected experimental temperature history and using the algorithm outlined in Figure 3.6, the mean h -value from the experiment was computed to be $\bar{h} = 370 \text{ W/m}^2/\text{K}$. This \bar{h} -value was obtained based on the assumption of uniform convective environment and the thermocouple's dynamics were not accounted for. To shift the experimental curve to account for the thermocouple dynamics, we needed to take a derivative of the measured temperature (see Figure 3.10b), which created error and oscillations as shown in Figure 3.11b. Therefore, we used the uncorrected data for the initial determination of the \bar{h} -value. Figure 3.12 shows the

comparison between the curve from experiment and the one predicted using a constant value of $\bar{h} = 370 \text{ W/m}^2/\text{K}$.

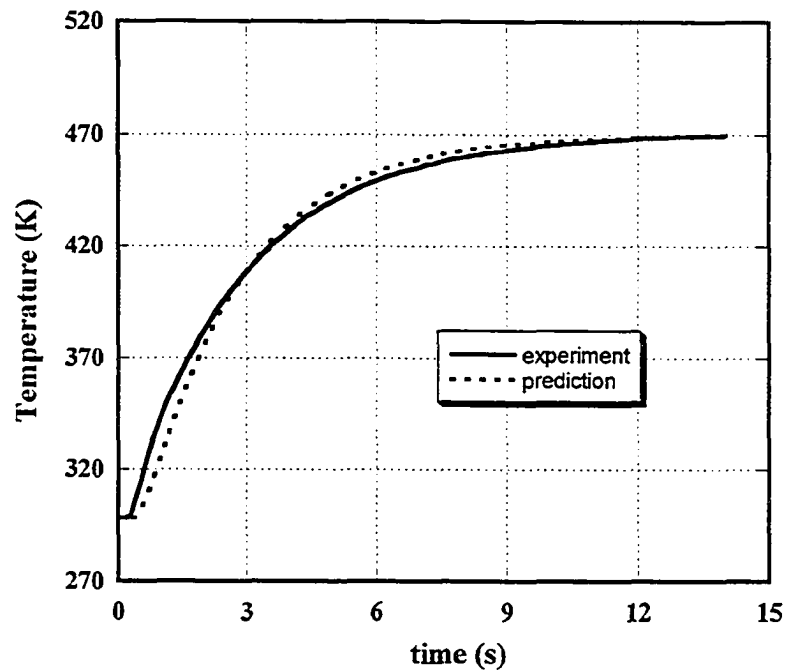


Figure 3.12 Comparison of the center point temperature curves from the experiment and that predicted with $h=370 \text{ W/m}^2/\text{K}$ using algorithm outlined in Figure 3.6.

It is seen that the predicted temperature rises slower than the experimental one initially, and at later times, the slope of the predicted curve is greater than the experimental one. The discrepancy between the two curves may be due to the assumptions we made. While the same algorithm (Figure 3.6) can and will be used to determine an average heat transfer coefficient from each of the simulations, such a calculation would be subject to the same assumptions as uniform convective environment, which is a necessary assumption in the case of experimental data, but an unnecessary one in the case of simulation, as local and average heat transfer coefficient can be calculated according to Eqs. 3.6 and 3.7.

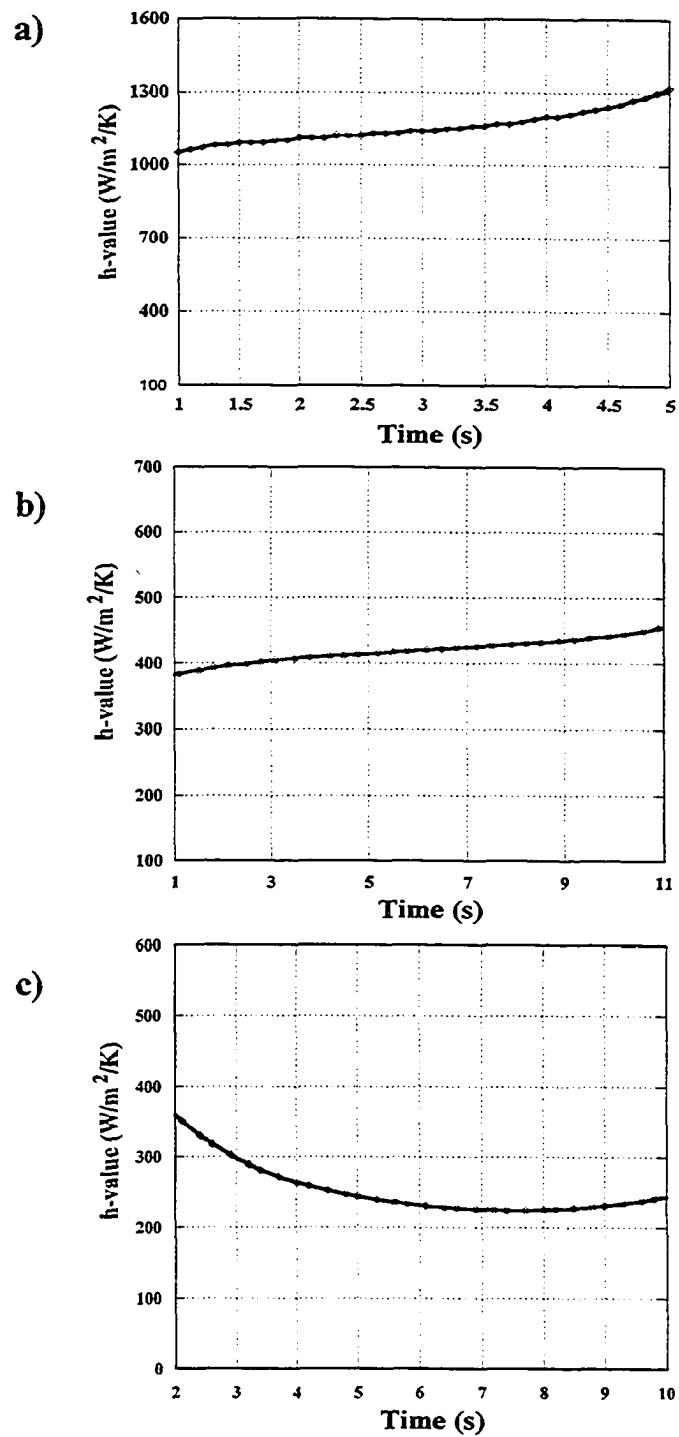


Figure 3.13 Variation of spatially averaged h -values with time: a) 2D simulation with axis perpendicular to the flow ($h=1160$ W/m²/K); b) 2D simulation with axis parallel to the flow ($h=420$ W/m²/K); c) 3D simulation ($h=250$ W/m²/K).

Figure 3.13a-c presents heat transfer coefficients obtained from Eqs. 3.6 and 3.7 vs. different times from the 2-D and 3-D batch mixer simulations. Since the heat flux at the interface has a singularity (infinite heat flux) at $t=0$, there are large numerical errors at the beginning of the simulation. Similarly at the end of the simulation, temperatures at some nodes along the interface are almost equal to the reference temperature, leading to division by zero in the heat transfer coefficient calculation, and thus resulting in large errors. Hence the results for heat transfer coefficients are presented for a certain time range. Using Eqs. 3.6 - 3.8, the average heat transfer coefficients for each of the three cases were determined to be 1160, 420 and 250 $\text{W/m}^2/\text{K}$ for the 2-D circle, 2-D rectangle and 3-D cylinder, respectively. Table 3.3 summarizes all the calculated heat transfer coefficients and the time ranges used to calculate them.

Table 3.3 Summary of heat transfer coefficients from experiment and simulations.

Data source and method	\bar{h} ($\text{W/m}^2/\text{K}$)	Time range (s)
2D simulation-circle ^a	1160	1~5
2D simulation-rectangle ^a	420	1~11
3D simulation-cylinder ^a	250	2~10
Measured data from experiment ^b	370	0~14
Data removing time delay from experiment ^b	>600	0~14
Data from 3D simulation-cylinder ^b	>600	0~14
Churchill correlation	210	

a: integration from local heat transfer coefficient - Equations (3.6)-(3.8)

b: algorithm outlined in Figure 3.6

Heat transfer for an infinite length circular cylinder in cross flow is correlated by the Churchill equation (28).

$$\overline{Nu}_D = 0.3 + \frac{0.62 Re_D^{1/2} Pr^{1/3}}{[1 + (0.4/Pr)^{2/3}]^{1/4}} \left[1 + \left(\frac{Re_D}{282000} \right)^{5/8} \right]^{4/5} \quad (3.9)$$

where the Reynolds number is $Re_D = 0.00039$ and the Prandtl number is $Pr = 4.3 \times 10^6$ for this work. From this correlation, the mean heat transfer coefficient was calculated to be $210 \text{ W/m}^2/\text{K}$. Although the flow condition is different from our experiment, the value is surprisingly close to the one found from the simulation results. Rao (29) provided another correlation for non-Newtonian flows over a cylinder in cross flow. Using this correlation, the calculated heat transfer coefficient is over $2000 \text{ W/m}^2/\text{K}$; however, the Re number and Pr number in our work are not within the ranges specified for use of this correlation.

Based on the shifted experimental curve shown in Figure 3.11b, using the algorithm outlined in Figure 3.6, the mean heat transfer coefficient, \bar{h} , was calculated to be between 600 and $650 \text{ W/m}^2/\text{K}$. This value is much larger than the value obtained by averaging the local heat transfer coefficients from the 3-D simulations ($250 \text{ W/m}^2/\text{K}$). For comparison, the same algorithm (shown in Figure 3.6) was used to calculate \bar{h} based on the center point temperature data from the 3-D simulation; however, the calculated value for \bar{h} was also over $600 \text{ W/m}^2/\text{K}$, which is not consistent with the value calculated using the heat flux and temperature data from the simulation ($250 \text{ W/m}^2/\text{K}$). Therefore, the assumption of an even convective environment used in the algorithm outlined in Figure 3.6 is not an acceptable one to calculate \bar{h} . If we consider real polymer pellets used in polymer processing, which are short cylinders with L/D of about one, the assumption of uniform convective environment is even less valid.

We can see the match between the simulation and the experiment by comparing the center point temperature curves obtained from the 3-D simulation and the experiment. From Figure 3.11, we see that the simulation and experimental temperature vs. time curves match well if we account for the thermocouple dynamics. Therefore, we can assert that the heat transfer coefficient obtained from simulation is the correct heat transfer coefficient, since it accounts for the uneven convective environment.

Comparison between the experiment and the simulations shows that the 3-D simulation represents the experimental process the best. From the simulation, we can get a more accurate value for the heat transfer coefficient than that from the experiment because no assumption for even convective environment and no effect of thermocouple dynamics were included in the calculation of the heat transfer coefficient value for the 3-D simulation.

3.4.2 SIMULATION RESULTS

One major advantage of the numerical modeling is that detailed information can be extracted from the simulation result. Figure 3.14 shows the temperature contour and the velocity vectors at a time of 1 s.

The velocity has reached its fully developed state already, and dynamic changes in flow due to changes in viscosity near the pellet are small. The effects of heat conduction inside the pellet and heat convection outside the pellet are clearly seen in this figure as shaded contours. The heat transfer inside the pellet is seen to have progressed to a significant level even after 1 s. In the 2-D simulations, because the

velocity of the bottom surface (left roller) is greater than that of the top surface (right roller), a degree of unevenness in the cold region is seen near the faster moving surface.

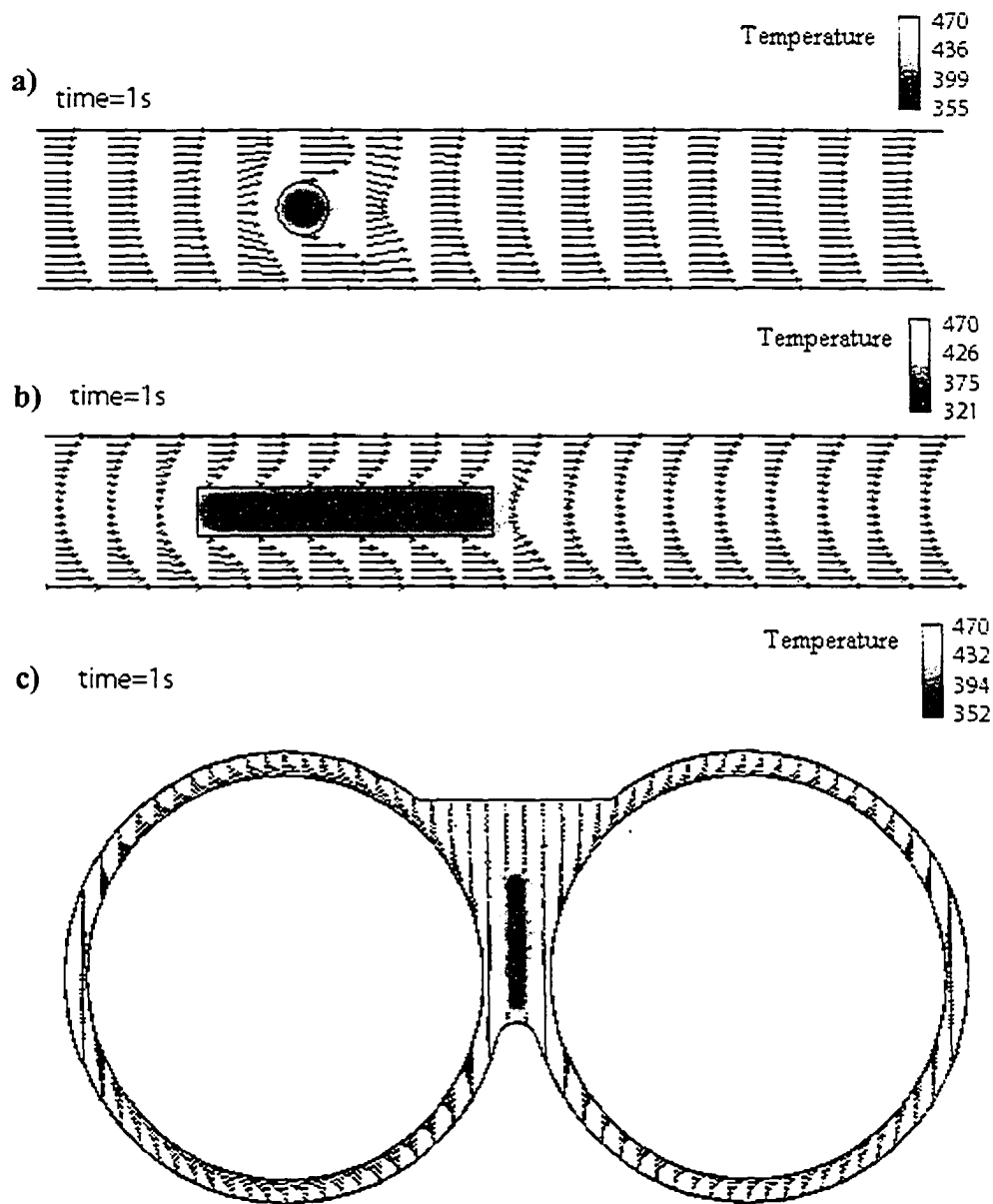


Figure 3.14 Temperature profile and vector plots of the velocity field for the three cases are shown at the end of 1 s: a) 2D simulation with axis perpendicular to the flow; b) 2D simulation with axis parallel to the flow; c) 3D simulation.

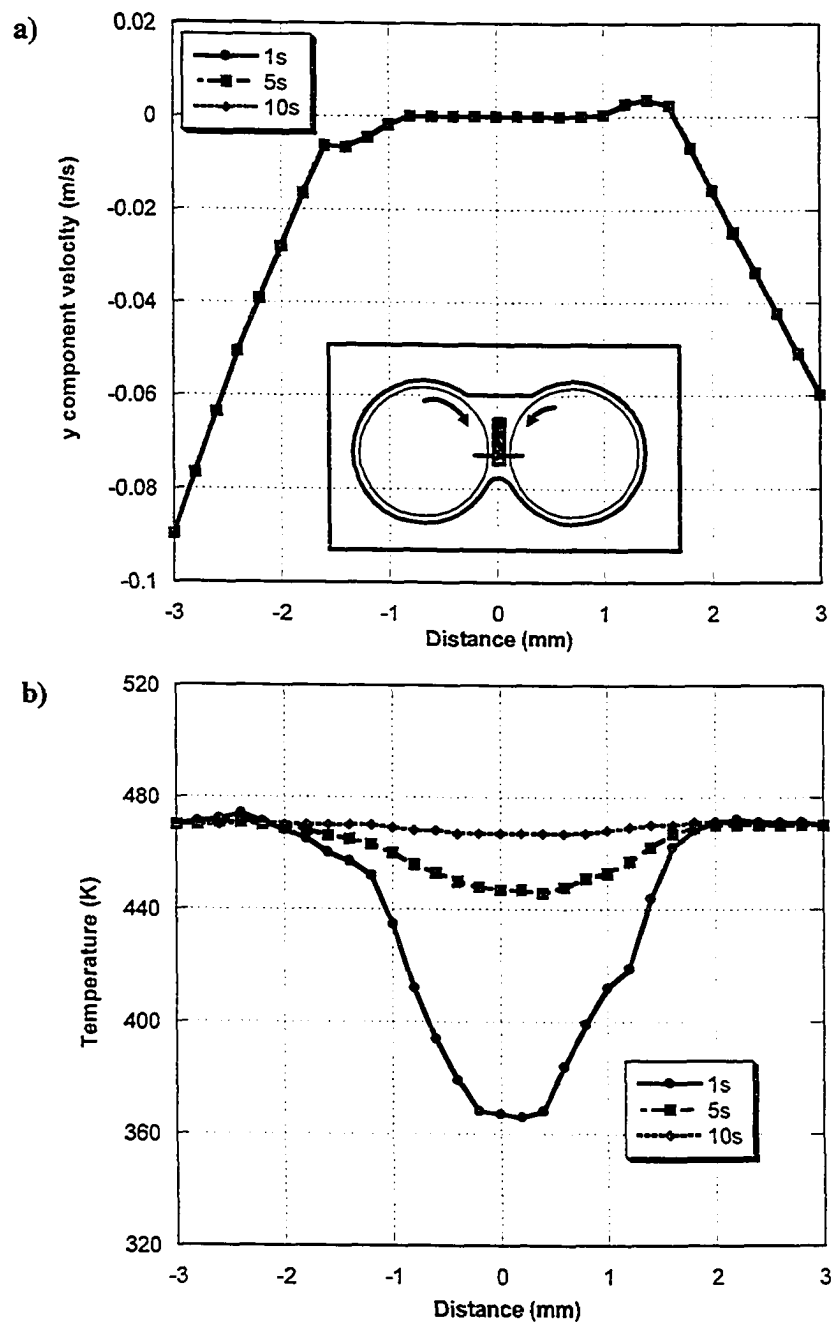


Figure 3.15 a) Y component velocity variation and b) Temperature variation from the three-dimensional simulation along x, ($y=0$, $z=-3$). The sampling line cuts across the pellet as shown in the inset. Axes are defined in Figure 3.8c.

To obtain detailed quantitative results from the 3-D simulation, variation of field quantities along a line parallel to the x-axis through ($y=0.0$, $z=-3.0$), which crosses the pellet at the location of the thermocouple was chosen (Figure 3.8c shows the x, y, z directions). Figure 3.15a and 3.15b show, respectively, the U_y variation and the temperature variation along the chosen line at three different times of 1, 5, and 10 s. The vertical component of the velocity, shown in Figure 3.15a, shows that the velocity varies linearly in the gap, except near the pellet surface due to temperature dependent viscosity effects, and it is identical at all three sampling times. From detailed examination of the velocity profiles near the pellet, we saw that there were eddies near the surface of the pellet. For example, the y-component velocity near the right roller at the sampling line is going up or is positive (see Figure 3.15a) and the melt re-circulates down at a higher z position. It can be seen in Figure 3.15b that the temperature at the core of the pellet has already changed at 1 s from its initial value of 298 K to over 350 K. At $t=5$ s and 10 s, the temperature near the left roller (which moves faster) is slightly higher than near the right roller. Actually, the maximum temperatures at $t=5$ s and 10 s are several degrees higher than 470 K. This is due to a higher rate of viscous heating near the pellet surface, which experiences a higher shear rate. As expected, the rate of temperature change between 5 and 10 s is smaller as the temperature driving force decreases with time.

For a non-Newtonian fluid, like the PE melt in this work, shear rate is another important parameter that affects the flow, and hence the heat transfer. Figure 3.16 shows the shear rate along the same line across the pellet at three sampling times. Within the solid pellet, the shear rate is always zero. At the interface, the shear rate

reaches its maximum value. The different velocities of the left and right roller result in the unsymmetrical shear rate profiles. There is almost no difference between the profiles at the three times. This result again conforms to the expectation that the shear rate is higher near the left roller and that the flow changes very little with time.

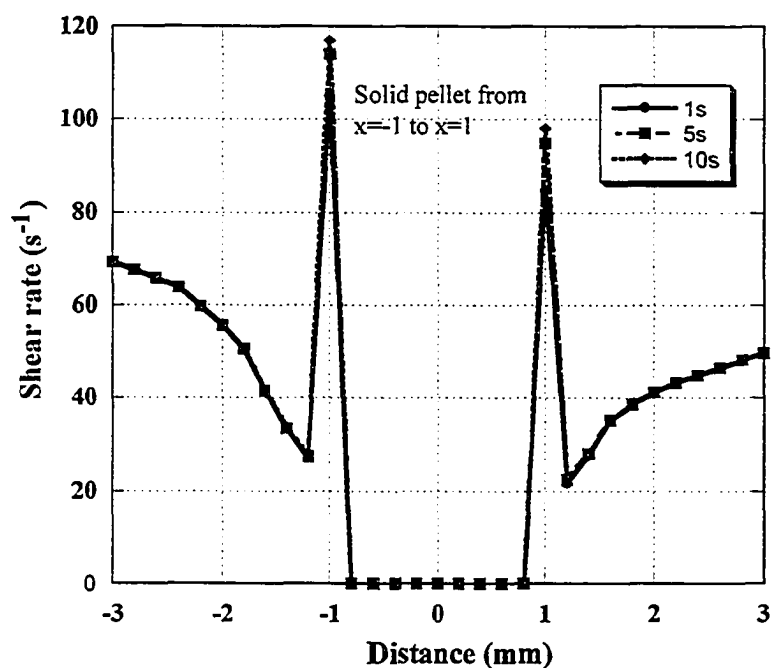


Figure 3.16 Shear rate plots along a line through the pellet from the three dimensional simulation at different times. The location is along x , ($y=0$, $z=-3$). Axes are defined in Figure 3.8c.

As previously mentioned, the viscosity of PE depends on temperature and shear rate. Figure 3.17 gives the viscosity variation at different times along the same line through the pellet. There is no viscosity for the solid PEI pellet (distance: -1 mm to 1 mm). From Figure 3.16, we see that the shear rate is higher at the interface and that it is highest on the left hand side (where the roller is moving faster). Since polymer melts are shear thinning, high shear rate corresponds to low viscosity, and low shear rate corresponds to high viscosity. Hence the viscosity should be lower at the interface and it

should be lowest near the left side, as seen in Figure 3.17. Furthermore, the effect of temperature on the viscosity can be seen. The initially cool pellet reduces the temperature of the surrounding melt at early times, and hence, the viscosity at $t=1$ s is higher than at subsequent times.

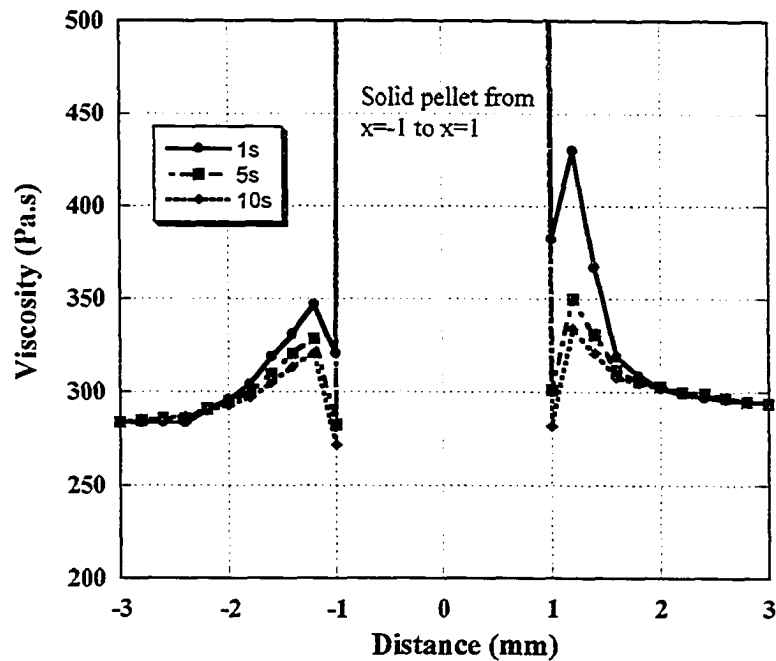


Figure 3.17 Viscosity plots along a line through the pellet from the three dimensional simulation at different times. The location is along x , ($y=0$, $z=-3$). Axes are defined in Figure 3.8c.

For any time greater than 10 s, there is little temperature variation, so only shear rate affects the viscosity. Even at $t=1$ s, the sharply increased shear rate very close to the interface dominates the changes in viscosity and the viscosity decreases resulting in the steeper velocity gradient near the interface seen in Figure 3.15a. Obviously, compared to an experiment, much more detailed information about the process can be extracted from the numerical modeling results.

3.5 Summary

The heat transfer coefficient was determined experimentally and numerically for a polymer pellet in an intensive mixing flow. Two 2-D and one 3-D geometries were built for the numerical simulations. The 3-D simulation represents the experiment the best. In the experiment, the dynamics of the thermocouple had a significant influence on the temperature history of the pellet. There was some discrepancy between the temperature curves from the experiment and the 3-D simulation, but by adjusting the data using the thermocouple dynamics, the two temperature curves matched very well. The time for the pellet to reach the reference temperature and the center point temperature history obtained from the experiment match well with values obtained from the 3-D simulation. Simulation results allowed us to understand the experiment better, and we were able to obtain a more representative heat transfer coefficient, since we could account for the uneven convective environment in the mixer. It was shown that shear rate and viscosity varied significantly near the pellet surface.

3.6 References

1. Wu, S., "Phase Structure and Adhesion in Polymer Blends - a Criterion for Rubber Toughening," *Polymer*, **26**, 1855 (1985).
2. Bucknall, C. B., F. F. P. Cote, I. K. Partridge, "Rubber Toughening of Plastics 9: Effects of Rubber Particle Volume Fraction on Deformation and Fracture in HIPS," *J. Mater. Sci.*, **21**, 301 (1986).
3. Favis, B. D., J. P. Chalifoux, "The Effect of Viscosity Ratio on The Morphology of Polypropylene Polycarbonate Blends During Processing," *Polym. Eng. Sci.*, **27**, 1591 (1987).
4. Majumdar, B., H. Keskkula, D. R. Paul, "Mechanical Properties and Morphology of Nylon-6/Acrylonitrile-Butadiene-Styrene Blends Compatibilized with Imidized Acrylic Polymers," *Polymer*, **35**, 5453 (1994).
5. Sundararaj, U., Y. Dori, C. W. Macosko, "Sheet Formation in Immiscible Polymer Blends," *Polymer*, **36**, 1957 (1995).
6. Kudva, R. A., H. Keskkula, D. R. Paul, "Morphology and Mechanical Properties of Compatibilized Nylon 6/Polyethylene Blends," *Polymer*, **40**, 6003 (1999).
7. Willis, J. M., V. Caldas, B. D. Favis, "Processing Morphology Relationships of Compatibilized Polyolefin Polyamide Blends 2: The Emulsifying Effect of an Ionomer Compatibilizer as a Function of Blend Composition and Viscosity Ratio." *J. Mater. Sci.*, **26**, 4742 (1991).
8. Utracki, L. A., Z. H. Shi, "Development of Polymer Blend Morphology During Compounding in a Twin-Screw Extruder 1: Droplet Dispersion and Coalescence - A Review," *Polym. Eng. Sci.*, **32**, 1824 (1992).
9. Sundararaj, U., C. W. Macosko, "Drop Breakup and Coalescence in Polymer Blends: The Effects of Concentration and Compatibilization," *Macromolecules*, **28**, 2647 (1995).
10. Sundararaj, U., "Effect of Processing Parameters on Phase Inversion during Polymer Blending," *Rev. Makrom. Chem. Makrom. Symp.*, **112**, 85 (1996).
11. Huneault, M. A., Z. H. Shi, L. A. Utracki, "Development of Polymer Blend Morphology during Compounding in a Twin-Screw Extruder 4: A New Computational Model with Coalescence," *Polym. Eng. Sci.*, **35**, 115 (1995).

12. Oshinski, A. J., H. Keskkula, D. R. Paul, "The Role of Matrix Molecular Weight in Rubber Toughened Nylon 6 Blends 1: Morphology," *Polymer*, **37**, 4891 (1996).
13. Levitt, L., C. W. Macosko, S. D. Pearson, "Influence of Normal Stress Difference on Polymer Drop Deformation," *Polym. Eng. Sci.*, **36**, 1647 (1996).
14. Li, H. X., G. H. Hu, and J. A. Sousa, "The Early Stage of the Morphology Development of Immiscible Polymer Blends During Melt Blending: Compatibilized vs. Uncompatibilized Blends," *J. Polym. Sci. B Polym. Phys.*, **37**, 3368 (1999).
15. Qian, B. N., C. G. Gogos, "The Importance of Plastic Energy Dissipation (PED) to the Heating and Melting of Polymer Particulates in Intermeshing Co-Rotating Twin-Screw Extruders," *Adv. Polym. Tech.*, **19**, 287 (2000).
16. Chandrasekaran M., M. V. Karwe, "Measurement of Velocity Profiles in Reverse-Screw Elements of a Twin-Screw Extruder," *AIChE J.*, **43**, 2424 (1997).
17. Bravo V. L., A. N. Hrymak, J. D. Wright, "Numerical Simulation of Pressure and Velocity Profiles in Kneading Elements of a Co-Rotating Twin-Screw Extruder." *Polym. Eng. Sci.*, **40**, 525 (2000).
18. Sastrohartono, T., Y. Jaluria, M. V. Karwe, "Numerical Simulation of Fluid Flow and Heat Transfer in Twin-Screw Extruders for Non-Newtonian Materials," *Polym. Eng. Sci.*, **35**, 1213 (1995).
19. Chiruvella, R. V., Y. Jaluria, M. V. Karwe, V. Sernas, "Transport in a Twin-Screw Extruder for the Processing of Polymers," *Polym. Eng. Sci.*, **36**, 1531 (1996).
20. Lai, E., D. W. Yu, "Modeling of the Plasticating Process in a Single-Screw Extruder: A Fast Track Approach," *Polym. Eng. Sci.*, **40**, 1074 (2000).
21. Tenge, S., D. Mewes, "Experimental Investigation of the Energy Balance for the Metering Zone of a Twin Screw Extruder." *Polym. Eng. Sci.*, **40**, 277 (2000).
22. Potente, H., U. Melisch, "Theoretical and Experimental Investigations of the Melting of Pellets in Co-Rotating Twin-Screw Extruders." *Intern. Polymer Processing*, **11**, 101 (1996).
23. Potente, H., M. Bastian, "Polymer Blends in Co-Rotating Twin-Screw Extruders." *Intern. Polymer Processing*, **16**, 14 (2001).

24. Potente, H., M. Bastian, K. Bergemann, M. Senge, G. Scheel, T. Winkelmann, "Morphology of Polymer Blends in the Melting Section of Co-Rotating Twin Screw Extruders," *Polym. Eng. Sci.*, **41**, 222 (2001).
25. Han, C. D., K. Y. Lee, N. C. Wheeler, "An Experimental Study on Plasticating Single-Screw Extrusion," *Polym. Eng. Sci.*, **30**, 1557 (1990).
26. Van Krevelen, D.W., P. J. Hoftyzer, "Newtonian Shear Viscosity of Polymeric Melts," *Angew. Makromol. Chem.*, **52**, 101 (1976).
27. Incropera, F. P., D. P. DeWitt, *Introduction to Heat Transfer*, 3rd Ed., John Wiley & Sons Inc., New York (1996).
28. Churchill, S. W., M. Bernstein, "Correlating Equation for Forced Convection From Gases and Liquids to a Circular Cylinder in Cross Flow," *J. Heat Transfer*, **99**, 300 (1977).
29. Rao, B. K., "Heat Transfer to Non-Newtonian Flows Over a Cylinder in Cross Flow," *Int. J. Heat Fluid Flow*, **21**, 693 (2000).

Chapter 4

Rheology of polymer melt suspensions

4.1 Introduction

Heat transfer, including heat conduction from hot metal surface and heat convection from polymer melt, provides energy to melt polymers during blending. The driving force for the heat conduction in the partially filled region (see chapter 2) and heat convection studied in chapter 3 is temperature difference. However, the quick melting of polymers during processing cannot be achieved through this type of heat transfer alone. The mechanical energy input plays a critical role for melting as discussed in chapter 2. Heat can be generated inside and outside of solid polymer pellets through friction, plastic energy dissipation (PED), or viscous energy dissipation (VED). VED was one of the major mechanisms to convert mechanical energy into heat for melting, especially for concentrated polymer melt suspensions.

Investigation of polymer melting in processing was done to better understand morphology development along the extrusion channel (1~4). Initially, a lubrication flow starts in the extrusion channel after a polymer film forms between the hot barrel and solid polymer pellets. At the beginning of the fully filled region, a concentrated polymer melt suspension with spatially non-uniform distribution of solid polymer pellets is often formed (2, 5), and the temperature of the solid polymer pellets is usually close to their softening temperature. Therefore, deformation of the softened solid polymer pellets can

occur in the flow. The rheological properties of such suspensions are essential to understand polymer melt processing and the heat balance calculation during blending. The lack of data on the rheological properties of such suspensions slowed down the progress towards accurately modeling the melting process in blending equipment (5~7).

In this chapter, ethylene-acrylate copolymer (EAC) melt suspensions with spatially non-uniform distribution of solid polystyrene (PS) beads were used as the model system to study the rheological behavior of polymer mixtures in the initial stage of melting during extrusion. Two sample preparation methods were used: (1) solid PS beads or glass beads were layered between two EAC films to obtain sandwich suspension samples, and (2) cryo-ground EAC and PS beads were dry mixed and then compression molded to obtain a “homogeneous” sample. Temperatures were chosen above EAC melting temperature (T_m) and slightly below PS glass transition temperature (T_g) to capture the physical structure of the polymer mixture in the initial melting region of extrusion, and to study the effect of particle deformation on rheological properties.

4.2 Previous work

Rheological study of suspensions can be traced to the initial work of Einstein (8, 9), where he developed his famous equation

$$\eta_r = \frac{\eta}{\eta_0} = 1 + k\phi, \quad (4.1)$$

where η_r is the relative viscosity, η is the viscosity of the suspension, η_0 is the viscosity of the pure liquid, ϕ is the volume concentration of dispersed particles, and shape factor $k = 2.5$ for rigid spheres. This equation is valid only for infinitely dilute suspensions due to the simplifications made in the mathematical derivation. Since Einstein's work, the relation between the relative viscosity and the volume concentration has been studied extensively for application to non-dilute suspensions via experiments (10~13), or through theoretical derivation (14~20). Reviews of this research area are provided by Rutgers (21) and Krieger (22). Various equations have been developed to capture the relationship between the relative viscosity η_r and the volume concentration ϕ . Among them, three equations have been widely discussed. One is the Eilers equation (10):

$$\eta_r = \left[1 + \frac{1.25\phi}{1 - \phi/0.78} \right]^2, \quad (4.2)$$

another one is the Mooney equation (16):

$$\eta_r = \exp\left[\frac{2.5\phi}{1 - k\phi} \right], \quad (4.3)$$

where k is a constant, and the final one is the Krieger-Dougherty equation (20):

$$\eta_r = \left[1 - \frac{\phi}{\phi_m} \right]^{-[\eta]\phi_m} \quad (4.4)$$

where, ϕ_m is the volume concentration at maximum packing, and $[\eta]$ is the intrinsic viscosity.

However, rheological properties of suspensions are affected not only by the volume concentration, but also by particle size, particle size distribution, surface properties of the particles, and the distribution of particles in the fluid (23~28). For suspensions with nanometer size particles, bulk properties are governed by Brownian motion and colloidal particle-particle interactions, therefore, the viscosities of suspensions can be sensitive to particle surface chemistry (22, 29). For non-Brownian suspensions (particle size $> 10 \mu m$), the bulk viscosities are mainly determined by hydrodynamic interactions of neighboring spheres (30, 31). Aqueous solutions with glass bead and mineral particle have been widely used for the study of rheological behavior of suspensions partly because glass beads and mineral particle are rigid, easy to obtain, and do not swell or shrink after being immersed in a liquid (13, 15, 25, 27, 32~34). Other particles, such as synthetic polymer spheres (11, 22, 35~37), metal powders and aluminum oxide (38, 39), and coal (40) have also been used since suspensions have various applications.

Generally speaking, a suspension refers to a mixture of relatively rigid particles in a liquid, while emulsion refers to mixtures of one liquid in another liquid. Thus, a mixture of partially melted polymer drops dispersed in molten polymer is not a typical suspension of rigid particles, nor is it an emulsion of liquid droplets. The partially melted polymer drops can undergo large deformation during extrusions (1, 3).

Therefore, such a mixture is in a state between suspension and emulsion. Relatively few papers can be found on the study of rheological behavior of emulsions compared to the vast body of work on suspensions of solid particles. Comprehensive reviews of early studies of suspension rheology are provided by Sherman (41) and by Pal (42).

Equations or theories developed for suspensions of solid particles were widely applied to emulsions. The Einstein equation (8, 9) was extended by Taylor (43) for the case of liquid spheres. The following equation was derived,

$$\eta_r = 1 + \left[\frac{\eta_c + 2.5\eta_d}{\eta_c + \eta_d} \right] \phi \quad (4.5)$$

where, η_r is the relative viscosity, η_c is the viscosity of the continuous phase, η_d is the viscosity of the dispersed phase, and ϕ is the volume concentration. As in the case of the Einstein equation, the Taylor equation cannot be applied to finite concentration systems because of the significant hydrodynamic interaction between droplets. Two approaches developed for the rheological study of concentrated suspensions were also widely used in the field of concentrated emulsions: the so-called effective medium method (16, 18) and the cell model (19, 44, 45). According to the effective medium method, a concentrated suspension or emulsion can be obtained by successively adding small amounts of dispersed phase materials into the continuous phase. The equation for infinitely dilute suspensions or emulsions can be applied several times to derive the equation for concentrated systems. Some measured viscosity data and moduli fit well with the equations generated through the effective medium method using an adjusted dispersed phase volume concentration (13, 22, 46~51). However, this method does not include the effect of interaction between particles (or droplets) on the relative viscosity

of suspensions or emulsions, so it should not be used for systems with dispersed phase concentrations close to the maximum packing concentration.

According to the cell model, a concentrated suspension with spheres can be represented by a sphere surrounded by the continuous phase with a certain thickness, which is called “cell envelope”. The diameter of the cell envelope is calculated using the dispersed phase volume concentration, i.e. the envelope diameter decreases as the volume concentration increases. The cell model is an averaged approach, and suffers from the drawback that the results are strongly dependent on somewhat arbitrary choices of boundary conditions of the cell (52), and on the particle shape and size (44, 53).

For emulsions, there is a significant effect of shear rate on the relative viscosity. Pal and Rhodes (47) developed the following empirical equation to predict emulsion viscosity as a function of the volume fraction and shear rate:

$$\eta_r = \left[1 + \frac{0.8415\phi / (\phi)_{\eta_r=100}}{1 - 0.8415\phi / (\phi)_{\eta_r=100}} \right]^{2.5} \quad (4.6)$$

where, η_r is the relative viscosity, ϕ is the volume fraction, and $(\phi)_{\eta_r=100}$ is the volume fraction at which the relative viscosity becomes 100. The shear rate effect on viscosity was taken into account through the term $(\phi)_{\eta_r=100}$. This equation should not be used for concentrated emulsions at relatively high shear rate, when deformation of droplets is significant. Das et al. (54) experimentally investigated the influence of continuous phase viscosity, volume fraction, droplet size and temperature on concentrated emulsion viscosity at low shear rate. They found that the relative emulsion viscosity increased

linearly with volume fraction with constant size distribution, and pointed out that the effect of droplet size became more significant at higher volume fraction.

Compared with suspensions of rigid particles, concentrated emulsions show a moderately increasing viscosity with increasing volume fraction in shear flow according to numerical simulations (55). The alignment of deformed droplets in the flow direction reduced the rate of viscosity increase with volume fraction. Palieme (56) derived a linear viscoelastic constitutive equation for concentrated emulsions of incompressible viscoelastic materials in the presence of interfacial agents. Equations to calculate emulsion shear modulus as a function of shear modulus of the continuous phase and dispersed phase, droplet diameter, and the interfacial tension was developed for an infinitely dilute emulsion with spherical droplets. Using the rheological data of emulsions formed by mixing two polymer melts, Graebing et al. (57) used the Palieme model (56) to predict the interfacial tension between the two polymer melt phases.

As indicated in the discussion above, there are no general conclusions that can be drawn about rheological properties of concentrated suspensions or emulsions. Studies of rheological behavior of concentrated suspensions and emulsions are still refined on a case by case basis. More experimental and theoretical investigations are needed to have a better understanding of the rheological behavior of concentrated suspensions and emulsions.

4.3 Experimental

4.3.1 MATERIALS AND SAMPLE PREPARATION

A semi-crystalline polymer made in DuPont, ethylene-acrylate copolymer (EAC) with melting temperature, $T_m = 67\text{ }^{\circ}\text{C}$, was used as the matrix phase. An amorphous polymer, polystyrene (PS) with a glass transition temperature $T_g = 100\text{ }^{\circ}\text{C}$, was chosen as the dispersed phase.

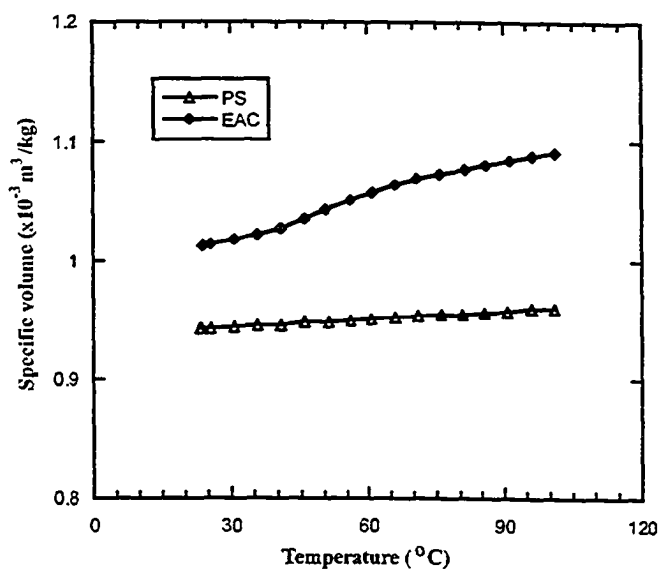


Figure 4.1 Relationship between specific volume and temperature for EAC and PS.

Figure 4.1 shows the relationship between specific volume and temperature for EAC and PS. The PS was obtained in the form of spherical beads. The size distribution of the PS beads was obtained by analyzing over 500 randomly selected beads using Mastersizer 2000 (Malvern Instruments Ltd.), and the result is shown in Figure 4.2. The volume weighted mean size is 0.5mm in diameter. For comparison, glass beads (GB) with diameter in 0.5mm were also used for this study. The glass transition temperature of GB is over $600\text{ }^{\circ}\text{C}$, and its specific volume is $0.4 \times 10^{-3}\text{ m}^3/\text{kg}$.

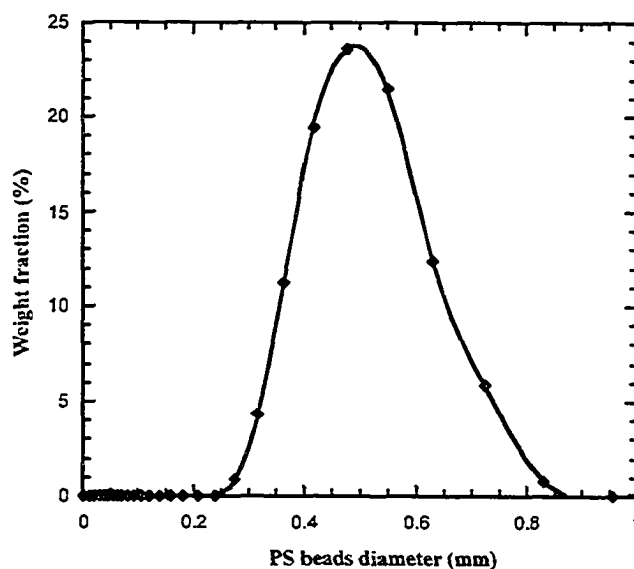


Figure 4.2 Size distribution of PS beads.

Two types of samples were made for the rheology measurement. One is a “sandwich” sample, and the other is a homogeneous sample. Each sample has a diameter of 40mm and thickness of around 2.6mm. To make the sandwich samples, we first prepared two EAC films by pressing EAC pellets at 80 °C in a mold with a diameter of 40mm. The weight of EAC pellets for each film was calculated based on the concentration of solid beads and the total weight of the sample. First one film was placed on the bottom of the mold; next the PS beads or GB were added, then the other EAC film was placed on top of the beads, and finally, the materials were pressed at 80°C with four tons pressure to make the sandwich sample. For the homogeneous samples, the EAC pellets were first cryo-ground in liquid nitrogen and a sieve was used to isolate particles with diameter around 0.5mm. A uniform solid mixture of the PS beads and the cryo-ground EAC particles was achieved by dry mixing them together

since they had a similar size and density. By pressing the uniform solid mixture in the mold at 80°C with four tons pressure, we obtained the homogeneous sample.

4.3.2 RHEOLOGICAL MEASUREMENT

A parallel plate rheometer, Advanced Polymer Analyzer (APA 2000, Alpha Technologies), was used for the measurement. The gap between the parallel plates without a sample is 2.2mm. Clamps were mounted on the parallel plates to prevent wall slip. One ton force was applied to the sample during testing. Comparison of viscosity data for polyethylene obtained from this rheometer and other rheometers verified that the clamps have no effect on the rheological measurement.

For EAC/PS samples, the measurement was carried out at three temperatures, viz., 70 °C, 80 °C, and 90 °C. For comparison, EAC/GB samples were tested only at 80°C. The temperatures were chosen so that EAC melt suspensions with solid PS beads are formed. Dynamic rheological tests were performed and this helped to keep the original structure of the samples. The frequency was swept from 10s⁻¹ to 100s⁻¹ under strain of 1%.

4.4 Results and discussion

4.4.1 VISCOSITY OF SUSPENSIONS

Figure 4.3 shows the relationship of the complex viscosity versus frequency at different temperatures for the sandwich sample EAC/PS suspensions. Using the Cox-Merz rule, which states that the complex viscosity versus frequency curve matches the steady shear viscosity versus shear rate curve, we are able to interpret the dynamic data as the relationship between viscosity and shear rate. Shear thinning behavior is observed for the pure EAC melt and for all sandwich suspension samples in the frequency range from 10 s^{-1} to 100 s^{-1} at all three temperatures.

Straight lines in the log-log plots in Figure 4.3 indicate that the power law model can describe the relationship between the complex viscosity and the frequency for the sandwich suspension samples. However, not all lines are exactly parallel to each other; therefore samples with different PS volume fraction may have different shear thinning behavior. The parameters of the power law model for each sample at different temperatures are summarized in Table 4.1.

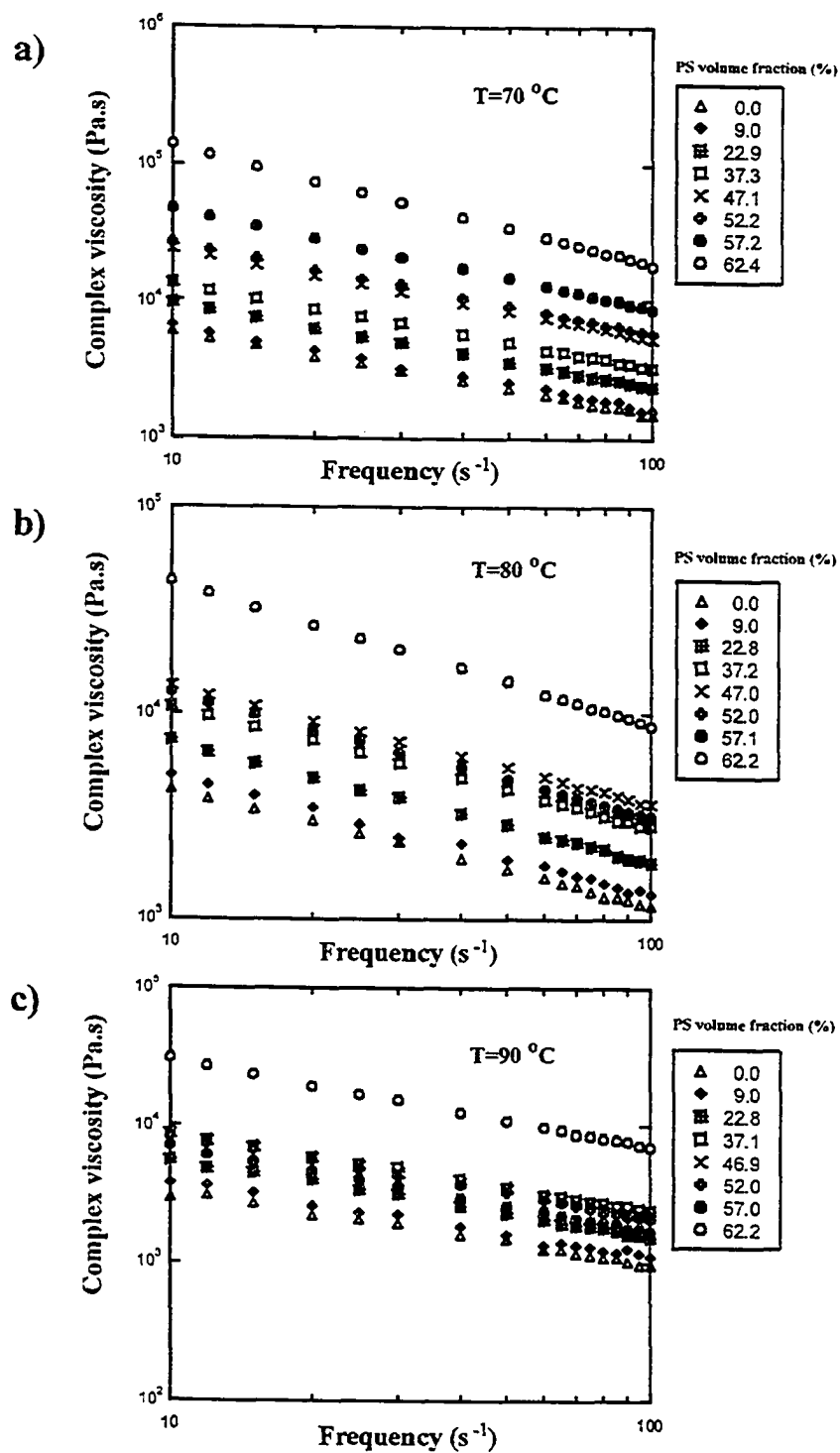


Figure 4.3 Complex viscosity versus frequency for the sandwich EAC/PS suspensions: a) 70°C; b) 80°C; c) 90°C.

Table 4.1 Data fitting using power law model, $\eta = \eta_0 \cdot \dot{\gamma}^{(n-1)}$, for sandwich EAC/PS suspensions

ϕ (vol%)	70 °C		80 °C		90 °C	
	η_0	n	η_0	n	η_0	n
0	23,800	0.40	15,900	0.44	10,900	0.48
9	26,200	0.40	18,500	0.43	13,500	0.46
23	39,200	0.39	27,900	0.42	21,000	0.44
37	55,100	0.38	42,200	0.41	31,900	0.44
47	104,300	0.36	50,700	0.42	33,400	0.42
52	122,700	0.34	50,000	0.40	34,500	0.39
57	246,900	0.28	50,700	0.39	29,800	0.38
62	1000,000	0.13	213,300	0.31	130,100	0.37

The degree of shear thinning decreased with increasing temperature for all sandwich samples as well as the pure EAC melt ($\phi = 0$). At each temperature, the shear thinning behavior was more pronounced with increasing volume fraction, especially at 70°C, since the power law index n decreased with the volume fraction. This result is consistent with earlier experimental measurement by Faulkner and Schmidt (58). The enhancement of shear thinning with the volume fraction could be caused by the higher shear rate generated in the flow between beads (59, 60).

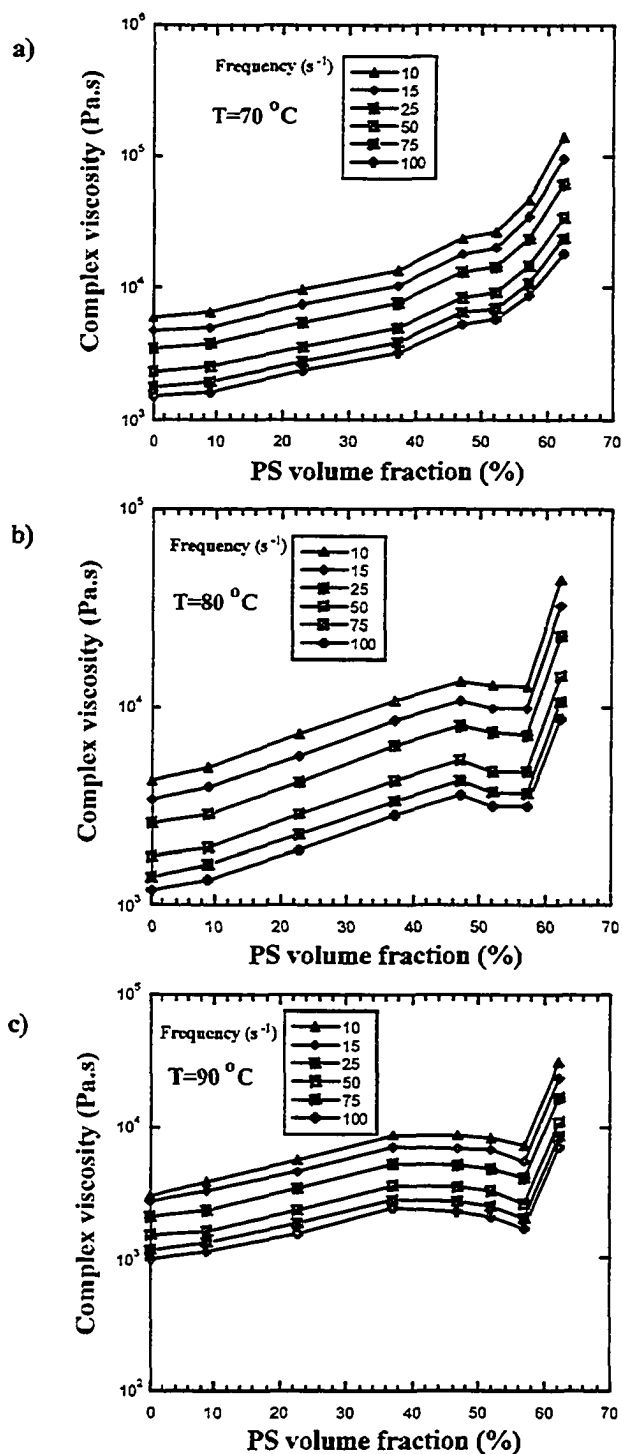


Figure 4.4 Complex viscosity versus volume fraction for the sandwich EAC/PS suspensions: a) 70°C ; b) 80°C ; c) 90°C .

Earlier studies of suspensions (15, 61) showed that at low and moderate concentrations, the viscosity was proportional to the volume fraction, and this was also

true for many emulsions before phase inversion occurred (10, 48). For the system studied here, the complex viscosity increased with the volume fraction at 70 °C. However, at 80°C and 90 °C, the complex viscosity increased with the volume fraction only when the volume fraction was below a critical value. Figure 4.4 shows the relationship between log of complex viscosity and volume fraction for the sandwich EAC/PS suspensions at the three temperatures. Lines corresponding to different frequencies at one temperature are parallel to each other. At 80°C, the complex viscosity at $\phi=47\%$ is greater than that at 52% and 57%; and at 90°C, the complex viscosity at $\phi=37\%$ is higher than that at 47%, 52%, and 57%. Volume increase was reported by Lee et al. (62) and Reiner (63) for plastic materials due to void generation during tensile testing, which could result in viscosity decrease. For our measurement, considering the force acting on the sample and the small (1%) strain during test, we believe volume increase cannot be the reason for the decrease of complex viscosity with volume fraction found for the EAC/PS sandwich suspensions.

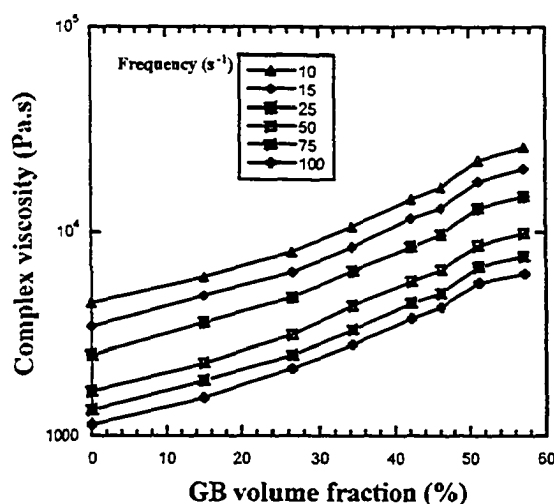


Figure 4.5 Complex viscosity versus volume fraction for the sandwich EAC/GB suspensions at 80 °C.

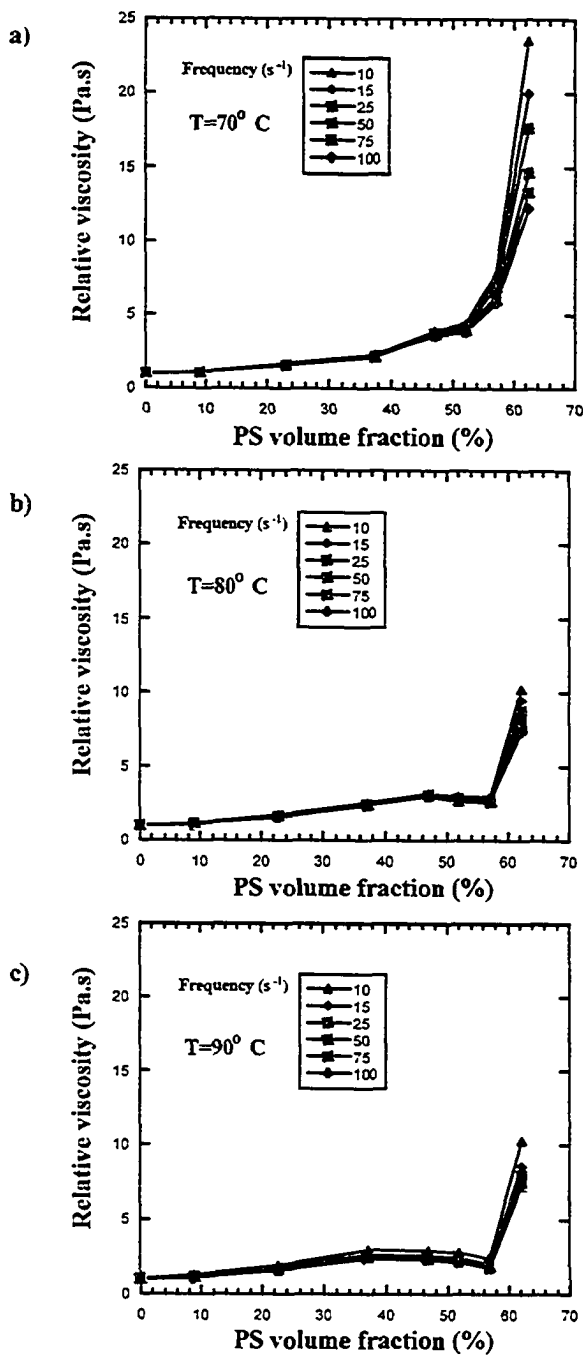


Figure 4.6 The relative viscosity versus volume fraction for the sandwich EAC/PS suspensions: a) 70°C; b) 80°C; c) 90°C.

Figure 4.5 shows the relationship between log of complex viscosity and volume fraction for the sandwich EAC/GB suspensions at 80°C. Due to experimental

difficulties, the maximum volume concentration of GB in EAC/GB samples we made was close to 60%. The complex viscosity increased monotonically with the volume fraction for the EAC/GB sandwich suspensions. At 80°C, GB is much more rigid than the PS beads since T_g of PS is at 100 °C. Deformation of PS beads under local shear stress in concentrated suspensions could contribute to the decrease of complex viscosity with the volume fraction found for the EAC/PS suspensions.

To eliminate the shear thinning effect of the suspending fluid (EAC), at different frequencies, we calculated the relative viscosity η_r . The results for the sandwich EAC/PS suspensions are given in Figure 4.6, and the sandwich EAC/GB suspensions in Figure 4.7.

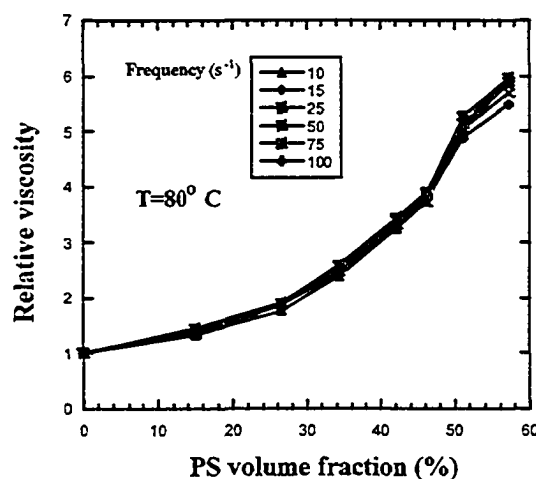


Figure 4.7 The relative viscosity versus volume fraction for the sandwich EAC/GB suspension at 80°C.

We can still see the decrease for the relative viscosity versus the volume fraction at high concentrations for the EAC/PS sandwich suspensions, but not for EAC/GB suspensions. Lines corresponding to different frequencies at one temperature overlap

for volume fraction below 47% for both systems, i.e. frequency did not affect the relationship between the relative viscosity and the volume fraction for dilute and medium concentration sandwich suspensions under the conditions studied here. Since the viscosity decreases more rapidly with increasing shear rate for concentrated suspensions than for dilute systems (60), the relative viscosity also decreased with frequency when the volume fraction is above 52%. The shear thinning behavior was more significant at high concentrations for lower temperatures. This could be clue to different amount of deformation of PS resulting from different local shear stress at different temperatures.

PS is an amorphous polymer. The three temperatures we chose are close to T_g of PS (100°C). At the lowest temperature 70°C, well below the T_g of PS, the PS beads were more rigid solid-like particles. Little deformation occurred even under high shear stress due to high local shear rate in the flow between PS beads. At a temperature of 90°C, PS beads became softer and were more likely to be deformed under shear stress. The deformation of PS beads at 90°C in concentrated suspensions reduced the velocity gradient in the flow between PS beads. This, in turn, reduced the local shear rate so that there was a more even stress distribution around the PS surfaces. A lower average shear rate was achieved for the deformed PS system than for the non-deformed systems under the same test conditions. Therefore, the concentrated PS suspensions show a stronger shear thinning behavior at lower temperature than at higher temperature.

Alignment or deformation of dispersed particles along the flow direction reduced the relative viscosity compared to rigid particles under the same conditions (20, 45, 55). Deformation of PS beads at high concentrations could also explain the

difference in the decrease of complex viscosity with volume fraction at the three temperatures. At 70°C, PS beads were so rigid that only small deformation was possible during testing even at high volume fractions. The relative viscosity had no change in the range of volume fraction from 47% to 57%. The viscosity increase due to increasing volume fraction in this range was balanced by the viscosity decrease due to small deformation of PS beads during shearing. A critical volume fraction, ϕ_d , can be defined for suspensions with deformable particles when the balance is reached. Obviously, ϕ_d is dependent on temperature. When temperature was increased, it was easier to deform the PS beads. The decrease of the relative viscosity due to deformation of PS beads along the flow direction counteracted the increase in relative viscosity with increasing volume fraction.

At higher temperatures, a lower volume fraction was required to generate enough local shear rate to cause deformation. This explains why the decrease of relative viscosity with volume fraction started at $\phi_d = 37\%$ for 90°C while for 80°C it started only at $\phi_d = 47\%$.

Deformation of PS beads was also inferred from the data of relative viscosity versus volume fraction at the same frequency. Figure 4.8 shows the relationship between the relative viscosity and the volume fraction for the sandwich EAC/PS suspensions at the lowest and highest frequencies used in this study. Temperature had no effect on the relative viscosity at volume fractions below 37%. As the volume fraction increased, the local shear rate increased, and this could cause deformation of PS beads in the flow. This process is demonstrated in Figure 4.9.

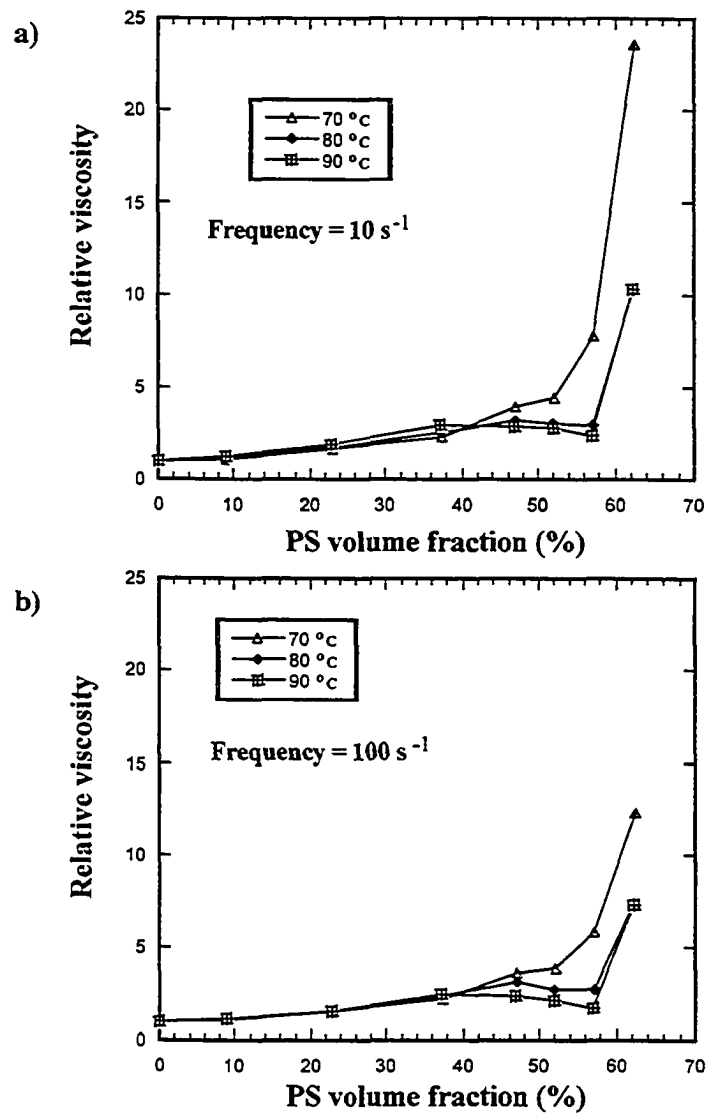


Figure 4.8 The relative viscosity versus volume fraction at constant frequency for the sandwich EAC/PS suspensions: a) 10 s^{-1} ; b) 100 s^{-1} .

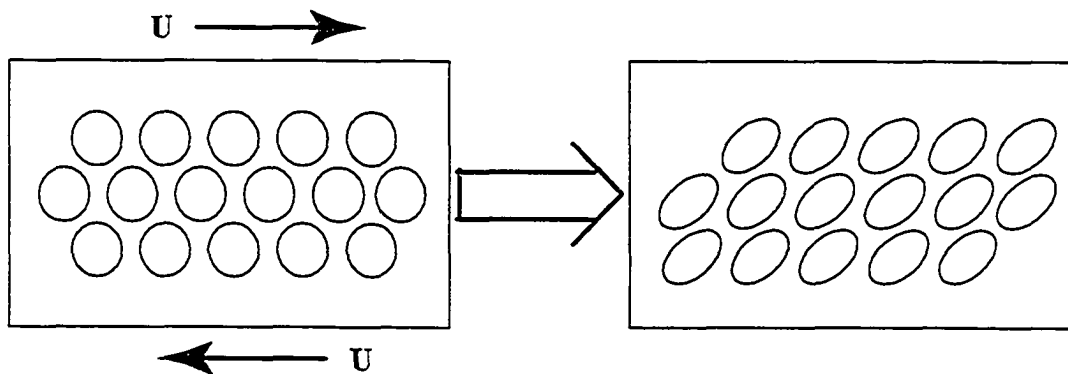


Figure 4.9 Deformation of PS beads under local shear stress.

The degree of PS beads deformation was determined by three major factors: packing factor of PS beads (gap between PS beads), modulus of PS beads (temperature dependent), and frequency during testing. With sufficient deformation of PS beads at higher concentrations, a decrease of the relative viscosity with volume fraction was found. The level of deformation of the PS beads at 70°C was probably too little to have any significant decrease in the relative viscosity. A viscosity plateau is seen for the curves at 70°C for both frequencies at volume fraction between 47% and 52%. The relative viscosity of the concentrated suspensions ($\phi > 47\%$) is always greater at 70°C than at 80°C and 90°C. At the lower frequency of 10s^{-1} , the PS beads seem to experience a similar degree of deformation at 80°C and 90°C in the flow. However, the two curves separate at the higher frequency of 100s^{-1} . Larger deformation of PS beads at 90°C caused an additional decrease of the relative viscosity with the volume fraction compared to that found at 80°C.

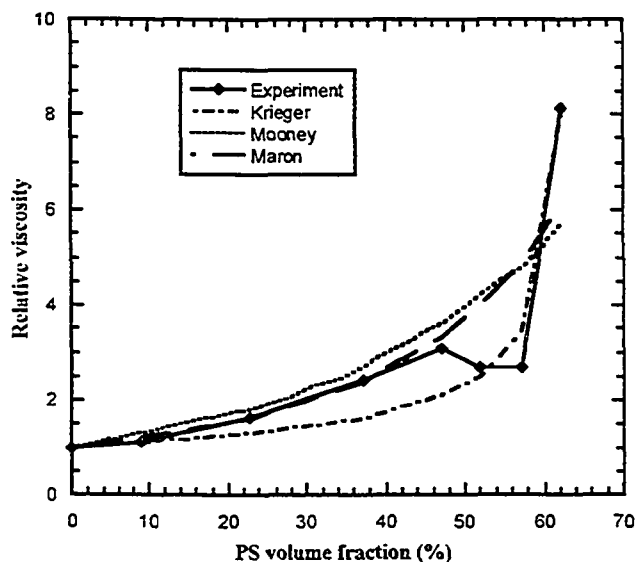


Figure 4.10 Experimental data fitting using well known equations.

In the introduction, we indicated that many equations have been developed to capture the relationship between the relative viscosity and the volume fraction. However, none of them are capable of predicting the decrease of relative viscosity with the volume fraction observed in the suspensions studied here. Taking the sandwich EAC/PS suspension experimental data at 80°C and frequency 50s⁻¹ as an example, three well known equations were used to fit the data using least squares regression and the results are shown in Figure 4.10. All the fitted lines fail to predict the decrease of relative viscosity with volume fraction at high concentrations. More parameters, such as shear modulus of the dispersed material, viscosity of the suspending fluid and the local shear rate information, are needed in these equations to capture the effect of deformation on the relative viscosity.

4.4.2 COMPLEX SHEAR MODULUS OF SUSPENSIONS

The complex shear modulus G^* is connected to the complex viscosity η^* through the following equation:

$$G^* = \eta^* \cdot \omega, \quad (4.8)$$

where ω is the frequency. The magnitude of the complex shear modulus, or shear modulus, can be calculated as:

$$|G^*| = \sqrt{G'^2 + G''^2}, \quad (4.9)$$

where G' is the elastic modulus, and G'' is the viscous modulus. Similar to the relative viscosity, the relative shear modulus, G_r , can be defined as follows:

$$G_r = \frac{|G_\phi^*|}{|G_0^*|}, \quad (4.10)$$

where $|G_\phi^*|$ is the shear modulus of suspensions, and $|G_0^*|$ is the shear modulus of the pure fluid. Since complex viscosity is linearly related to the shear modulus, the plot of relative shear modulus versus volume fraction looks identical to that of relative viscosity versus volume fraction as shown in Figure 4.6. Equations have been developed by Palierne (56) to predict complex shear modulus of emulsions in the linear viscoelastic region. For a dilute suspension of rigid spherical particles, the equation to calculate the relative complex shear modulus is:

$$|G_\phi^*| = 1 + 2.5\phi \quad (4.11)$$

Pal (51) extended this equation to concentrated suspensions using a strategy similar to the method proposed by Mooney (16). However, these equations also do not predict the decrease of shear modulus with the volume fraction observed in this study most probably because they do not incorporate particle deformation in the flow. More work is needed to quantify the effect of particle deformation in the flow on the relative viscosity or shear modulus of suspensions.

It was reported (58, 60) that both relative elastic modulus and relative viscous modulus increase with the volume fraction of rigid solid particles, and the increase of relative viscous modulus was greater than that of relative elastic modulus with increasing solid concentration. However, for the system studied here, the relative elastic modulus and the relative viscous modulus increased at the same rate with increasing volume fraction for each temperature. Taking the sandwich EAC/PS suspension data at

80 °C and frequency 50s^{-1} as an example, the relationships between relative viscous modulus with frequency and relative elastic modulus with frequency are shown in Figure 4.11. The increase of relative elastic modulus with volume fraction is the same as that for relative viscous modulus. The addition of PS beads into the EAC melt at the three temperatures did not change the comparative importance of elastic and viscous modules. This result also indicates that the PS beads were not rigid solid particles at temperatures close to the T_g of PS, therefore deformation of PS beads occurred during shearing.

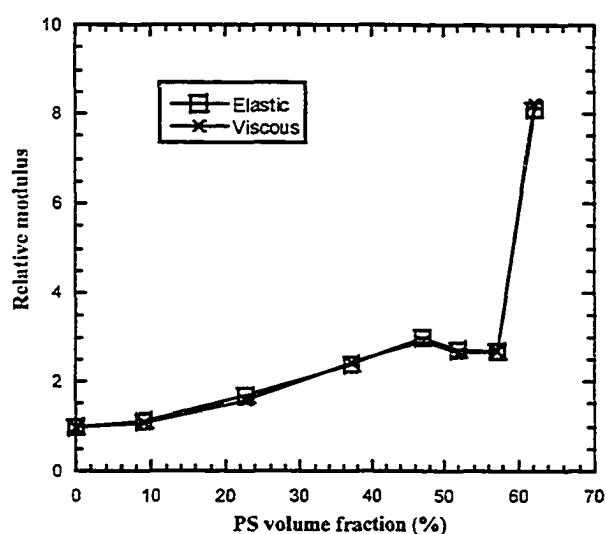


Figure 4.11 The relative elastic modulus and viscous modulus versus volume fraction at 80°C and frequency 50s^{-1} for the sandwich EAC/PS suspensions.

4.4.3 STRUCTURE EFFECT ON VISCOSITY

Sandwich structure samples and homogeneous sample were prepared and viscosity results were compared to each other. Due to experimental sample preparation difficulties, the maximum attainable concentration for the homogeneous sample was 57%. Comparisons were made only at 80°C . Figure 4.12 shows the relationship between

the relative viscosity and the volume fraction for the EAC/PS homogeneous and sandwich structure samples. Similar effects are seen for the homogeneous suspensions and the sandwich structure suspensions. For both sample types, the relative viscosity initially increased with the volume fraction followed by a decrease at volume fraction above 47%. However, the effect of frequency on the relative viscosity shows some differences for the two sample types. A significant shear thinning behavior is found for the homogeneous samples for $\phi > 37\%$, while only a small variation with frequency is seen for the sandwich samples.

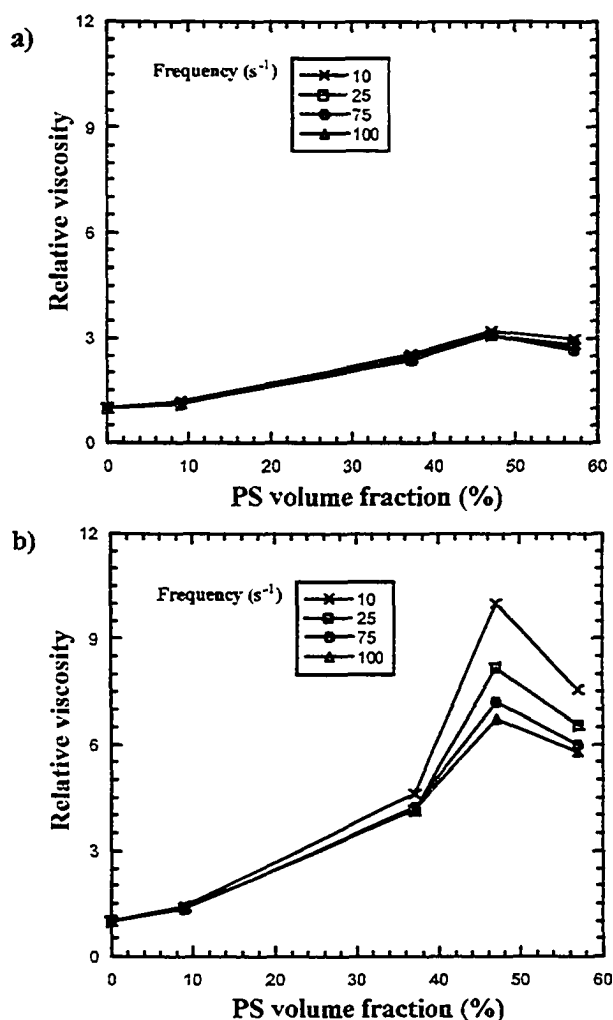


Figure 4.12 The relative viscosity versus volume fraction for EAC/PS suspensions at 80°C: a) sandwich; b) homogeneous.

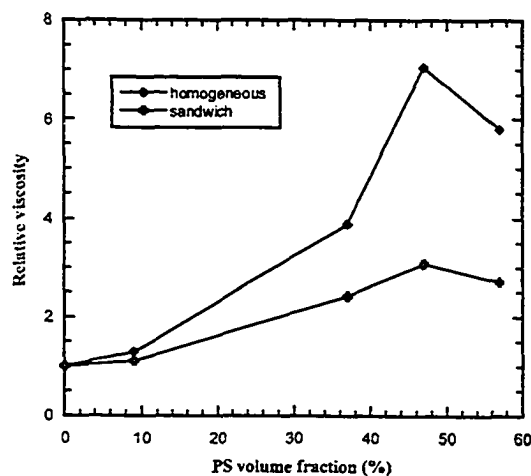


Figure 4.13 The relative viscosity versus volume fraction for the sandwich and homogeneous EAC/PS suspensions at 80°C and frequency 50s⁻¹.

To see difference between the sample types more clearly, we plot curves of relative viscosity versus volume fraction at one frequency (50s⁻¹) for the two sample structures in Figure 4.13. The relative viscosity of the sandwich sample was always lower than that of its corresponding homogeneous sample in the volume fraction range between 9% and 57%. For the sandwich structure suspensions, the PS beads were concentrated in the center of the samples (see Figure 4.14).



Figure 4.14 PS beads distribution in EAC/PS suspensions at $\phi = 47\%$: a) sandwich: b) homogeneous.

This non-uniform distribution of PS beads in the sandwich suspensions arbitrarily generated a significant wall effect, which resulted in a lower viscosity compared to the homogeneous suspensions (15, 64, 65). As ϕ approaches the maximum volume fraction, these two sample structures should have the same wall effect under the same flow conditions. Due to the difficulties in making homogeneous samples with higher volume fraction, we do not have data to validate this hypothesis.

4.5 Summary

A model system, EAC melt suspensions with PS beads, was used to investigate rheological properties of polymer mixtures during melting in polymer processing equipment. It was found that the power law model is capable of describing the relationship between viscosity and frequency in the range of 10s^{-1} and 100s^{-1} . The shear thinning behavior of these suspensions was enhanced at higher concentrations of PS beads. Shear thinning decreased as the PS beads were deformed. In the frequency range studied here, at a particular concentration the frequency had significant effect on the relative viscosity only for highly concentrated suspensions. The relative viscosity of the suspensions did not monotonically increase with volume fraction ϕ . A new phenomena occurred in these suspensions of deformable particles at a critical ϕ , ϕ_d , after which the relative viscosity decreased with ϕ . This decrease was followed by sudden increase in relative viscosity when ϕ was close to the typically observed critical maximum volume fraction ϕ_m . Deformation of PS beads along the flow direction in concentrated suspensions is postulated to be the reason for the observed decrease of relative viscosity with ϕ after ϕ_d .

Compared to homogeneous samples, a significant wall effect was present in the sandwich samples. The relative viscosity of the sandwich structure suspensions was always lower than that of the homogeneous suspensions when ϕ was below ϕ_m . New equations are needed to predict the relative viscosity of suspensions by taking into account the effect of deformation of the dispersed phase.

4.6 References

1. Gogos, C. C., Z. Tadmor, and M. H. Kim, "Melting Phenomena and Mechanisms in Polymer Processing Equipment," *Adv. Polym. Tech.*, **17**, 285 (1998).
2. Bawiskar, S., J. L. White, "A Composite Model for Solid Conveying, Melting, Pressure and Fill Factor Profiles in Modular Co-Rotating Twin Screw Extruders," *Inter. Polym. Process.*, **12**, 331 (1997).
3. Potente, H., and M. Bastian, "Polymer Blends in Co-Rotating Twin-Screw Extruders," *Intern. Polymer Process.*, **16**, 14 (2001).
4. Zhu, L., and X. Geng, "Experimental Investigation of Polymer Pellets Melting Mechanisms in Corotating Twin-Screw Extrusion," *Adv. Polym. Tech.*, **21**, 188 (2002).
5. Potente, H., and U. Melisch, "Theoretical and Experimental Investigations of the Melting of Pellets in Co-Rotating Twin-Screw Extruders," *Intern. Polym. Process.*, **2**, 101 (1996).
6. Todd, D. B., "Melting of plastics in kneading blocks," *Intern. Polym. Process.*, **8**, 113 (1993).
7. Vergnes, B., G. Souveton, M. L. Delacour, A. Ainsler, "Experimental and theoretical study of polymer melting in a co-rotating twin screw extruder," *Intern. Polym. Process.*, **16**, 351 (2001).
8. Einstein, A., "Eine neue Bestimmung der Moleküldimension," *Ann. Phys.*, (Leipzig) **19**, 289 (1906).
9. Einstein, A., "Berichtigung zu meiner Arbeit: Eine neue Bestimmung der Moleküldimension," *Ann. Phys.*, (Leipzig) **34**, 591 (1911).
10. Eilers, H., "Die Viskosität von Emulsionen hochviskoser Stoffe als Funktion der Konzentration," *Kolloid Z.*, **97**, 313 (1941).
11. Ward, S. G., and R. L. Whitmore, "Studies of the viscosity and sedimentation of suspensions Part I. The viscosity of suspension of spherical particles," *Brit. J. Appl. Phys.*, **1**, 286 (1950).
12. Williams, P. S., "Flow of concentrated suspensions," *J. Appl. Chem.*, **3**, 120 (1953).

13. Sweeny, K. H., and R. D. Geckler, "The rheology of suspensions," *J. Appl. Phys.*, **25**, 1135 (1954).
14. Vand, V., "Viscosity of solutions and suspensions. I Theory," *J. Phys. Colloid Chem.*, **52**, 277 (1948).
15. Vand, V., "Viscosity of solutions and suspensions. II Experimental determination of the viscosity-concentration function of spherical suspensions," *J. Phys. Colloid Chem.*, **52**, 300 (1948).
16. Mooney, M., "The viscosity of a concentrated suspension of spherical particles," *J. Colloid Sci.*, **6**, 162 (1951).
17. Simha, R., "A treatment of the viscosity of concentrated suspensions," *J. Appl. Phys.*, **23**, 1020 (1952).
18. Brinkman, H. C., "The viscosity of concentrated suspensions and solutions," *J. Chem. Phys.*, **20**, 571 (1952).
19. Happel, J., "Viscosity of suspensions of uniform spheres," *J. Appl. Phys.*, **28**, 1288 (1957).
20. Krieger, I. M., T. J. Dougherty, "A mechanism for non-Newtonian flow in suspensions of rigid spheres," *Trans. Soc. Rheol.*, **3**, 137 (1959).
21. Rutgers, I. R., "Relative viscosity and concentration," *Rheol. Acta*, **2**, 305 (1962).
22. Krieger, I. M., "Rheology of monodisperse latices," *Advan. Colloid Interface Sci.*, **3**, 111 (1972).
23. Brady, J. F., and G. Bossis, "The rheology of concentrated suspensions of spheres in simple shear flow by numerical simulation," *J. Fluid Mech.*, **155**, 105 (1985).
24. Brady, J. F., and J. F. Morris, "Microstructure of strongly sheared suspensions and its impact on rheology and diffusion," *J. Fluid Mech.*, **348**, 103 (1997).
25. Zarraga, I. E., D. A. Hill, and D. T. Leighton, "The characterization of the total stress of concentrated suspensions of non-colloidal spheres in Newtonian fluids," *J. Rheol.*, **44**, 185 (2000).
26. Singh A., and P. R. Nott, "Normal stresses and microstructure in bounded sheared suspension via Stokesian Dynamics simulations," *J. Fluid Mech.*, **412**, 279 (2000).

27. Amoros, J. L., V. Sanz, A. Gozalbo, and V. Beltran, "Viscosity of concentrated clay suspensions: effect of solids volume fraction, shear stress, and deflocculant content," *British Ceramic Transactions*, **101**, 185 (2002).
28. Matijasic, G., A. Glasnovic, "Influence of dispersed phase characteristics on rheological behavior of suspensions," *Chem. Biochem. Eng. Q.*, **16**, 165 (2002).
29. Russel, W. B., "Review of the Role of Colloidal Forces in the Rheology of Suspensions," *J. Rheol.*, **24**, 287 (1980).
30. Frankel, N. A., and A. Acrivos, "On the viscosity of a concentrated suspension of solid spheres," *Chem. Eng. Sci.*, **22**, 847 (1967).
31. Sierou, A., and J. F. Brady, "Rheology and microstructure in concentrated noncolloidal suspensions," *J. Rheol.*, **46**, 1031 (2002).
32. Chong, J. S., E. B. Christiansen, and A. D. Baer, "Rheology of concentrated suspensions," *J. Appl. Polym. Sci.*, **15**, 2007 (1971).
33. De Kruif, C. G., E. M. F. Van Lersel, A. Vrij, and W. B. Russel, "Hard sphere colloidal dispersions: Viscosity as a function of shear rate and volume fraction," *J. Chem. Phys.*, **83**, 4717 (1985).
34. Watanabe, H., M. Yao, K. Osaki, T. Shikata, H. Niwa, Y. Morishima, "Nonlinear rheology of concentrated spherical silica suspensions: 3. Concentration dependence," *Rheol. Acta*, **38**, 2 (1999).
35. Hoffman, R. L., "Discontinuous and Dilatant Viscosity Behavior in Concentrated Suspensions. I. Observation of a Flow Instability," *Trans. Soc. Rheol.*, **16**, 155 (1972).
36. Hoffman, R. L., "Discontinuous and Dilatant Viscosity Behavior in Concentrated Suspensions II. Theory and Experimental Tests," *J. Colloid Interface Sci.*, **46**, 491 (1974).
37. Rodriguez, B. E., E. W. Kaler, and M. S. Wolfe, "Binary mixtures of monodisperse latex dispersions. 2. Viscosity," *Langmuir*, **8**, 2382 (1992).
38. Bigg, D. M., "Rheological Behavior of Highly Filled Polymer Melts," *Polym. Eng. Sci.*, **23**, 206 (1983).
39. Zhou, Z., M. J. Solomon, P. J. Scales, and D. V. Boger, "The yield stress of concentrated flocculated suspensions of size distributed particles," *J. Rheol.*, **43**, 651 (1999).

40. Wildemuth, C. R., and M. C. Williams, "A new interpretation of viscosity and yield stress in dense slurries: coal and other irregular particles," *Rheol. Acta*, **24**, 75 (1985).
41. Sherman, P., "Rheological properties of emulsions," in *Encyclopedia of Emulsion Technology*, edited by P. Becher, Marcel Dekker, New York, Vol. 1, pp. 405 (1983).
42. Pal, R., "Rheology of Emulsions Containing Polymeric Liquids," in *Encyclopedia of Emulsion Technology*, edited by P. Becher, Marcel Dekker, New York, Vol. 4, pp. 93 (1996).
43. Taylor, G. I., "The viscosity of a fluid containing small drops of another fluid," *Proc. R. Soc. London, Ser. A* **138**, 41 (1932).
44. Yaron, I., and B. Gal-Or, "On viscous flow and effective viscosity of concentrated suspensions and emulsions," *Rheol. Acta*, **11**, 241 (1972).
45. Choi, S. J., and W. R. Schowalter, "Rheological properties of nondilute suspensions of deformable particles," *Phys. Fluids*, **18**, 420 (1975).
46. Pal, R., and E. Rhodes, "A novel viscosity correlation for non-Newtonian concentrated emulsions," *J. Colloid interface Sci.*, **107**, 301 (1985).
47. Pal, R., and E. Rhodes, "Viscosity/concentration relationships for emulsions," *J. Rheol.*, **33**, 1021 (1989).
48. Pal, R., "Shear viscosity behavior of emulsions of two immiscible liquids," *J. Colloid Interface Sci.*, **225**, 359 (2000).
49. Pal, R., "Novel viscosity equations for emulsions of two immiscible liquids," *J. Rheol.*, **45**, 509 (2001).
50. Pal, R., "Novel shear modulus equations for concentrated emulsions of two immiscible elastic liquid with interfacial tension," *J. Non-Newtonian Fluid Mech.*, **105**, 21 (2002).
51. Pal, R., "Complex Shear Modulus of Concentrated Suspensions of Solid Spherical Particles," *J. Colloid Interface Sci.*, **245**, 171 (2002).
52. Jeffrey, D. J., and A. Acrivos, "The rheological properties of suspensions of rigid particles," *AIChE. J.*, **22**, 417 (1976).
53. Adler, P. M., "Viscosity of concentrated suspensions of aggregable particles," *Rheol. Acta*, **17**, 288 (1978).

54. Das, A. K., D. Mukesh, V. Swayambunathan, D. D. Kotkar, and P. K. Ghosh, "Concentrated emulsions. 3. Studies on the influence of continuous-phase viscosity, volume fraction, droplet size, and temperature on emulsion viscosity," *Langmuir*, **8**, 2427 (1992).
55. Loewenberg, M., E. J. Hinch, "Numerical simulation of a concentrated emulsion in shear flow," *J. Fluid Mech.*, **321**, 395 (1996).
56. Paliarne, J. F., "Linear rheology of viscoelastic emulsions with interfacial tension," *Rheol. Acta*, **29**, 204 (1990).
57. Graebbling, D., R. Muller, J. F. Paliarne, "Linear viscoelastic behavior of some incompatible polymer blends in the melt. Interpretation of data with a model of emulsion of viscoelastic liquids," *Macromolecules*, **26**, 320 (1993).
58. Faulkner, D. L., and L. R. Schmidt, "Glass bead-filled polypropylene Part I: Rheological and mechanical properties," *Polym. Eng. Sci.*, **17**, 657 (1977).
59. Kataoka, T., T. Kitano, M. Sasahara, and K. Nishijima, "Viscosity of particle filled polymer melts," *Rheol. Acta*, **17**, 149 (1978).
60. Metzner, A. B., "Rheology of suspension in polymeric liquid," *J. Rheol.*, **29**, 739 (1985).
61. Thomas, D. G., "Transport characteristics of suspension: VIII. A note on the viscosity of Newtonian suspensions of uniform spherical particles," *J. Colloid Sci.*, **20**, 267 (1965).
62. Lee, A. R., M. Reiner, P. J. Rigden, "Volume flow of plastic materials," *Nature*, **158**, 706 (1946).
63. Reiner, M., P. J. Rigden, and E. N. Thrower, "The volume flow of asphalt." *J. Soc. Chem. Ind., London*, **69**, 257 (1950).
64. Barnes, H. A., "A review of the slip (wall depletion) of polymer solutions, emulsions and particle suspensions in viscometers: its cause, character, and cure," *J. Non-Newtonian Fluid Mech.*, **56**, 221 (1995).
65. Mooney, M., "Explicit formulas for slid and fluidity," *J. Rheol.*, **2**, 210 (1931).

Chapter 5

Polymer drop deformation and breakup in polymer blends*

5.1 Introduction

The study of melting in polymer blending covers the melting behavior of polymers (chapter 2), heat balance calculation during melting (chapter 3 and 4), and the morphology development during melting. Numerous studies have shown that performance of a polymer blend depends on properties of its component polymers and the final blend morphology (1~4). However, prediction of morphology development during polymer blending remains a big challenge in the polymer processing field mainly due to the poor understanding of the melting process and the complex viscoelastic properties of polymer melts. This chapter will focus on polymer drop deformation and breakup in polymer blends. Simulations and experiments are performed to understand the morphology development during blending.

The behavior of a Newtonian droplet deformation and breakup has been well established through a fundamental study by Taylor (5, 6) and other researchers (7, 8). It is well known that polymeric liquids are usually very non-Newtonian. Their behavior under even a simple shear flow may not follow the prediction by theories for Newtonian fluids (9~14). Numerical modeling is becoming a powerful tool to study the mechanisms of drop deformation and breakup especially considering the ever-

* Part of this chapter is published in paper:
Chen, H., U. Sundararaj, K. Nandakumar, *Polym. Eng. Sci.*, **44**, 1258 (2004)

increasing power of computers (15~19). Many useful data that cannot be obtained through experimental measurement, such as local shear rates, viscosity distribution, and local shear stress, can be easily accessed through numerical simulations (18~21). Several impressive experimental results have been reported recently on the fundamental study of polymer drop deformation and breakup under shear flow (9, 14). However, no satisfactory explanation has been given to data to those mechanisms observed in their experiments for polymer blends. Presumably, this is due to the complex properties of polymers and lack of detailed data about two phase flow.

Since the melting process in extruders is not fully understood, morphology prediction has been restricted to the molten state. Sundararaj et al. (22) showed that a sheeting mechanism was an effective way of dispersing the droplets at the initial stage of morphology generation. Willemse et al. (23) theoretically explained the rapid decrease of the sheet thickness under shear flow by using simplified equations. To model drop size in the molten state, one method is to divide the flow into different zones according to the local flow information (such as shear rate). Passage of flow through different zones was used to model the morphology development in batch mixers or extruders by many authors, such as Tadmor (24), Janssen and Meijer (25) DeRoussel et al. (26), Potente et al. (27), Delamare and Vergnes (28), and Huneault et al. (29). Another method is to simplify the boundary conditions for the flow in extruders by using unwound geometries. Two basic flows are generated in extruders; shear flow and extensional flow. Shi and Utracki (30) and Huneault et al. (29) used this method to study the morphology development in a twin-screw extruder by incorporating drop breakup and coalescence theories for generalized Newtonian fluids under shear flow.

However, a significant portion of the morphology development of polymer blends occurs during the melting process in extruders. Theories for liquid drop deformation and breakup under shear flow may not be applicable to polymer drops during melting.

In this chapter, the mechanism of deformation and breakup of polycarbonate (PC) drop in polyethylene (PE) was studied through on-line visualization of extrusion of PE/PC blend and numerical simulations using the volume of fluid (VOF) method in FIDAP 8.7 and FLUENT 6.0. The numerical simulations were based on the experimental setup used by Lin et al. (14). Only shear flow was involved in numerical simulations. Two-dimensional (2D) simulations were carried out for this study. The 2D simulations included two systems: one with a matrix phase/dispersed phase of PE/PE (initial temperature 190°C/25°C), and the other with PE/PC (initial temperature 220°C/210°C).

5.2 On-line visualization of PE/PC blending

The same 40mm twin screw extruder (TSE) as that described in section 2.2.1 was used for this study. The detailed description about the device used for the on-line visualization can be found in section 2.2.1 of this thesis. The sliding mechanism with a glass window fitted in the barrel was used to visualize the extrusion process on-line.

PE (Petromont DMDB-8907) and PC (GE LEXAN 140) were chosen for this study. Figure 5.1 shows the original shapes of the two types of pellets used in the extrusion. PE pellets are opaque and have a shape close to a sphere, while PC pellets are transparent and have a cylindrical shape. The specific heats of the two polymers were measured using a TA Instruments Model 2910 Differential Scanning Calorimeter (DSC), and Thermal Analyst 2200 software was to analyze the DSC data.

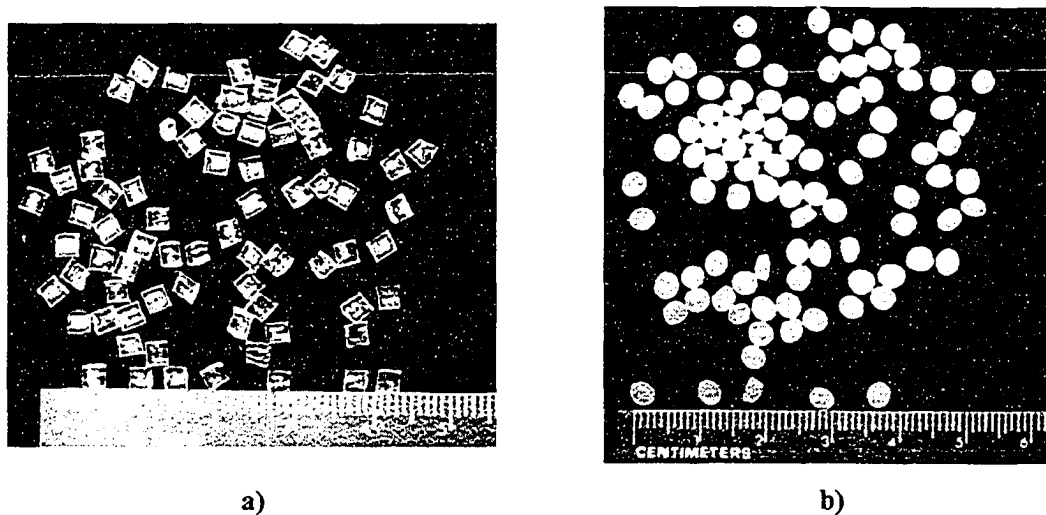


Figure 5.1 Original shapes of PE and PC pellets: a) PC; b) PE.

The heating rate was 20°C/min as recommended by the manufacturer. The glass transition temperature (T_g) of PC is around 150°C. The melting temperature (T_m) of PE is approximately 140°C.

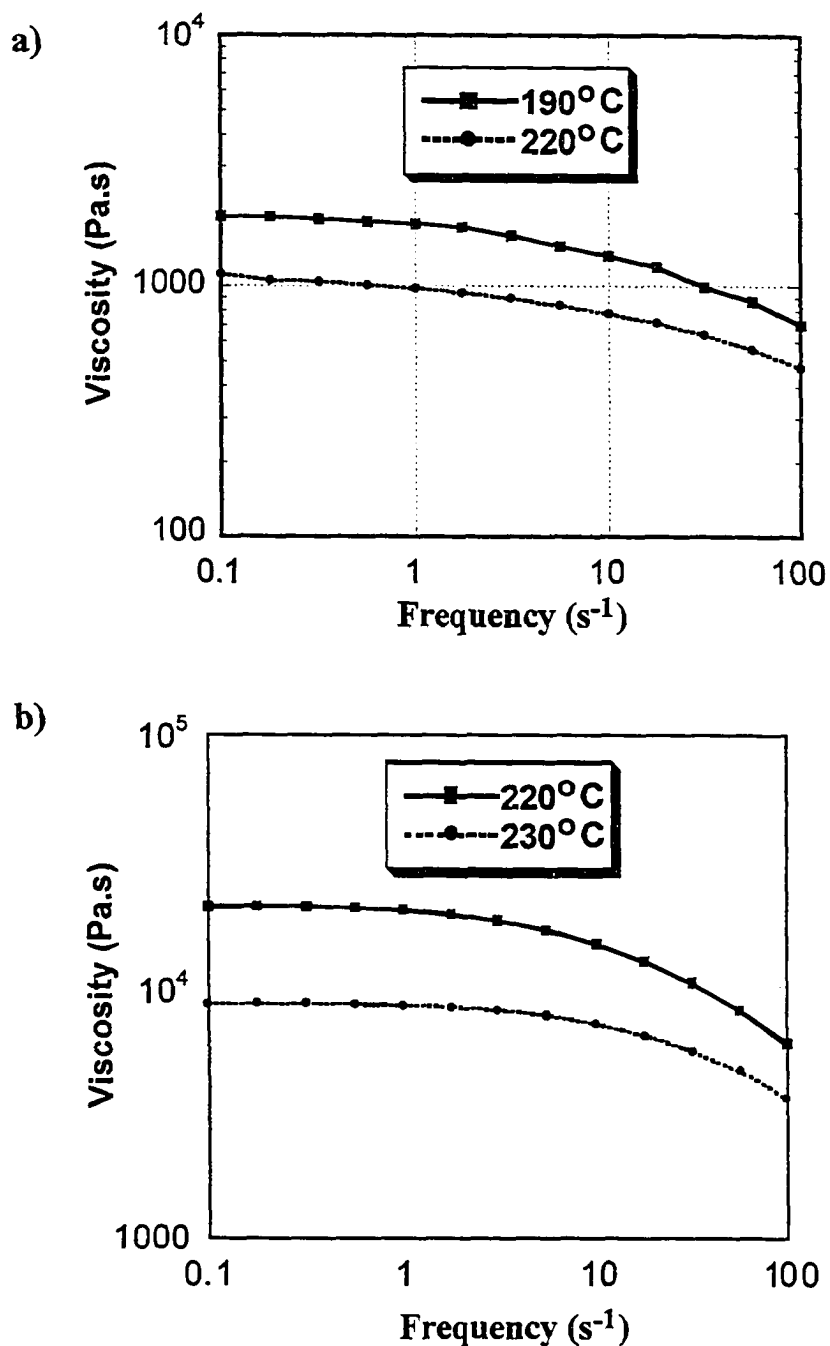


Figure 5.2 Dynamic viscosity versus frequency at different temperatures: a) PE; b) PC.

The dynamic rheological properties of PE and PC were determined using a Rheometrics RMS 800 rheometer with parallel plate fixtures, and the viscosity results are shown in Figure 5.2. On the basis of the Cox-Merz rule, which states that the complex viscosity versus frequency curve matches the steady shear viscosity versus shear rate curve, we used the dynamic data to model steady shear flow in our model. Figure 5.2a shows the variation of shear viscosity of PE with frequency at temperatures of 190°C and 220°C. Figure 5.2b shows the variation of shear viscosity with frequency for PC at temperature 220°C and 230°C. Shear thinning behavior can be seen over the frequency range for both PE and PC. The temperatures for barrels 1 to 9 were set as (°C): 50-50-150-150-160-220-230-250-250. The feeding material was composed of 90% PE and 10% PC. The steady state extrusion was operated at a total flow rate 22.7kg/hr and screw speed of 40rpm.

5.3 Numerical Modeling

5.3.1 MODEL GEOMETRIES

Two two-dimensional (2D) model geometries were built in this study: one to study PE and another to study PC drop deformation and breakup process in PE melt under shear flow.

Figure 5.3 shows the two 2D models for the PE/PE blend and the PE/PC blend. The boundary and initial conditions for both simulations are also shown in Figure 5.3.

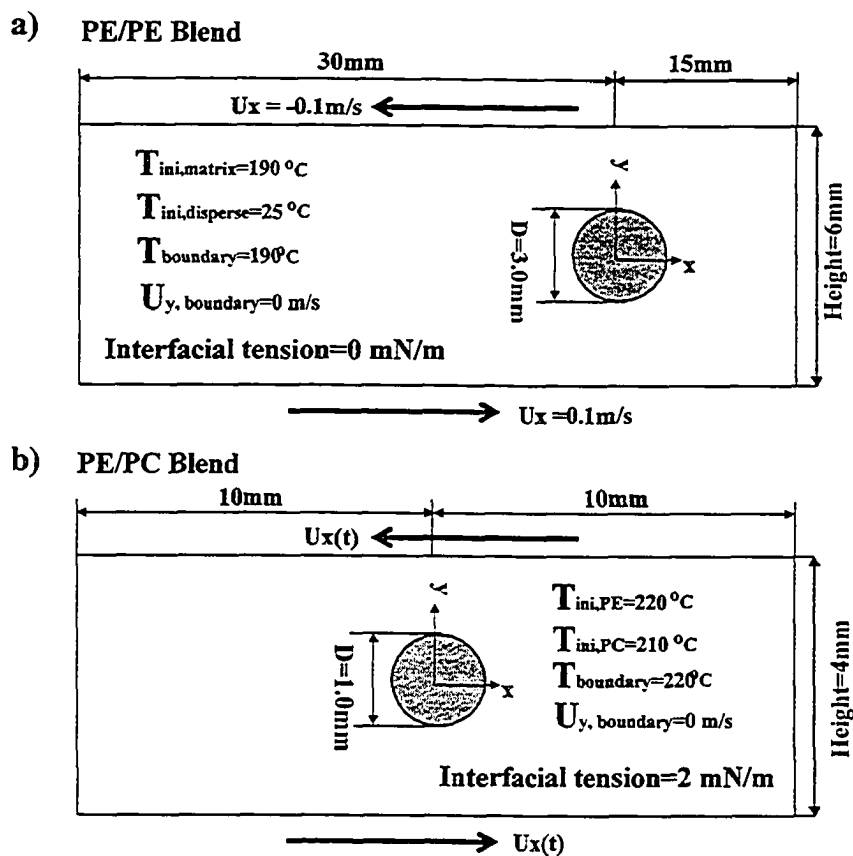


Figure 5.3 Simulation models, boundary and initial conditions: a) PE/PE blend; b) PE/PC blend.

The y-component velocities of the boundaries were set to zero. The top and bottom boundaries in Figure 5.3a moved with constant velocities (PE/PE blend), while time dependent moving boundaries were used for the PE/PC blend (Figure 5.3b). The

relationship between velocity $U_{x, 2D}$ and time, and the corresponding nominal shear rate and time for the PE/PC blend are shown in Figure 5.4. For the 2D simulations, we are really simulating the breakup of a cylinder in a matrix and looking at a cross-section. Our initial interests were to see if all the essential mechanisms of heat transfer, melting and deformation could be captured in a two-dimensional setting.

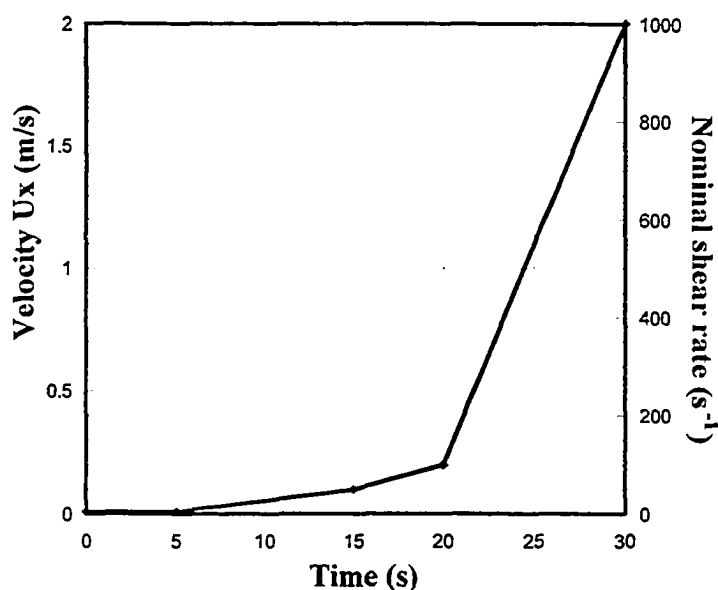


Figure 5.4 Velocity and nominal shear rate versus time for PC/PE blend.

5.3.2 MODEL EQUATIONS

The interface is tracked using the VOF method. The same set of equations is solved for the two phase problems using the local properties. The governing equations are:

Continuity equation:

$$\nabla \cdot V = 0 \quad (5.1)$$

where V is the velocity vector.

Momentum equation:

$$\rho\left(\frac{\partial V}{\partial t} + V \cdot \nabla V\right) = -\nabla P + \nabla \cdot \tau \quad (5.2)$$

where P is the pressure, ρ is the density, t is time, and τ , is the shear stress which is related to the rate of strain tensor, D through

$$\tau = 2\eta \cdot D \quad (5.2a)$$

Here η is the non-Newtonian viscosity. In equation (5.2) and (5.3), ρ and η are defined separately for each phase.

Energy equation:

$$\rho C_p \left(\frac{\partial T}{\partial t} + V \cdot \nabla T \right) = \nabla \cdot (k \nabla T) + \tau : \nabla V \quad (5.3)$$

For the 2D simulations, equations 1 to 3 were solved using finite element method (FEM) in FIDAP 8.6 with the segregated solver. The geometries were meshed with uniform sizes, 0.2mm for the PE/PE system, and 0.1mm for the PE/PC system. Since the drop size was 3.0mm for the PE/PE system, there were approximately 15 elements along the drop diameter, and since the diameter was 1.0mm for the PE/PC system, there were approximately 10 elements along the drop diameter.

5.3.3 VOF METHOD

The VOF method tracks the interface of two immiscible fluids through a marker concentration function F . The advection of F is governed by

$$\frac{\partial F}{\partial t} + V \cdot \nabla F = 0 \quad (5.4)$$

where t is the time, V is the velocity vector, governed by momentum and continuity equations. The two fluids are represented by the volume concentration function F

$$F = \begin{cases} 1 & \text{fluid 1} \\ 0 & \text{fluid 2} \end{cases} \quad (5.5)$$

The value of F varies between 0 and 1. Steep gradients in the marker concentration represent the interface location. Average properties are obtained through interpolation; for example density ρ is:

$$\rho = F\rho_1 + (1-F)\rho_2 \quad (5.6)$$

Other properties, such as viscosity η , specific heat capacity C_p , and thermal conductivity k , are calculated in the same way. It is well known that the VOF method conserves mass and still maintains a good representation of the interface (15, 31).

5.3.4 MATERIAL PROPERTIES

The same PE and PC as those used for the on-line visualization were chosen for the simulations. Since polymers have thermodynamic transitions over a range of temperatures, not at one specific temperature, we approximated the enthalpy change due to melting for PE using the specific heat curve (i.e. the specific heat can be integrated over the melting temperature range to obtain the enthalpy change due to fusion).

Shear thinning behavior can be seen over the frequency range for PE at temperatures of 190°C and 220°C, although the effect is not significant (see Figure 5.2a). The dispersed PE in the PE/PE blend simulation experienced a wide range of temperature change, starting from 25°C at the beginning of the run to over 190°C at the

end. Compared to the shear rate, the temperature dominates the changes in viscosity of PE. Therefore, we used a temperature only dependent viscosity model for PE in the simulation of PE/PE blend. A correlation proposed by Van Krevelen and Hoftzyer (32) is used to generate the viscosity data of PE at temperatures above its melting point. A large value ($\sim 10^6 \text{ Pa}\cdot\text{s}$) was set for the viscosity of PE at temperatures below its melting point to approximate solid behavior. Figure 5.5 shows the relationship of PE viscosity with temperature used in the simulation of PE/PE blend.

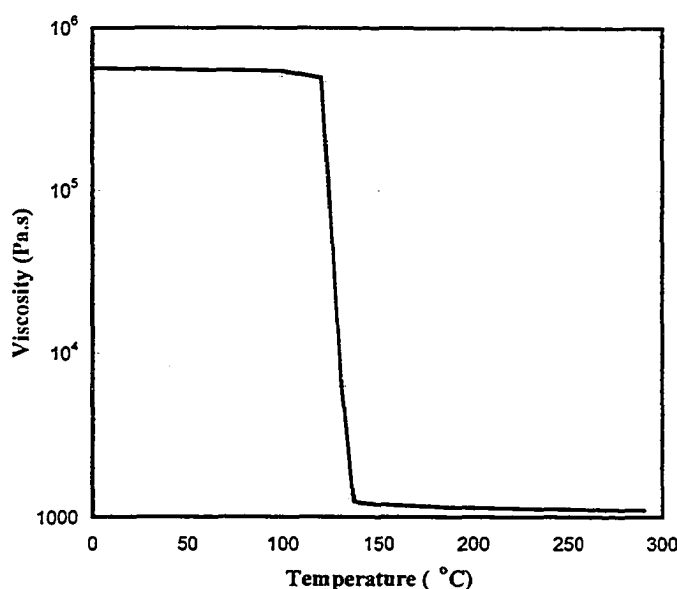


Figure 5.5 Dynamic viscosity of PE versus temperature. This relation was used in simulation of the PE/PE blend.

For the simulation of PE/PC blend, the PE is the matrix phase, and the initial temperature difference between the matrix phase PE and the dispersed phase PC is only 10°C . Here, compared to the temperature effect on viscosity, the shear thinning effect cannot be neglected. Therefore, we used a generalized Newtonian viscosity model for the PE in the simulation of PE/PC blend to include the shear thinning effect. The model for the PE was based on data from our rheological measurement for PE melt at two

temperatures (Figure 5.2a). The correlation from reference 32 is used to generate the viscosity data of PE at other temperatures in the simulation. The viscosity of PE in the PE/PC simulation at different temperature and shear rate was calculated using the following equations.

$$\eta = \begin{cases} 0.37 \cdot \exp(3900/T) \cdot \dot{\gamma}^{(0.84-1)} & \dot{\gamma} \geq 1.0s^{-1} \\ 0.37 \cdot \exp(3900/T) & \dot{\gamma} < 1.0s^{-1} \end{cases} \quad (5.7)$$

where $\dot{\gamma}$ is the shear rate, and T is the temperature in K .

Figure 5.2b shows the variation of shear viscosity with frequency for PC at temperature 220°C and 230°C. The same correlation structure (32) was used to obtain the viscosity of PC at other temperatures in the simulation. A generalized Newtonian viscosity model was derived and used for PC in the simulation of PE/PC blend. The equation is shown below:

$$\eta = \begin{cases} 1.59 \times 10^{-15} \cdot \exp(22000/T) \cdot \dot{\gamma}^{(0.66-1)} & \dot{\gamma} \geq 10s^{-1} \\ 1.59 \times 10^{-15} \cdot \exp(22000/T) & \dot{\gamma} < 10s^{-1} \end{cases} \quad (5.8)$$

where $\dot{\gamma}$ is the shear rate, and T is temperature in K . Constant thermal conductivities were used for PE and PC. Table 5.1 summarizes the properties of PE and PC used in the 2D simulations.

Table 5.1 Properties of PE and PC used in modeling

Material	ρ (kg/m^3)	C_p ($J/kg \cdot ^\circ C$)	k ($W/m \cdot ^\circ C$)	η ($Pa \cdot s$)
PE	954	1520 (25°C) 2120 (190°C)	0.182	Figure 5.4 for PE/PE blend Equation 5.7 for PE/PC blend
PC	1200	1750 (210°C) 1780 (220°C)	0.24	Equation 5.8

5.4 Results and discussion

5.4.1 ON-LINE VISUALIZATION OF PE/PC BLENDING

Our major interest is to see how PC drops deform and breakup in PE melt under complex flow in TSE. Therefore, the barrel temperatures in the conveying zone (from barrel 3 to 7) were set higher than the melting temperature of PE (140°C) and sequentially increased to approach the flowing temperature of PC (230°C). A PE melt suspension with PC drops would be formed when the flow reached the kneading section of the TSE.

Figure 5.6 shows the flow on-line visualization results of PE/PC blending process in the TSE. The definition of X can be found in Figure 2.5 in chapter 2. Since most PE already melted at X=110mm, a dilute PE melt suspension with PC pellets was formed at X= 150mm. Most PC pellets in the picture at X=150mm still kept their original cylindrical shape. However, whitening of some PC pellets on their surfaces is shown in this picture. PC pellets that are surrounded with a cloud of PC melt can be identified. The softened outer layer of PC pellets was stretched and peeled off from the pellets in the flow. The “erosion” mechanism (14) is shown for some PC pellets, which means the out layer of PC pellets was softened, stretched and peeled off from the pellets under the complex flow (Figure 5.6 at X=150mm). This erosion mechanism continued to dominate PC pellets deformation and breakup in the following kneading section of the TSE (see Figure 5.6 from X=170 to 290mm). Stretched ribbons are found for many PC pellets in the PE flow. Through this erosion mechanism, the size of PC pellets was reduced, and the shape of PC pellets was changed from cylinder to sphere. As more PC

dispersed into the PE matrix under complex flow in the kneading section, the flow became more milky, and a relatively more uniform flow was reached at $X=310\text{mm}$.

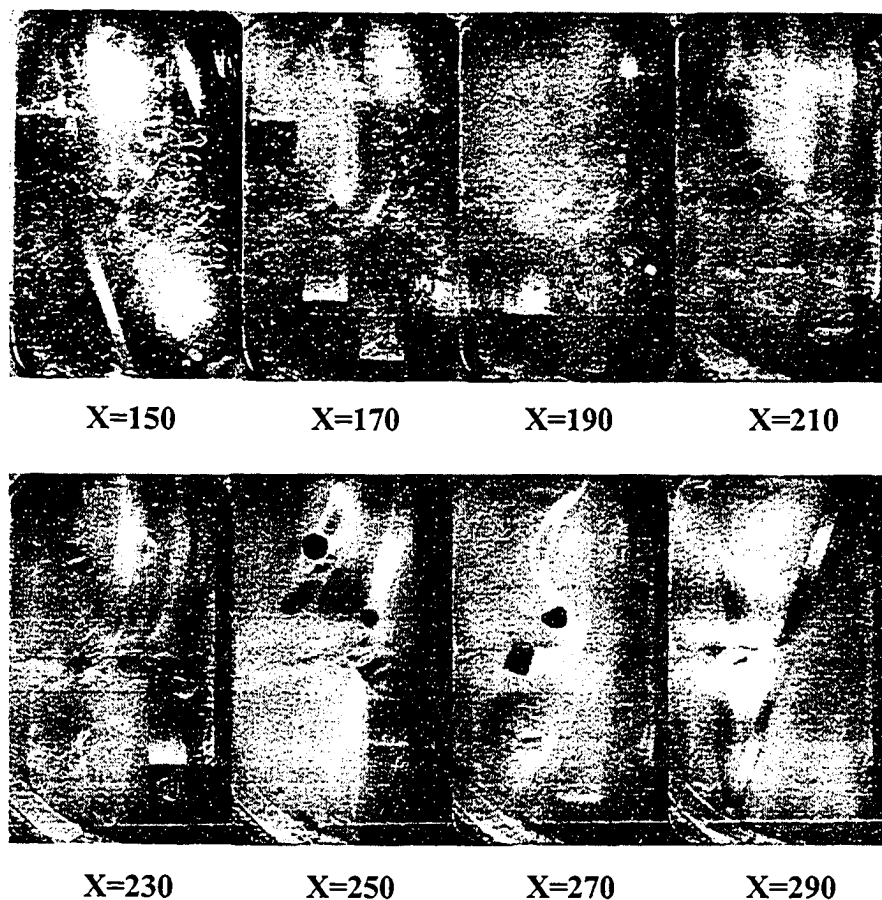


Figure 5.6 On-line visualization of PE/PC blending in TSE (“erosion” of some PC pellets in pictures at $X=250$ and $X=270$ is highlighted, refer to Figure 2.5 for the definition of X , in the unit of mm).

5.4.2 MODELING OF PE/PE Blend

In this simulation, we wanted to model the melting of a PE pellet in a PE melt. Therefore, for initial conditions, we chose a low temperature (25°C) for the pellet and a high temperature (190°C) for the melt. This simulation could correspond to the case of solid pellets side-fed into an extruder at a location where melt was present. Figure 5.7

shows deformation and breakup of a solid PE pellet in PE melt subjected to simple shear flow at different times, and Figure 5.7 also shows the corresponding temperature contours.

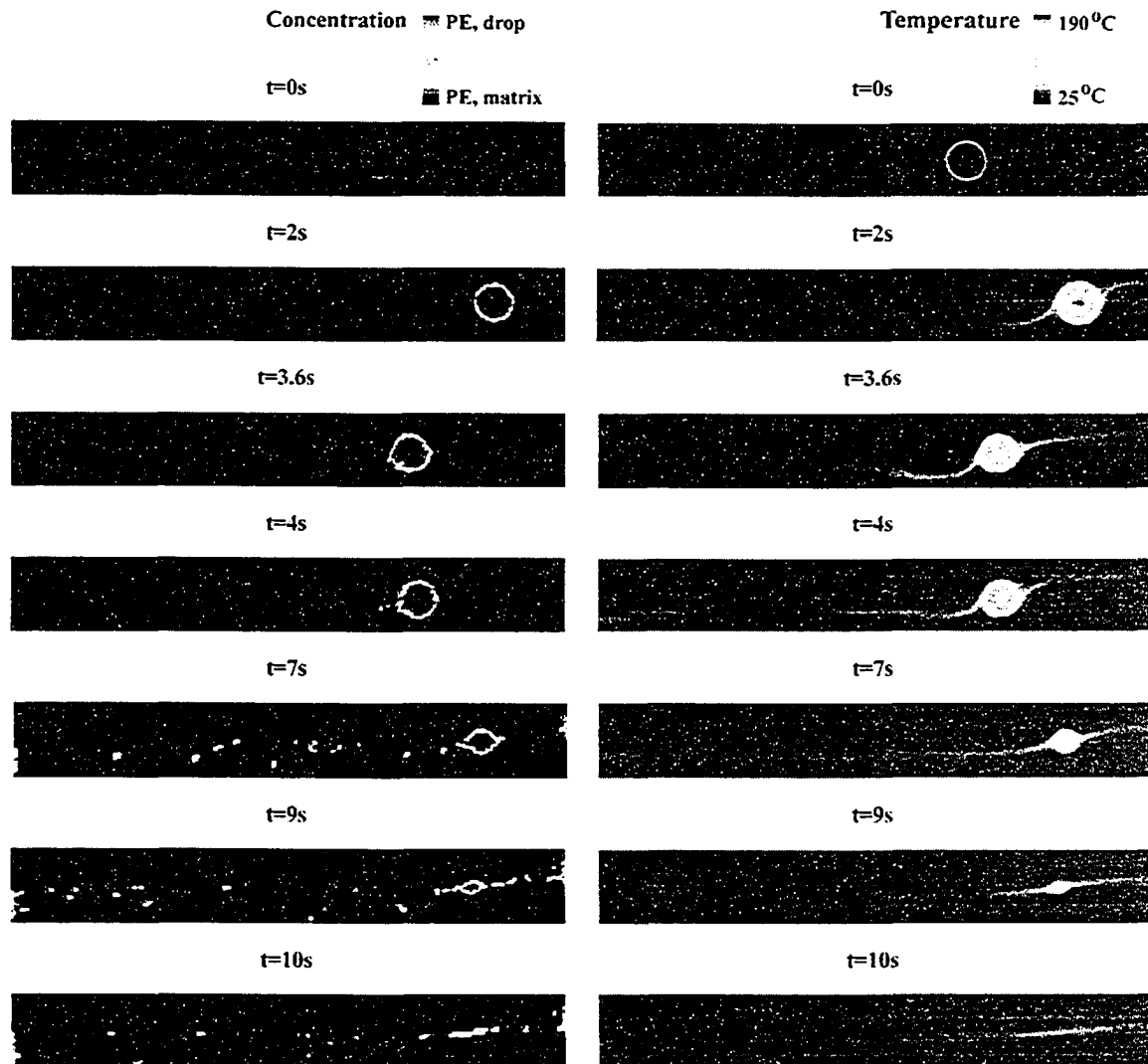


Figure 5.7 Deformation and breakup mechanism of PE drop in PE melt under shear flow at different times and corresponding temperature contours.

The initial temperatures for the dispersed PE and the matrix PE are shown in Figure 5.3a. Constant velocities ($U_x=0.1\text{m/s}$) were used for the top and the bottom

plate to generate the shear flow. The fluid velocity was initially zero and was driven by the opposite movement of the top and bottom plates. No steady state was achieved for the flow before the PE drop completely broke. However, some variables, such as velocity in the region far from the PE drop, had little variation after a certain time. According to the simulation results, it took less than 0.02 seconds for the matrix PE to reach a pseudo steady state in terms of velocity profile. During the first 3.6 seconds, the PE drop did not breakup in any way. The PE drop rotated as a solid particle under the shear flow. Small deformation can be observed on the surface of the PE drop. Heat convection outside the PE drop and heat conduction in the PE drop are clearly shown in the temperature contours in Figure 5.7.

The core of the PE drop was still cold before time of 3.6 seconds. In a previous paper, we were able to show that the temperature rise in a cold solid polymer pellet in a hot melt could be modeled accurately using the transport equations (33). In that case, a thermocouple was inserted into the cold pellet to experimentally determine the temperature rise with time. Though this cannot be done for the case of a melting drop that is studied here, we have confidence in the heat transfer results based on the earlier study. As more heat was transferred to the PE drop, the drop surface reached the T_m of PE, and resulted in a sharp decrease of the viscosity of the surface layer. Then at time of 3.6 seconds, the newly melted PE on the surface underwent a large local deformation under shear flow. The deformation on the surface grew larger with time as more heat was transferred to the PE drop and the surface layer viscosity decreased further. The deformation was large enough that a piece of PE broke off from the surface of the PE drop at time of 4 seconds.

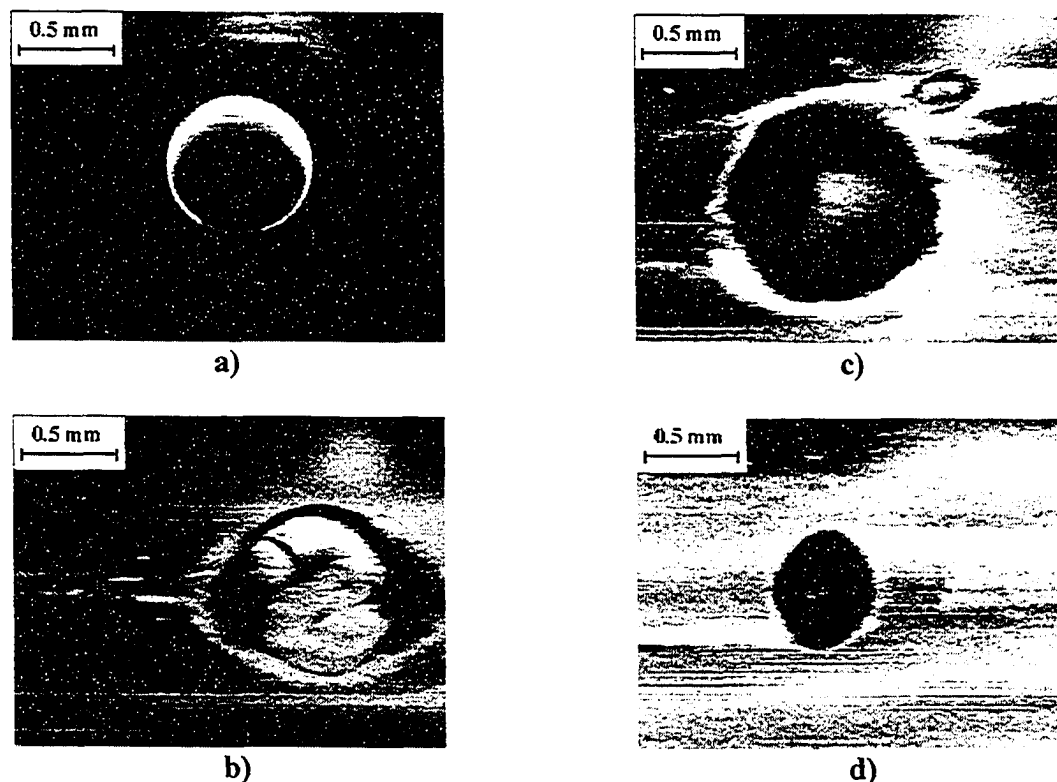


Figure 5.8 PC drop deformation and erosion in PE matrix at nominal shear rate 1.2 s^{-1} and viscosity ratio of 9: a) $t=0\text{s}$ (no deformation); b) $t=1632\text{s}$; c) $t=1747\text{s}$; d) $t=2356\text{s}$ (Lin et al, 2003).

The simulated breakup phenomenon is similar as that observed by Lin et al. (14) in their experiment with a PE/PC system (Figure 5.8). The outer layer of PC pellet was softened first, stretched under the shear flow, and finally peeled off from the mother PC pellet. This breakup mechanism was called “erosion”. The same simulation for the PE/PE system was also carried out using FLUENT 6.0 (Fluent Inc.) with VOF. Unlike FIDAP 8.6, where the finite element method is used, in FLUENT 6.0, the finite volume method is incorporated. Simulation results from FLUENT 6.0 also show the same erosion mechanism of the PE drop breakup as that seen in Figure 5.7. More PE pieces were peeled off from the PE drop through this erosion mechanism as the cold region of the PE drop shrank gradually through “erosion” of the drop surface under shear flow (Figure 5.7). The whole PE drop melted and was dispersed into the PE matrix in about 10 seconds.

Interfacial tension was not included in this simulation since both dispersed phase and matrix phase are PE. In reality, these simulation results represent the melting process of a solid polymer drop in its own melt under shear flow. However, it is very hard to compare the simulation to a corresponding experiment because of the difficulty of tracking the dispersed PE after it melts in the experiment. According to the simulation, the whole melting process took about 10 seconds to finish, which provides us with an important parameter that can be used for the comparison with polymer processing experiments, and potentially in design of polymer processes.

5.4.3 MODELING OF PE/PC Blend

Unlike the PE/PE blend, time dependent boundary velocities were used for the 2D simulation of PE/PC blend; thus the shear rate changed with time. The interfacial tension was set as 0.002 N/m for the PE/PC system (34), and the initial temperature difference between the melt and the drop was 10°C . The temperatures were chosen so that the simulation would correspond closely to the conditions used in the visualization experiments shown in Figure 5.8. Their initial temperatures are much higher than either T_m of PE or T_g of PC. Thus, the PC should be deformed inside the PE melt. Figure 5.9 shows the PC drop deformation process in a PE melt under shear flow during the first 8 seconds. The corresponding temperature contours are also shown in Figure 5.9. The temperature difference between the melt and the drop disappeared very quickly. After 8 seconds, a uniform temperature was obtained, so no further temperature contours are shown. The PC drop rotated and underwent small deformation on the surface under shear

flow. Each time the plate velocity was increased, the rotation rate of the PC drop increased.

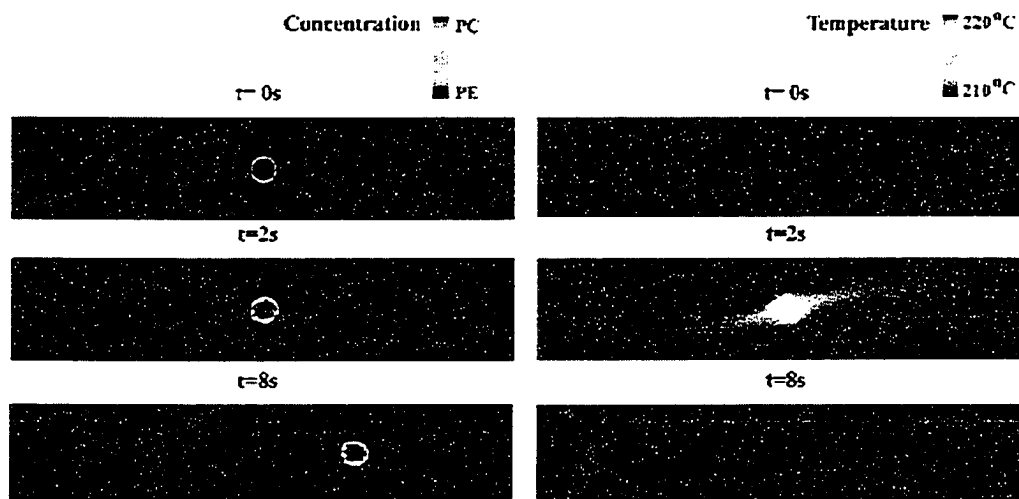


Figure 5.9 Deformation and breakup mechanism of PC drop in PE melt under shear flow for $t < 8s$ and corresponding temperature contours.

There was no breakup of the PC drop until a time of 21.7 seconds. The PC drop breakup process from time of 21.7s to 22.9s is shown in Figure 5.10. At time of 21.7 seconds, a large local deformation on the surface of the PC drop can be found (Figure 5.10, at $t=21.7s$), followed by the breaking off of a small piece of PC from the mother PC drop at time of 21.8s (Figure 5.10, at $t=21.8s$). Then, more pieces of PC were similarly peeled off of the PC drop under shear flow. The simulation shows a breakup mechanism that is similar to that observed in the experiment (see Figure 5.8 and ref. 14) and to that seen in the simulation for PE/PE system (Figure 5.7). The velocity of each plate at time of 21.7s is $0.50 m/s$, and the nominal critical shear rate in the flow is $250 s^{-1}$ (obtained from $\Delta U_x / height$). A higher shear rate was required to break up the remaining PC particle. The simulation is qualitatively similar to the experimental result published by Lin et al (14); however, there are some key differences, such as the time and the critical

shear rate for breakup. The differences in the observed time and critical shear rate for breakup could be due to differences in rheological properties; in particular, omission of viscoelastic effects in the simulation.

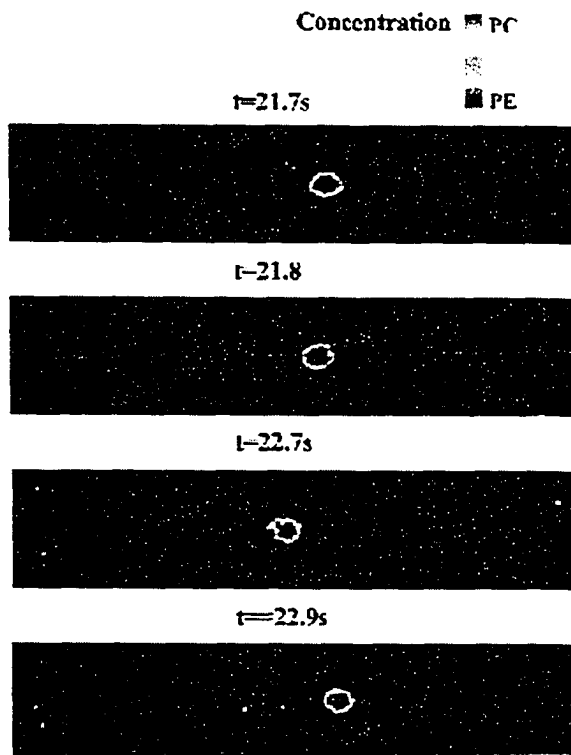


Figure 5.10 Deformation and breakup mechanism of PC drop in PE melt under shear flow for $t=21.7\sim 22.9$ s.

Since the breakup begins at 21.7 seconds, simulation results at this time were examined in more detail to better understand the deformation and breakup process of a PC drop in PE melt under shear flow. A cross-section from the bottom boundary to the top boundary, A-B, which crosses the center of the PC drop, was chosen for the analysis. The position of the cross section is shown in Figure 5.11a. Variables, such as volume concentration, temperature, shear rate, and viscosity, were plotted along the cross section AB. Figure 5.11b shows the volume concentration distribution along the cross section. In

the regions from 0 *mm* to 1.4 *mm* and from 2.6 *mm* to 4 *mm*, the volume concentration is 0, which means these regions were occupied by PE alone, while in the region from 1.7 *mm* to 2.2 *mm*, the volume concentration is 1 meaning this region is PC alone. Due to numerical diffusion, the remaining regions along the cross section (1.4 to 1.7 *mm*, and 2.2 to 2.6 *mm*) were occupied by a mixture of PE and PC. Along with the shear rates and temperatures along the cross-section, we can calculate the viscosities along the same cross-section using the viscosity models for PE and PC.

The simulation results showed that the initial temperature difference disappeared within 8 seconds of shearing (Figure 5.9). From that time onward, a small temperature difference existed between the PC drop and the PE melt. Figure 5.11c shows the temperature curve at different positions along the cross section. The temperature of the PC drop is slightly higher than that of the PE melt due to higher rate of viscous dissipation in the PC drop. However, the temperature difference between the two phases is minimal. The curve of shear rate versus position at time of 21.7s is shown in Figure 5.11d. The highest shear rates are located in the region of the interface. Each bulk phase of PE and PC has its own magnitude of shear rate in the bulk, and the bulk shear rate of PE is much larger than that of PC.

In our simulations, generalized viscosity models were used for both the PE and the PC. The viscosities across AB using these viscosity models are shown in Figure 5.11e. Two distinct viscosities are found for the bulk phase of PE and the bulk phase of PC. The viscosity of the PC phase is much higher than that of the PE phase. Based on the viscosity and shear rate data, we calculated shear stress along the same cross-section A-B.

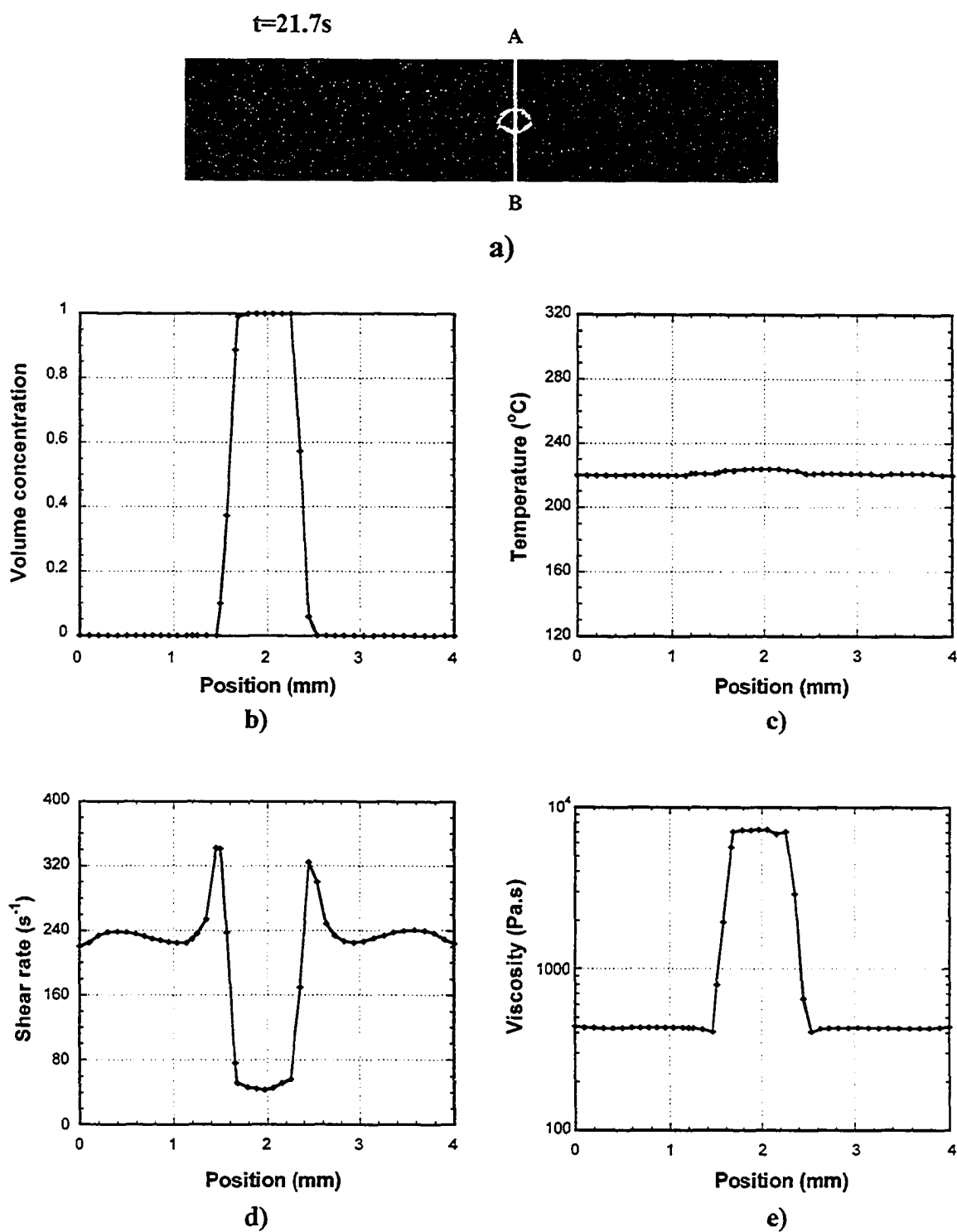


Figure 5.11 a) Cross section AB chosen for plots at time 21.7s; b) Volume concentration vs. position at time 21.7s; c) Temperature vs. position at time 21.7s; d) Shear rate vs. position at time 21.7s; e) Viscosity vs. position at time 21.7s; f) Shear stress vs. position at time 21.7s.

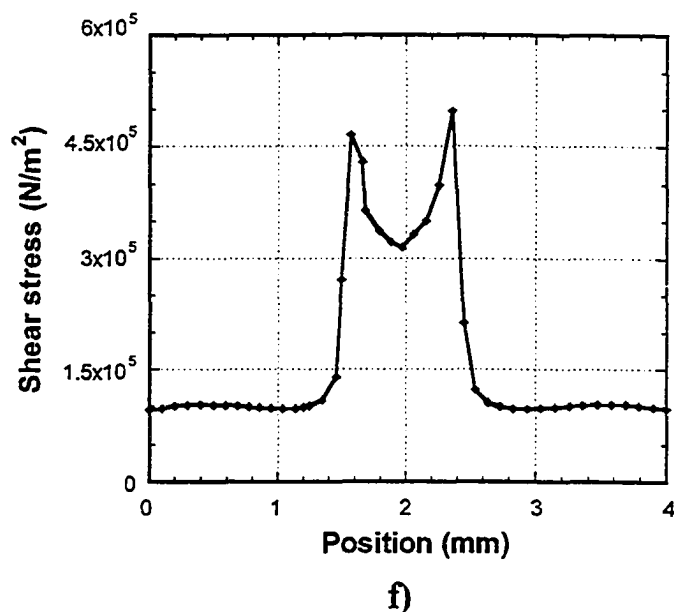


Figure 5.11 (Continued).

The result is shown in Figure 5.11f. Shear stresses in the bulk phase of PC are larger than those of PE. However, two shear stress peaks appear in the two interfacial regions, with values much larger (approximate five times larger) than that in the PE and PC bulk phases. The high shear stress at the interface explains why erosion occurs at the drop surface and the high interfacial stress leads to the deformation and breakup behavior observed in the experiment (14). Using the simulation, we were able to delve into the details of the material and flow properties to better understand why erosion occurs in polymer systems.

5.5 Summary

On-line visualization of PE/PC blend in a TSE showed an “erosion” mechanism for PE pellet in PC melt under complex flow. The deformation and breakup process of PE or PC drop in PE melt under shear flow were modeled using VOF method in FIDAP 8.6. Heat transfer between two phases, viscous dissipation in the melt, free migration of polymer drop, and polymer drop deformation and breakup were captured in the simulations. The simulations showed an erosion mechanism for the polymer drop deformation and breakup under shear flow, and this breakup was qualitatively similar to that seen in its corresponding experimental studies and PE/PC blending in TSE. Heat conduction inside the polymer drop and heat convection outside the drop were clearly seen in the simulation results. It took about 8~10 seconds for the cold polymer drops to reach to their surrounding temperatures under shear flow for the cases studied here. Shear rate and shear stress at the interface were found to be greater than those either in the bulk dispersed phase or in the bulk matrix phase. The results from simulations indicated that the high shear stress at the interface allowed material to be peeled off of the drop surface, and thus explained the erosion mechanism observed in corresponding experiments.

5.6 References

1. Wu, S., "Phase-Structure and Adhesion in Polymer Blends - A Criterion for Rubber Toughening," *Polymer*, **26**, 1855 (1985).
2. Subramanian, P. M., "Permeability Barriers by Controlled Morphology of Polymer Blends," *Polym. Eng. Sci.*, **25**, 483 (1985).
3. Bucknall, C. B., F. P. Cote, I. K. Partridge, "Rubber Toughening of Plastics. 9. Effects of Rubber Particle-Volume Fraction on Deformation and Fracture in HIPE," *J. Mater. Sci.*, **21**, 301 (1986).
4. Montiel, A. G., H. Keskkula, D. R. Paul, "Impact-Modified Nylon-6 Polypropylene Blends. 1. Morphology - Property Relationships," *Polymer*, **36**, 4587 (1995).
5. Taylor, G. I., "The viscosity of a fluid containing small drops of another fluid," *Proc. R. Soc. London, Ser. A*, **138**, 41 (1932).
6. Taylor, G. I., "The formation of emulsions in definable fields of flow," *Proc. R. Soc. London, Ser. A*, **146**, 501 (1934).
7. Grace, H. P., "Dispersion phenomena in high viscosity immiscible fluid systems and applications of static mixers as dispersion devices in such systems," *Chem. Eng. Commun.*, **14**, 225 (1982).
8. Bentley, B. J., and L. G. Leal, "An experimental investigation of drop deformation and breakup in steady, two-dimensional linear flows," *J. Fluid Mech.*, **167**, 241 (1986).
9. Migler, K. B., "Droplet vorticity alignment in model polymer blend," *J. Rheol.*, **44**, 277 (2000).
10. Migler, K. B., "String formation in sheared polymer blends: coalescence, breakup, and finite size effects," *Phys. Rev. Letter*, **86**, 1023 (2001).
11. Sundararaj, U., and C. W. Macosko, "Drop breakup and coalescence in polymer blends: the effects of concentration and compatibilization," *Macromolecules*, **28**, 2647 (1995).
12. Wu, S., "Formation of dispersed phase in incompatible polymer blends: interfacial and rheological effects," *Polym. Eng. Sci.*, **27**, 335 (1987).

13. Levitt, L., and C. W. Macosko, "Influence of normal stress difference on polymer drop deformation," *Polym. Eng. Sci.*, **36**, 1647 (1996).
14. Lin, B., U. Sundararaj, F. Mighri, and M. A. Huneault, "Erosion and breakup of polymer drops under simple shear in high viscosity ratio system," *Polym. Eng. Sci.*, **43**, 891 (2003).
15. Tryggvason, G., B. Bunner, A. Esmaeeli, D. Juric, N. Al-Rawahi, W. Tauber, J. Han, S. Nas, and Y. J. Jan, "A front-tracking method for the computations of multiphase flow," *J. Comput. Phys.*, **169**, 708 (2001).
16. Rallison, J. M., "A numerical study of the deformation and burst of a viscous drop in general linear shear flows," *J. Fluid Mech.*, **109**, 465 (1981).
17. Stone, H. A., "Dynamics of drop deformation and breakup in viscous fluids," *Annu. Rev. Fluid Mech.*, **26**, 65 (1994).
18. Pillapakam, S. B., and P. Singh, "A level-set method for computing solutions to viscoelastic two-phase flow," *J. Comput. Phys.*, **174**, 552 (2001).
19. Li, J., Y. Y. Renardy, and M. Renardy, "Numerical simulation of breakup of a viscous drop in simple shear flow through a volume-of-fluid method," *Phys. Fluids*, **12**, 269 (2000).
20. Chen, H., U. Sundararaj, and K. Nandakumar, "Modeling of polymer melting, drop deformation and breakup under shear flow," *Polym. Eng. Sci.*, **44**, 1258 (2004).
21. Cristini, V., J. Blawdziewicz, and M. Loewenberg, "Drop breakup in three-dimensional viscous flows," *Phys. Fluids*, **10**, 1781 (1998).
22. Sundararaj, U., Y. Dori, and C. W. Macosko, "Sheet formation in immiscible polymer blends: model experiments on initial blend morphology," *Polymer*, **36**, 1957 (1995).
23. Willemse, R. C., E. J. J. Ramaker, J. V. Dam, and A. P. De Boer, "Morphology development in immiscible polymer blends: initial blend morphology and phase dimensions," *Polymer*, **40**, 6651 (1999).
24. Tadmor, Z., "Number of Passage Distribution Functions with Application to Dispersive Mixing," *AIChE J.*, **34**, 1943 (1988).
25. Janssen, J. M. H., and H.E.H. Meijer, "Dynamics of liquid-liquid mixing - A 2-zone model," *Polym. Eng. Sci.*, **35**, 1766 (1995).

26. DeRoussel, P., D. V. Khakhar, and J. M. Ottino, "Mixing of Viscous Immiscible Liquids. Part 1: Computational Models for Strong-Weak and Continuous Flow Systems," *Chem. Eng. Sci.*, **56**, 5511 (2001).
27. Potente, H., M. Bastian, K. Bergemann, M. Senge, G. Scheel, T. Winkelmann, "Morphology of polymer blends in the melting section of co-rotating twin screw extruders," *Polym. Eng. Sci.*, **41**, 222 (2001).
28. Delamare, L., and B. Vergnes, "Computation of the Morphological Changes of a Polymer Blend Along a Twin-Screw Extruder," *Polym. Eng. Sci.*, **36**, 1685 (1996).
29. Huneault, M. A., Z. H. Shi, and L. A. Utracki, "Development of Polymer Blend Morphology during Compounding in a Twin-Screw Extruder. 4. A New Computational Model with Coalescence," *Polym. Eng. Sci.*, **35**, 115 (1995).
30. Shi, Z. H., and L. A. Utracki, "Development of Polymer Blend Morphology during Compounding in a Twin-Screw Extruder. 2. Theoretical Derivations," *Polym. Eng. Sci.*, **32**, 1834 (1992).
31. Li, J., Y. Y. Renardy, and M. Renardy, "Numerical simulation of breakup of a viscous drop in simple shear flow through a volume-of-fluid method," *Phys. Fluids*, **12**, 269 (2000).
32. Van Krevelen, D. W., and P. J. Hoftyzer, "Newtonian shear viscosity of polymeric melts," *Angew. Makromol. Chem.* **52**, 101 (1976).
33. Chen, H., U. Sundararaj, K. Nandakumar, "Experimental and simulation studies of heat transfer in polymer melts," *AIChE J.*, **49**, 1372, (2003).
34. Pham, H. T. and C. J. Carriere, "The effect of temperature on the interfacial tension of polycarbonate/polyethylene blends," *Polym. Eng. Sci.*, **37**, 636 (1997).

Chapter 6

General discussion and future work

6.1 General discussion and conclusions

The study of melting in polymer blending is inspired by widely used industrial processes and covers a wide range of chemical engineering research topics. The heat balance during melting is the focus of this study. It includes melting initiation, melting propagation, heat generation, and heat transfer to polymers under complex flows such as those found in extruders (1~6). The difficulty of theoretical prediction of the heat balance mainly derives from non-Newtonian fluid properties of polymers. Another important topic for the melting study, especially for polymer blends, is the final morphology and final properties achieved under different melting mechanisms. This topic is more practical and related to mixing or morphology development and control during melting. These two topics, though related, are not parallel to each other. Research results from the work related to heat balance during melting provides a basis for the second project (7~10). In this thesis, both topics have been addressed.

Considering the wide application of TSE in industry, our understanding of blending process in twin screw extruder (TSE) is very limited. Thus, melting of polymers in a TSE has been chosen as the focus area for this study. Two commercial polymers, polystyrene (PS, amorphous) and polypropylene (PP, semi-crystalline), were used for the melting study. A sliding barrel technique was used to perform on-line

visualization of polymer blend extrusion, and obtain the axial temperature and pressure along the extruder. Through a glass window fitted in the barrel, the melting behavior of PS/PP blends along the screw channel of the TSE was obtained. Combined with the sliding barrel technique, a pulse method was introduced to detect the location and amount of mechanical energy consumption in the TSE. It was found that the melting of PS/PP blends in the TSE can be divided into three distinct regions: partially filled region, transition region, and fully filled region.

Solid polymer pellets melted in the TSE through an erosion mechanism under the conditions studied in this thesis. In the partially filled region, the peeling off of the outer layer from polymer pellets was caused by the relative movement of pellets against the barrel, while in the transition region, it was caused by contact with neighboring pellets, and in the fully filled region, it occurred through shearing of pellets in the melt flow. The composition of a polymer blend has a significant effect on its melting behavior in TSE. Completely different melting sequences were found for PS/PP (80:20) and PP/PS (80:20) blends even under the same operating conditions. For PS/PP (80:20) blend, the melting was initiated with PS in the partially filled region, and followed by a combined melting of PS and PP in the transition region; while for PP/PS (80:20) blend, the melting was initiated with PP in the transition region, then dominant melting of PS, and finally melting of PP alone in the transition region. As the ratio of Q/N increased, the beginning of the transition region moved upstream.

By comparing the melting initiation difference for PS/PP (80:20) and PP/PS (80:20) blends, we found that heat conduction with the hot barrel was the major heat source for the melting in the partially filled region under the condition studied in this

thesis. Polymers started compaction in the transition region. A highly concentrated polymer melt suspension with solid polymer pellets and compressed air was usually formed at the beginning of the transition region. Most of the melting occurred in the transition region mainly due to mechanical energy consumption. Mechanical energy can be converted to heat through friction energy dissipation (FED), plastic energy dissipation (PED), and viscous energy dissipation (VED) in the TSE. Solid fraction in the transition region was the key factor to determine the relative importance of FED, PED and VED for heat generation. In the transition region, FED and PED played key roles in achieving fast melting of PS/PP blends when the solid fraction was greater than 80%. When there was more polymer melt in the flow, solid friction and solid plastic deformation were greatly reduced due to lubrication between solid particles. VED dominated the melting when the solid fraction was below 60%. When the flow left the transition region, a dilute polymer melt suspension with solid polymer residue was usually formed. Melting in the fully filled region was mainly through VED and heat convection. The end of the melting process can be identified using the visualization results and, to some extent, the pressure profile along the extrusion length.

The major melting occurred in the transition region, where a significant amount of mechanical energy was consumed for the melting. The location of the transition region was determined from the visualization results, temperature and pressure profiles, and the most important from a practical viewpoint, using the pulse method. The pulse method includes three major components: perturbation of a steady state, perturbation signal recording, and flow tracking technique. In this study, the steady state operation was disturbed with an additional mass pulse (30g PS/PP blend), and the motor power

input was monitored as the perturbation signal. For flow tracking, the sliding barrel mechanism and residence time distribution (RTD) probe mounted in the barrel were used. At each slide position, the pulse mass was added to the steady flow together with some RTD tracer. When the pulse mass reached the transition region, additional mechanical energy was needed from the motor to melt the pulse material. As a result of this, a melting peak was generated in the motor power input signal. At the same slide position, the pulse mass flow was tracked by the RTD probe, which measured the concentration of carbon black tracer. When the carbon black reached the RTD probe, its concentration was measured using an optical signal. The RTD signal included a peak which indicated when the maximum concentration of carbon black passed the probe. The location of the RTD probe in the screw channel was known at each slide position. When the melting peak and the RTD peak appeared at the same time, the RTD probe location is where a significant mechanical energy was consumed for the melting. The amount of mechanical energy consumption for melting can also be obtained through integration of the pulse signals. Combining the barrel sliding technique and the pulse method was an effective way to analyze fundamentals of melting in a TSE. However, this technique is not limited to the melting study only in TSE. It provides a new approach to study other process in continuous operation, such as chemical reaction during extrusion (11).

On-line visualization of PS/PP blends extrusion shows that a polymer melt suspension with solid polymer pellets is the typical flow during melting in TSE. Heat transfer coefficient between polymer pellets and polymer melt under complex flow is certainly a necessary parameter to calculate the heat balance during melting. In this

thesis, a batch mixer with two counter rotating blades was modified to capture the shear flow in TSE. The heat transfer coefficient was determined experimentally and numerically for a polymer pellet in another polymer melt under an intensive mixing flow. Based on the experimental set up, two two-dimensional (2-D) and one three-dimensional (3-D) geometries were built for the numerical simulations. The 2-D geometries represent the rectangular and circular cross section of the solid cylindrical pellet. The 3-D simulation captured all geometric characteristics of the experiment, and most closely represents the experiment. In the experiment and simulations, a point temperature inside the pellet was measured or calculated. It was found that only the 3-D simulation matches with the experiment in terms of time for the pellet to reach the reference temperature. The 2-D simulations either over-estimated or under-estimated the time.

The thermocouple dynamics had a significant influence on the temperature history of the pellet. There was some discrepancy between the temperature curves from the experiment and the 3-D simulation, but if we account for the thermocouple dynamics using a first order model and thus adjust the data, the two temperature curves matched very well. From the experimental temperature history, the heat transfer coefficient was determined to be $370 \text{ W} / \text{m}^2 \cdot \text{K}$. However, this value was obtained based on the assumption of an even convective environment, which is not true for the experiment, and does not account for effect of thermocouple dynamics. From the 3-D simulation, the heat transfer coefficient varied with time and the average was calculated to be $250 \text{ W} / \text{m}^2 \cdot \text{K}$. Simulation results allowed us to understand the experiment better,

and we were able to obtain a more representative heat transfer coefficient, since the simulation could account for the uneven convective environment in the mixer.

Heat transfer from the surrounding fluid provides a basic and direct way for the melting of dispersed phase. However, for polymer systems, viscous energy dissipation plays a critical role in converting mechanical energy into heat and leads to quick melting (2~5). The typical flow during melting in TSE is a suspension of solid polymer pellets in a polymer melt. The existence of solid polymer pellets in the already highly viscous polymer melt would enhance the viscous dissipation and accelerate the melting process, especially in the transition region in TSE where the solid concentration is relatively high (>50%). In this thesis, a model system, ethylene acrylate copolymer (EAC) melt suspensions with PS beads, was used to investigate rheological properties of polymer mixtures during melting in polymer processing equipment, such as TSE. Three temperatures near to PS T_g ($\sim 100^\circ\text{C}$) and above EAC T_m ($\sim 60^\circ\text{C}$) were chosen for the measurement to capture the characteristics of the softening process during melting. It was found that the viscosity of concentrated polymer melt suspensions can be over 20 times higher than that of the polymer melt, which gave us a sense how much more heat can be generated for the melting due to viscous dissipation. For the system studied here, the power law model is capable of describing the relationship between viscosity and frequency in the range of 10s^{-1} and 100s^{-1} . The shear thinning behavior of these suspensions was enhanced at higher concentrations of PS beads. In the frequency range studied here, the frequency had significant effect on the relative viscosity only for highly concentrated suspensions.

The relative viscosity of the suspensions did not monotonically increase with volume fraction ϕ as seen previously in the literature (12, 13). A new phenomena occurred in the EAC melt suspensions with PS beads at a critical ϕ , ϕ_d , after which the relative viscosity decreased with ϕ . This decrease was followed by an increase in relative viscosity when ϕ was close to the typically observed critical maximum volume fraction ϕ_m . Deformation of PS beads along the flow direction in concentrated suspensions is postulated to be the reason for the decrease of relative viscosity with ϕ between ϕ_d and ϕ_m . Deformation of dispersed phase under local shear stress also could explain the difference of the relative viscosity found in our measurement (~20) and estimated by Todd (~80, ref. 1). Compared to homogeneous samples, the sandwich samples generated a significant wall effect. The relative viscosity of the sandwich structure suspensions was always lower than that of the homogeneous suspensions when ϕ was below ϕ_m . New equations are needed to predict the relative viscosity of suspensions by taking into account the effect of deformation of the dispersed phase.

On-line visualization shows gives an overview of the melting behavior of polymers in TSE. Heat transfer and rheological study of polymer melt suspensions provide some necessary data to calculate the heat balance and detailed local information about the polymer flow during melting. Another important topic is morphology development during melting and this is also addressed in this thesis. On-line visualization of PS/PP blends in the TSE shows an “erosion” mechanism for solid polymer pellets in all three regions: friction with the barrel in the partially filled region, friction between solid polymer pellets in the transition region, and friction between solid polymer pellet and the fluid under shear in the fully filled region. Through this

erosion mechanism, solid PS or PP polymer pellets melted and dispersed in the continuous fluid.

The “erosion” mechanism was also found in a Couette flow for polycarbonate (PC) droplet in polyethylene (PE) melt (14). On-line visualization was performed again in this thesis to study the PC drop deformation and breakup in PE melt under complex flow generated in TSE. Since T_m of PE (140°C) is much lower than the flowing temperature of PC (250°C), and considering the low concentration of PC (10%) in the flow, a PE melt suspension with solid PC pellets was formed in the fully filled region. The same “erosion” mechanism was found for PC pellets in PE melt under complex flow in the TSE. Numerical simulations were carried out to study the details about the erosion mechanism using volume-of-fluid method. 2-D geometry model was built based on the corresponding experimental setup (14). Heat transfer between two phases, viscous dissipation in the melt, free migration of polymer drop, and polymer drop deformation and breakup were captured in the simulations. The simulations showed an erosion mechanism for the polymer drop deformation and breakup under shear flow, and this breakup was qualitatively similar to that seen in its corresponding experimental studies and PE/PC blending in TSE. Heat conduction inside the polymer drop and heat convection outside the drop were clearly seen in the simulation results. It took about 8~10 seconds for the cold polymer drops to reach the temperature of the surroundings under shear flow for the cases studied here. Shear rate and shear stress at the interface were found to be greater than those either in the bulk dispersed phase or in the bulk matrix phase. The high shear stress at the interface allowed material to be peeled off of

the drop surface, and thus explained the erosion mechanism observed in previous experiments.

In summary, this thesis identified melting of polymers in a TSE occurred in three distinct regions. Most melting occurred in the transition region. Heat transfer and rheological properties related to the typical flow in the transition region was studied in detail. An “erosion” mechanism was found for polymer blends during melting, and an explanation for this mechanism was determined through numerical simulations.

6.2 Future work

6.2.1 Melting or reaction of polymer blends during extrusion

This study focused on the melting process during polymer blending. A standard melting screw configuration and polymers in pellet form were used for all extrusion experiments in this thesis. However, there are many different screw configurations widely used in industry for different purposes, and the polymers are not necessary only used in the pellet form (15). Therefore, there is a need to study the melting behavior of polymer blends under different screw configurations and different types of feed (powder, flake, etc.).

More work is needed to study the effect of polymer particle shape and size on the melting. Our preliminary experiments with PS and PP powder, using the same pulse method, show that the size of polymer particles had a significant effect on the melting behavior of polymers in extrusion. The energy input signal experienced a decrease and then an increase after the powder form of polymers was introduced to disturb the steady state operation. Further experiments and analysis are needed to explain the new result and characterize the melting behavior of polymer powder in extrusion as well as other shapes like flakes.

The combination of sliding barrel mechanism and the pulse method provides a useful tool to probe the melting process in extruders. This technique can also be used for studies of other processes, such as reactive extrusion (16). Chemical reactions that occur during extrusion change molecular structure of some polymers, and most likely result in viscosity change of polymer flow. Using the sliding barrel mechanism and the pulse method, we can detect where the reaction occurs in the channel and how long it

takes for the reaction to finish in the extruder. This information is essential for us to understand and control the dynamics of chemical reactions in extruders.

6.2.2 Heat transfer of a free polymer pellet in polymer melt

Solid polymer pellets follow the flow during melting in blending equipment. Heat transfer coefficient between a free moving solid polymer pellet and polymer melt is a necessary parameter to calculate the heat balance during melting. In general, the heat transfer coefficient with a free moving pellet should be lower than the value with a fixed pellet under the same flow conditions. Numerical simulation provides an effective way to obtain both values and evaluate their difference. However, one of the difficulties of obtaining the heat transfer coefficient with a free moving pellet is experimental validation, i.e. monitoring the temperature history of a free moving pellet in a flow. A few options, such as fluorescence (17, 18), infrared thermography (19), or optical temperature measurement (20) could be used to develop a method to monitor the temperature history of a moving pellet on-line.

The effect of viscoelastic properties of polymers on the heat transfer coefficient is another project that should be addressed for the study of melting. Experiments with pure viscous fluid and viscoelastic fluid should be conducted to test the effect. Then numerical simulations can be used to obtain the heat transfer coefficient. Suitable viscoelastic models should be built and incorporated into simulations to accurately predict the important heat transfer process that occurs during melting.

6.2.3 Rheology of polymer blends in transition from suspension to emulsion

During melting of the polymer blending process, a polymer suspension was usually formed in the early stages and then changed to a polymer emulsion in later stages. Understanding of the rheological property change from suspension to emulsion for the same polymer blend is certainly an interesting topic for the melting study. The experimental measurement should cover systems with semi-crystalline polymer and/or amorphous polymer. The two component polymers for one system should be carefully chosen so that the matrix phase has a lower melting or softening temperature than the dispersed phase, and the matrix phase should not degrade too much at the melting or softening temperature of the dispersed phase. Ethylene-acrylate copolymer (EAC, $T_m=64^{\circ}\text{C}$) and polystyrene (PS, $T_g=100^{\circ}\text{C}$) beads could be one combination to study the rheological property change for semi-crystalline polymer/amorphous polymer system. However, the stability of EAC at PS flowing temperature ($\sim 160^{\circ}\text{C}$) should be checked before running the experimental tests.

Besides experimental measurements, numerical simulation with fluid-structure-interaction (FSI) strategy provides another useful tool to study the rheological properties of polymer melt suspensions. Compared to experimental measurement, the FSI simulation will show not only the rheological properties of the polymer melt suspension, but also lots of local information about the flow and the solid, such as, local shear rate, structure orientation during shearing, and possible deformation of particles under shearing. Corresponding experiments would also be necessary to check the simulation results.

6.2.4 Heat balance of polymer flow during melting

Heat balance calculation of polymer flow during melting requires a clear identification of each possible heat source and its magnitude. Taking polymer melting in a TSE as an example, the heat balance of this melting process could be studied in the three distinct regions: partially filled region, transition region, and fully filled region. Heat balance in each region can be built based on well identified heat sources in each region. In the partially filled region, heat conduction from the hot barrel and air convection in the channel may be the major heat sources to heat up the solid polymer; in the transition region, solid polymer friction, plastic energy dissipation and viscous dissipation may contribute most of the heat for the melting in this region; and in the fully filled region, heat convection and viscous dissipation may dominate the last stage of melting in the channel.

Theoretical prediction of and basic theory for every heat source for melting remains a big challenge in the polymer processing field. Data from numerical simulations, such as heat transfer coefficient, and data from experimental measurements, such as mechanical energy consumption, can be combined to obtain the contribution of each heat source in the heat balance calculation. The pulse detection provides an experimental method to obtain mechanical energy consumption for melting. The mechanical energy consumption includes friction energy dissipation (FED), plastic energy dissipation (PED), and viscous energy dissipation (VED). From the rheological data of polymer melt suspensions, the VED could be separated from the mechanical energy consumption. However, the separation of FED and PED remains a big challenge in this field mainly due to viscoelastic properties of polymer materials. Applicable

theoretical descriptions of FED and PED are needed for polymers to calculate the heat balance of polymer melting during processing. Modeling of lubricated polymer-polymer friction is certainly another important subject for the heat balance calculation (21). From the heat balance study, the relative importance of each heat source can be found in each region and also for the whole melting process.

6.2.5 Modeling of drop deformation and breakup with viscoelastic properties

Viscoelastic properties were believed to be the major reason for the difference of critical shear rate for breakup between experiments and simulations (see Chapter 5). It is necessary to incorporate viscoelastic properties of polymer melts into simulation models and extend two-dimensional models to three dimensional models to study the details of polymer drop deformation and breakup. Besides the “erosion” mechanism, several other mechanisms, such as parallel elongation, vorticity breakup, and so on, have been found from on-line visualization (22) of polymer drop breakup. However, the theoretical explanation of those mechanisms is still under investigation. Numerical simulations of drop breakup with viscoelastic properties may help to solve this problem considering the ever increasing power of computers.

Volume-Of-Fluid (VOF) method provides an easy and effective method to study the mechanism of polymer drop deformation and breakup. The interface is smoothed and tracked through a marker concentration function in VOF method (see chapter 5). With this approximation to real system, VOF method should not be used to obtain particle size and distribution during breakup. Incorporation of advanced front tracking

method into numerical models (23) certainly will boost the study of morphology development and control during polymer melting.

6.3 References

1. Todd, D. B., "Melting of Plastics in Kneading Blocks," *Intern. Polym. Process.*, **8**, 113 (1993).
2. Gogos, C. C., Z. Tadmor, M. H. Kim, "Melting Phenomena and Mechanisms in Polymer Processing Equipment," *Adv. Polym. Tech.*, **17**, 285 (1998).
3. Vergnes, B., G. Souveton, M. L. Delacour, A. Ainsler, "Experimental and Theoretical Study of Polymer Melting in a Co-Rotating Twin Screw Extruder," *Inter. Polym. Process.*, **16**, 351 (2001).
4. Jung, H., J. L. White, "Investigation of Melting Phenomena in Modular Co-Rotating Twin Screw Extrusion," *Intern. Polym. Process.*, **18**, 127 (2003).
5. Potente, H., M. Bastian, "Polymer Blends in Co-Rotating Twin-Screw Extruders," *Intern. Polym. Process.*, **16**, 14 (2001).
6. Tenge, S., D. Mewes, "Experimental Investigation of the Energy Balance for the Metering Zone of a Twin-Screw Extruder," *Polym. Eng. Sci.*, **40**, 277 (2000).
7. Scott, C. E., C. W. Macosko, "Model Experiments Concerning Morphology Development during the Initial-Stages of Polymer Blending," *Polym. Bull.*, **26**, 341 (1991).
8. Sundararaj, U., C. W. Macosko, R. J. Rolando, H. T. Chan, "Morphology Development in Polymer Blends," *Polym. Eng. Sci.*, **32**, 1814 (1992).
9. Li, H. X., G. H. Hu, and J. A. Sousa, "The Early Stage of the Morphology Development of Immiscible Polymer Blends During Melt Blending: Compatibilized vs. Uncompatibilized Blends," *J. Polym. Sci. Pol. Phys.*, **37**, 3368 (1999).
10. Potente, H., S. Krawinkel, M. Bastian, M. Stephan, P. Potschke, "Investigation of the Melting Behavior and Morphology Development of Polymer Blends in the Melting Zone of Twin-Screw Extruders," *J. Appl. Polym. Sci.*, **82**, 1986 (2001).
11. Wetzel, M. D., D. A. Denelsbeck, S. L. Latimer, "A Perturbation Method to Characterize Reactive Extrusion," *SPE ANTEC Tech. Papers*, (2003).
12. Mooney, M., "The viscosity of a concentrated suspension of spherical particles." *J. Colloid Sci.*, **6**, 162 (1951).

13. Krieger, I. M., "Rheology of monodisperse latices," *Advan. Colloid Interface Sci.*, **3**, 111 (1972).
14. Lin, B., U. Sundararaj, F. Mighri, M. A. Huneault, "Erosion and Breakup of Polymer Drops under Simple Shear in High Viscosity Ratio Systems," *Polym. Eng. Sci.*, **43**, 891 (2003).
15. Andersen, P. G., "mixing practices in corotating twin-screw extruders," in *mixing and compounding of polymers*, edited by Ica Manas-Zloczower and Zehev Tadmor, Hanser Publishers, New York, chapter 20 (1994).
16. Moad, G., "The synthesis of polyolefin graft copolymers by reactive extrusion," *Progress in Polym. Sci.*, **24**, 81 (1999).
17. Migler, K. B., A. Bur, "Fluorescence based measurement of temperature profiles during polymer processing," *Polym. Eng. Sci.*, **48**, 213 (1998).
18. Bur, A. J., M. G. Vangel, S. C. Roth, "Fluorescence based temperature measurements and applications to real-time polymer processing," *Polym. Eng. Sci.*, **41**, 1380 (2001).
19. Johnson, E. J., P. V. Hyer, P. W. Culotta, I. O. Clark, "Evaluation of infrared thermography as a diagnostic tool in CVD applications," *J. Cryst. Growth*, **187**, 463 (1998).
20. Alkemper, J., S. Sous, C. Stocker, L. Ratke, "Directional solidification in an aerogel furnace with high resolution optical temperature measurements," *J. Cryst. Growth*, **191**, 252 (1998).
21. Hsu, G., A. E. Yagle, K. C. Ludema, J. A. Levitt, "Modeling and identification of lubricated polymer friction dynamics," *Transactions of the ASME*, **122**, 78 (2000).
22. Bin, L. "Visualization of polymer drop breakup," University of Alberta, *PhD thesis* (2005).
23. Tryggvason, G., B. Bunner, A. Esmaeeli, D. Juric, N. Al-Rawahi, W. Tauber, J. Han, S. Nas, and Y. J. Jan, "A front-tracking method for the computations of multiphase flow," *J. Comput. Phys.*, **169**, 708 (2001).